ABSTRACT

Title of Dissertation:	EVALUATION OF AN ADDITIVELY MANUFACTURED FERRITIC-MARTENSITIC STEEL FOR ADVANCED NUCLEAR APPLICATIONS
	Daniel A. Vega, Doctor of Philosophy, 2018
Dissertation directed by:	Professor Mohamad Al-Sheikhly, Department of Material Science and Engineering

A multidisciplinary investigation is presented in which the first known Additively Manufactured (AM) ferritic/martensitic (FM) steel alloys were evaluated for suitability as fast reactor structural components. As AM becomes more mainstream, it offers new possibilities in improving the design and cost of metal parts, especially those with weldability and workability limitations. However, questions remain about AM's ability to reliably produce the types of high performance ferritic alloys that require carefully tailored microstructures. Laser-based AM produces heating patterns that interfere with the phase transformations from which wrought FM steels derive their ductility, high strength, and creep resistance. Additionally, study of irradiation effects on AM materials is immature. To address these questions, this dissertation presents an analysis of AM Grade 91 steel, an alloy with established pedigree in the nuclear and fossil fuel sectors, and whose ASME code case establishment was the first in a family

of creep strength enhanced FM steels. Material from the first known successful AM build of Grade 91 steel was prepared, heat treated, analyzed using microstructural characterization techniques, subjected to a range of mechanical testing (to 600 °C), and irradiated up to 100 dpa with 5 MeV Fe^{2+} ions.

Among the most salient findings were that i) AM material that was subjected to a prescribed normalization heat treatment developed a uniform microstructure and martensite fraction similar to wrought material, ii) normalized and tempered AM material had a similar distribution of carbide precipitates, but finer grain structure than wrought material, iii) AM material was slightly harder and less ductile than wrought material at room temperature, but at 300 °C and 600 °C, their mechanical strength/ductility were virtually the same, iv) AM heat treated material directly built and tested without heat treatments had an unpredictable and heterogeneous microstructure, but that when tensile tested, demonstrated extremely high strength and unexpectedly high ductility, especially at high temperatures, and iv) AM material showed less radiation-induced hardening, due to its fine grain structure. Indications are that AM Grade 91 steel may well be suitable for advanced nuclear applications, and additional research leading to a path forward for certification should be pursued.

EVALUATION OF AN ADDITIVELY MANUFACTURED FERRITIC-MARTENSITIC STEEL FOR ADVANCED NUCLEAR APPLICATIONS

by

Daniel Armando Vega

Dissertation submitted to the Faculty of the Graduate School at the
University of Maryland, College Park, in partial fulfillment
of the requirements for the degree of
Doctor of Philosophy
2018

Advisory Committee:
Professor Mohamad Al-Sheikhly[1], Chair
Professor Mohammad Modarres[1]
Professor Gary Pertmer[1]
Professor Lourdes Salamanca-Riba[1]
Doctor Stuart Maloy[2]

[1]University of Maryland
[2]Los Alamos National Laboratory

Dedication

To my late mother, Kathy Vega. Look Mom, no hands.

Acknowledgements

Thank you to the MSE Department at the University of Maryland; I could not have accomplished this work without the encouragement and patience of my advisor, Dr. Mohamad Al-Sheikhly, who stuck with me through years of difficulties and interruptions. Thank you as well to Dr. Travis Dietz, and Dr. Peter Zavalij, both of whom are great assets to the Department.

Secondly, thank you to the incredible staff at Los Alamos National Laboratory – especially to Drs. Stu Maloy, Carl Cady, Eda Aydogan, Jordan Weaver, Ben Eftink, DV Rao, and Tom Lienert, for demonstrating why LANL has such a high and well-deserved reputation.

Also, thank you to the U.S. Department of Energy, for supporting me (and funding me) to chase this professional and personal goal. Specifically, I would like to acknowledge Dr. John Herczeg, Dr. Patricia Paviet, Bill McCaughey Ray Furstenau for investing in me, and Dr. Mary Gillespie for believing in me and pushing me forward, especially at the low points. And, a very special thanks to DOE's finest loop crew: Farah Benahmed, Mike Reim, and Alisa Trunzo - may our days never be dull.

Finally, thank you to Siobhan Perkins. For everything.

Table of Contents

List of Tables

List of Figures

List of Abbreviations

AM	Additive Manufacturing
ASME	American Society of Mechanical Engineers
BCC	Body Center Cubic
BCT	Body Centered Tetragonal
CCT	Continuous Cooling Transformation
CSEF	Creep Strength Enhanced Ferritic
DPA	Displacements Per Atom
DMLS	Direct Metal Laser Sintering
EBSD	Electron Backscatter Diffraction
EDM	Electrical Discharge Machining
FCC	Face Centered Cubic
FFTF	Fast Flux Test Facility
FGHAZ	Fine Grain Heat Affected Zone
FM	Ferritic-Martensitic
FP	Frenkel Pair
HAZ	Heat Affected Zone
IBML	Ion Beam Materials Laboratory
LET	Linear Energy Transfer
LMD	Laser Metal Deposition
LMFBR	Liquid Metal Fast Breeder Reactor
LANL	Los Alamos National Laboratory
LWR	Light Water Reactor

ODS	Oxide Dispersion Strengthened
PKA	Primary Knock-On Atom
SFR	Sodium-cooled Fast Reactor
TE	Total Elongation
TEM	Transmission Electron Microscopy
UE	Uniform Elongation
UTS	Ultimate Tensile Strength
YS	Yield Strength
XRD	X-Ray Diffraction

1. Introduction and Background

Looking to the future, a stark difference in the traditional approach to nuclear innovation has been taking hold in the United States. Rather than relying on a limited number of large reactor vendors producing large Light Water Reactors (LWRs) to move the industry forward, a nascent industry of nuclear startups have begun to lead the way in innovation of new reactor types. At the time of this writing, several billion dollars in private capital have been invested in over 40 of these nuclear startup companies in North America [1].

Reactors under development by most of these nuclear startups are generally smaller, lower power designs, many of which can be modularized. Reactors of varying technical readiness levels, fuel types, coolant types, and neutron spectra are being evaluated in modern, innovative ways. Fresh thinking on the size and functionality of advanced reactors has brought forth the opportunity to couple young, innovative companies with world-class government research institutions thorough mechanisms like the U.S. Department of Energy's Gateway for Accelerated Innovation in Nuclear (GAIN) [2].

Contemporaneous to advanced reactor designs and ongoing materials research, the manufacturing industry is experiencing a revolution in the field of additive manufacturing (AM) technologies, sometimes known collectively as 3-D printing. With the emergence and growing ubiquity of off-the-shelf AM technology, entities from backyard hobbyists to government/military field operations are designing and producing rapidly prototyped parts of all shapes and materials for both research and practical use. AM uses automated technology to build components from bulk material, layer by layer. In doing so, it can

produce shapes and geometries that are too difficult or costly to achieve through traditional fabrication and machining. Furthermore, because some metals have limited workability and weldability once they are manufactured, AM could fabricate complex components directly.

In this spirit, this dissertation aims to evaluate for the first time, a ferritic/martensitic (FM) steel fabricated with laser-based AM for use as a structural material in advanced fast spectrum reactors. While Selective Laser Sintering (SLS) is now a commonplace method for fabricating metallic parts from constituent powder, alloys whose microstructural properties depend on their fabrication methods may or may not be suitable for such laser fabrication methods. Traditional fabrication methods for steels such as casting, forging, and other techniques can produce a part with a uniform microstructure. AM metal fabrication, on the other hand, produces parts through localized sintering or melting of powder, layer by layer. The effects of this type of fabrication on microstructure are a subject of study in modern AM development.

Both stainless steels (e.g., Austenitic 316-L) and Ferritic/Martensitic (FM) have a proven track record of success in energy/industrial sectors [3]. However, stainless steel has limitations in highly damaging radiation environments, such as those found in fast reactors, due to excessive swelling and void formation [4]. Ferritic/martensitic (FM) alloys (which have their origins in fast reactor development) have superior radiation resistance, and their high strength and creep resistance have made them staples of the power industry. One particular grade of FM alloy, Grade 91, was the first in a family of creep strength enhanced ferritic (CSEF) steels for which a code case was developed for use in high-temperature

industrial applications by the American Society of Mechanical Engineers (ASME), and is the subject of this investigation [5,6].

While effective in its current usage, Grade 91 steel has limitations when it comes to weldability and workability. Traditionally wrought Grade 91 products are strong and hard, making them less workable than traditional stainless steels, and welding tends to decrease their service lifetime [6]. Direct prototyping of metal parts using AM could enable the fabrication of complex geometries without the need for difficult and labor-intensive welding techniques, and introduction of potential creep stresses in heat affected zones (HAZs). The ability to create custom shapes – fuel components, ducting, grid spacers, ducts, even entire cores – from Grade 91 steel with longer lifetimes than wrought (traditional) material would prove an extremely valuable capability not just for nuclear applications, but any industry using FM steels.

FM steels rely on a number of mechanisms for their enhanced strength. Diffusionless phase transformations (to martensite) are the main mechanism for strengthening in basic Cr-Mo alloys, though modified Cr-Mo (Grade 91) also achieves precipitation hardening through the formation of carbides and nitrides (and carbonitrites) with the microalloying elements (V, Nb) [7]. While it is known that properties such as creep strength are strongly influenced by heat and strain cycles during fabrication [8], it is not known not clear the extent to which such critical transformations are affected by the irregular heating patterns of laser sintering. Observing and determining these effects are a central theme in this study.

This dissertation is thus presented as a multidisciplinary approach in which the first known successful build of AM Grade 91 steel is characterized from a microstructural

perspective (both pre and post heat treatment), tested for mechanical properties, and subjected to highly damaging irradiation with the goal of determining its suitability for advanced fast reactor components. If successful, this investigation will pave the way for improved understanding of the microstructural effects of non-uniform heating cycles during AM fabrication of FM steels, as well as supporting a path forward for licensing and mainstreaming additively manufactured FM steels in the energy, water and defense industries.

1.1. Motivation and Objectives

The nuclear industry in the United States is at a critical juncture in its history. Many traditional Light-Water Reactor (LWR) nuclear plants are nearing the end of their operating lifetimes, and some are closing prematurely due to market forces and regional/national politics. License extensions, high capacity factors, and power upgrades have helped the nuclear sector to increase its capacity, but at current rates, the net generation capacity of nuclear-produced electricity is trending downward without the addition of new plants. Periods of optimism that reactor vendors and government initiatives might revitalize the industry have generated interest in building new plants, but downward price movement of fossil fuels and high upfront capital requirements for new plants have, in recent years, stalled plans to significantly expand the nuclear sector in the United States. And yet, nuclear power still produces the majority of the U.S.'s low-carbon electricity, and it is widely recognized that nuclear

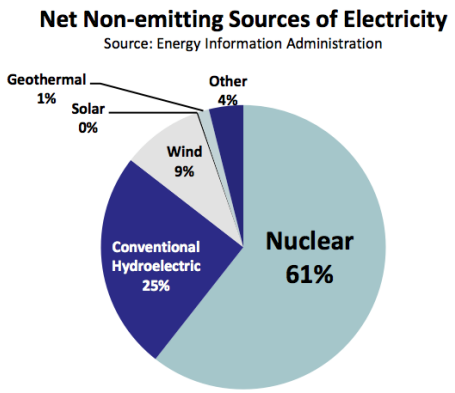

Figure 1.1. Primary sources of non-carbon based electricity[9].

power must play a crucial role in a low-carbon energy sector of the future.

Though preserving and improving the commercial nuclear fleet is fundamental to the United States' domestic energy security and environmental sustainability, the future of nuclear power will ultimately depend on the next generation of advanced reactors coming to market. Renewed interest by the private sector and a focus towards smaller, modularized designs is taking shape. These new designs fall into several basic categories, including technically mature Small Modular Reactors (SMRs) using familiar water-cooled systems, High-Temperature Gas Reactors (HTGRs), liquid metal cooled fast reactors (such as sodium fast reactors), and molten salt reactors (MSRs). Additionally, small, deployable special purpose reactors (also known as micro-reactors) are also being investigated for potential defense operations [10].

Though each advanced reactor type has its advantages and disadvantages, fast reactors have the potential for unparalleled resource utilization, due to their ability to produce fissile material at a higher rate than it is consumed (called breeding), as well as their ability to utilize spent fuel from other reactors as a fuel supply. Additionally, fast reactors are capable of transmuting undesirable minor actinides, removing them from the waste disposal chain. The compact, high power density nature (to prevent neutron moderation) of fast reactor cores, coupled with the high damage rate of fast neutrons, provides for a unique challenge in materials development. Though this investigation is focused on the development of AM steel for the specific needs of fast reactor development, but its implications may be significant to any industry for which AM metal fabrication is being considered.

To be competitive, advanced reactor systems will need to operate with predicable costs and high efficiency. Like any heat cycle, nuclear plant efficiency in nuclear systems is heavily dependent on the magnitude of the thermal gradient between the operating temperature and thermal reservoir. Higher temperatures enable higher thermodynamic efficiencies, and fast reactor systems are designed with this principle in mind.

The goal for fast reactor development should be to operate at the highest practical temperatures allowed by materials considerations, minus a built in safety factor. Doing so requires that reactor core structural materials be capable of safely operating at high temperatures (~650 °C), but also that they resist chemical corrosion, withstand the effects of high-fluence irradiation, and that they resist long-term deformation phenomena (creep) sufficiently to maintain the critical geometries for safety and neutron transport considerations.

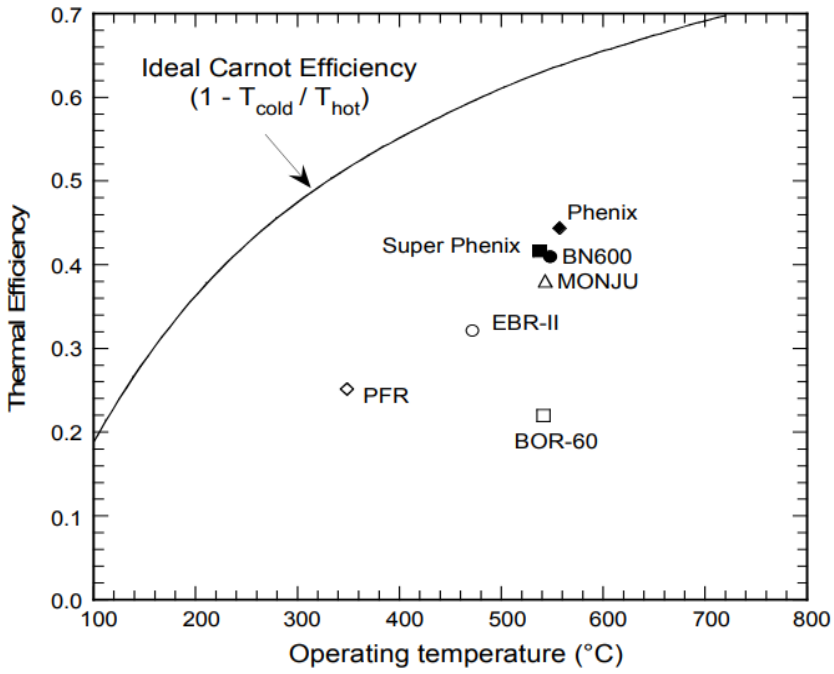

Figure 2.2. Thermal efficiency vs operating temperature for selected fast reactors[11].

The choice of Grade 91 steel being the subject of this investigation was made because it has an attractive and unique combination of properties and pedigree. Martensite formation, the crucial phase transformation and micro-constituent largely responsible for the high strength of Grade 91 steel, is observed and characterized, but not completely understood from an ab-initio perspective. Regardless, the fabrication repeatability and excellent performance of wrought Grade 91 has led to its being granted an ASME Code Case for Boiler and Pressure Vessel use in power plants, and along with it a compendium of data on (unirradiated) thermomechanical performance [12]. This code case prescribes the fabrication and heat treatments of Grade 91 steel, but has no guidance on alternative fabrication technologies (like AM). To date, outside this experiment there has been no known fabrication of Grade 91 steel from constituent powder and Direct Metal Laser Sintering (DMLS), and thus this investigation represents a pioneering leap into the world of advanced fabrication and characterization of alloyed steels.

It is not known exactly how laser-induced heating and cooling might affect martensite formation, other microstructural properties, or thermomechanical performance; nor is it known whether AM fabricated steel can be made congruent to wrought material through heat treatments. Thus, whether AM truly creates "Grade 91" steel, or a merely a compositional equivalent replica, remains an existential (and regulatory) question.

To address these questions, this dissertation aims to evaluate the suitability of AM FM steels by accomplishing the following objectives:

Objective 1: Characterize the first known build of AM Grade 91 material, both in in its As-deposited form directly (no heat treatments), as well as after prescribed normalization

and tempering heat treatments. This includes microstructural analysis and characterization using microscopy and X-ray diffraction, as well as qualitative analysis of builds quality (density, surface finish)

Objective 2: Perform a series of mechanical tests to determine the tensile strengths and stress/strain behavior of AM Grade 91 material of each type and heat treatment. This includes determining the materials' yield strength, tensile strength, creep strain rate, and ductility, and comparing it to that of wrought Grade 91 steel.

Objective 3: Perform irradiations of AM (and wrought) Grade 91 material to assess the effects of highly damaging ion beam radiation (Fe^{2+} ions, up to 100 dpa) at elevated temperatures by performing nano-indentation and nanohardness tests post-irradiation.

In accomplishing these objectives, this dissertation will have laid the ground work for understanding, quantifying, and manipulating the unique microstructure that is accompanies with laser-based AM of ferritic/martensitic steels, and alloys in general.

1.2. Selection of Fast Reactor Materials

Alloyed steels are designed and chosen primarily for their ability to maintain stability under thermomechanical and chemical conditions. Steels used in reactor applications have the additional complication of being exposed to damaging radiation fields, which can exacerbate degradation mechanisms. The extent to which steels are degraded over time by radiation depends on a complex interplay of damage and repair mechanisms related to the dose rate (or damage rate), environmental conditions (temperature, stress, chemical atmosphere), and microstructural features of the materials.

As the name suggests, fast reactors differ from thermal reactors is that the fast spectrum neutrons are the primary contributor to the fission rate. Neutrons are born from fission with a fission spectrum average energy of around 2.2 MeV, and are deliberately kept from slowing down via moderation. Fast neutrons are capable of inducing fission not only in fissile material (as is done in thermal reactors), but also in "fissionable" isotopes, whose threshold for neutron-induced fission is within the energy range of fast neutrons, but higher than that of thermal neutrons (0.025 eV) of fissile material. Additionally, fast neutrons are absorbed by fertile isotopes, which then decay into fissile isotopes, providing additional fuel for the reactor.

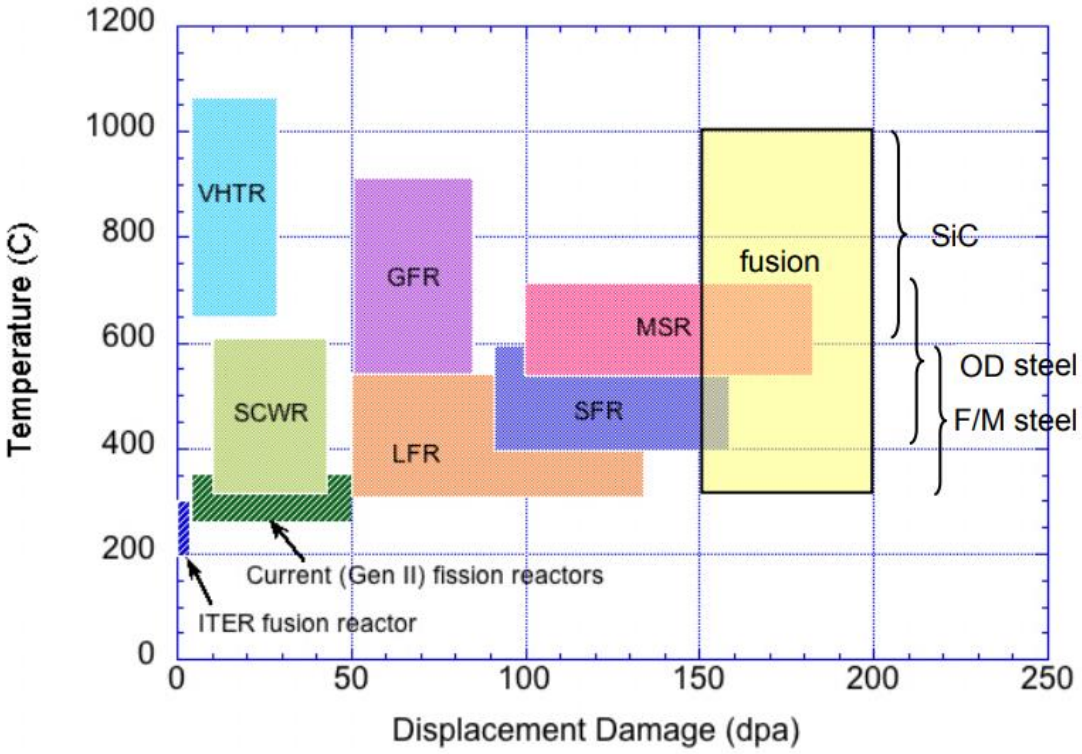

Figure 1.3. Performance space for fast reactor core materials[13]

Because of the harder spectrum of fast reactors, the resulting radiation damage is higher as well. As will be discussed later in the chapter, induced radiation damage is

proportional to the energy of the incoming particle, and thus, a single fast neutron will produce orders of magnitude more damage than thermal neutron (from an elastic kinetics perspective). Combined with the demand for high temperature performance and chemical stability, this makes the development and selection of materials for fast reactors particularly challenging.

In developing and selection reactor steels, there will usually be trade-offs from a material selection standpoint. Simple crystal structures may show better radiation resistance but sensitivity to corrosion, while highly complex and specialized solution-strengthened alloys may have far better environmental resistance and strength, but be susceptible to irradiation embrittlement, creep, or void formation. Like most engineering decisions, these and other tradeoffs (such as cost, ease of fabrication and welding) must be considered when choosing a material.

Austenitic stainless steels have long been the choice for elevated temperature applications in the nuclear industry, owing to their high thermal conductivity and corrosion resistance. Though there are several major differences in austenitic stainless steels and FM steels, a large discriminator between the two in selection of materials for fast reactor systems stems from their differences in radiation-induced void swelling.

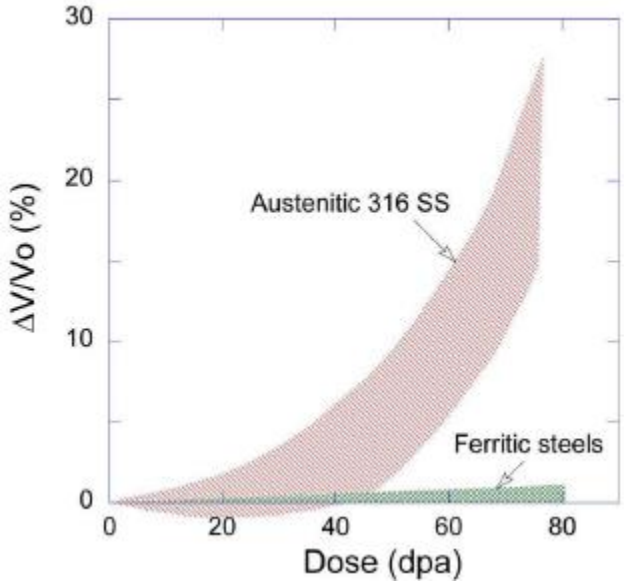

Figure 1.4. Swelling of stainless steel and ferritic steels[4]

Austenized 316 stainless steel has been the workhorse of the nuclear industry. It has a proven track record of predictable performance and resistance to corrosion, and excellent workability/weldability. However, 316 L loses much of its performance at temperatures above 600 °C and creep becomes a limiting factor at those temperatures as well [14]. Even non-pressurized systems like heat pipe and micro-reactors, temperatures are expected to reach up to around 635 °C [15].

1.3. Background on Radiation Effects in Solids

Principally, radiation damage in reactor materials is produced by energetic subatomic particles (neutrons, ions, protons, electrons, etc.) interacting with a crystalline solid. An incident particle with sufficient energy collides (elastically or otherwise) with an atom in the target's lattice, transferring recoil energy to the lattice atom, forming what is known as a primary knock-on atom (PKA). This collision creates a Frenkel pair (vacancy-interstitial), and the resulting PKA has the potential to displace additional neighboring atoms, resulting

in a localized damage cascade. For highly energetic particles, one PKA may cause thousands of atomic displacements, while lower energy PKAs may case only a few (or none). “Radiation Damage”, from a materials standpoint, deals with the formation, clustering, mobility, and recombination (annealing) of these defects, and their effects on materials properties. Exactly how these cascades form, propagate, and anneal depends on the type and energy of the incident particle, as well as the intrinsic properties of the target material (bond strength, mass, etc) and its temperature.

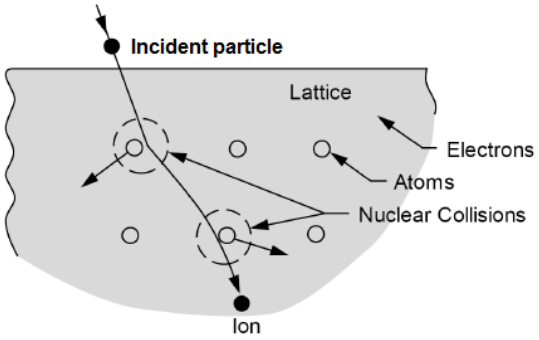

Figure 1.5. Illustration of Incident Particle Interacting with Medium16

In basic radiation interactions, not all of the incident particle energy is converted into kinetic energy; some inelastic effects, such nuclear interactions or electron excitation will also occur. Charged particles (e.g., ions) interact with matter electrostatically and immediately, losing energy rapidly and having relatively short penetration depths in solid media/ This is described as high linear energy transfer (LET). Neutrons, by contrast, being uncharged, tend to interact though nuclear reactions, and thus have low LET. For highly energetic radiation, the majority of displacement damage comes not from the initial PKA formation, but from the secondary damage cascade caused by the recoils.

In theory, the damage caused by two similar PKAs (of equal kinetic energy) will produce the same lattice damage, independent of what incident particle generated the PKA. Extending this theory further, it is tempting for one to attempt to correlate neutron damage to ion irradiation, hard spectrum/mixed spectrum system, fusion/fission hybrid systems, or pure fusion systems. Being able to quantify this mixed-source damage and correlate damage from various radiation sources would be highly valuable.

In practice, the density formation of PKAs is highly dependent on radiation interaction probabilities (and by extension, LET). Precise damage correlation between the charged and uncharged particles can be challenging because the production rate per unit volume and kinetic energy of PKAs vary among radiation types and energies. Additionally, interstitial ion implantation from the incident particles themselves have effects on defect clustering, and in neutron systems, activation, fission and transmutation cause the creation of additional point defect. In extremely high radiation damage environments, nuclear species transmutation causes void formation from the creation and accumulation of H and He.

Though it preferable to test potential fast reactor materials in a fast reactor spectrum, such irradiation presents a serious logistical problem. As of the time of this writing (2018), there are no fast reactors or fast neutron test facilities operating in the Western world. Geopolitical issues have made cooperation with the Russian Federation difficult, and Chinese and Indian Prototype reactors are used mostly for indigenous research. By any measure, fast neutrons are extremely expensive.

Due to these constraints, fast neutron irradiation is most often simulated using substitute fast neutron sources:

- Fusion neutrons (D-T or D-D fusion neutron source)

- Spallation neutron sources
- Fission neutrons (thermal and mixed spectrum)
- Ion irradiation with accelerators, and high-energy electron beams, etc.

Deuterium-Tritium and Deuterium-Deuterium fusion sources produce mono-energetic high-energy neutrons (14.1 MeV and 2.5 MeV, respectively), but the intensity is insufficient to build up appreciable damage in the material. Even high-intensity models may only ever achieve 10^{12} neutrons/s. Spallation sources use high-energy H^{-1} ions accumulated and accelerated to bombard metallic targets in pulses or a continuous beam and "spall" neutrons, which are subsequently moderated and used for scattering, time of flight, radiography, and other uses. Like fusion sources, spallation neutron sources are well suited for precision neutron measurements, but do not usually deliver the sustained intensities needed for causing significant lattice damage in steels. Thermal reactor cores and hard-spectrum locations in thermal reactor cores have been used to some extent for fast neutron irradiation, but they are designed for immediately moderating neutrons, and at the fluxes present in irradiation locations, realistic irradiations would take years. Finally, mixed-spectrum test reactors like Oak Ridge National Laboratory's High-Flux Isotope Reactor (HFIR) can produce high flux core locations with significantly hardened spectrums. At full power, HFIR can produce neutron damage on the order of 10^{-7} dislocations-per-atom (dpa)/s, which is about 4 months per dpa [17]. The unit of dpa will be more thoroughly defined and discussed in the following subchapter.

Irradiation source	Facility	Particles	Displacement dose rate (dpa/s)	He (appm)/dpa	H (appm)/dpa
Mixed spectrum fission reactor	HFIR	Neutron	1.1×10^{-7}	3.4	62
Mixed spectrum fission reactor	BR2	Neutron	4×10^{-7}	40	
Mixed spectrum fission reactor	HFR	Neutron	1.6×10^{-7}	20	
~~Fast fission reactor~~	~~EBR-II~~	~~Neutron~~	~~1.2×10^{-6}~~	~~0.15~~	~~2.3~~
~~Fast fission reactor~~	~~JOYO~~	~~Neutron~~	~~3×10^{-6}~~	~~0.17~~	
~~Fast fission reactor~~	~~PHENIX~~	~~Neutron~~	~~1.8×10^{-6}~~	~~0.3~~	
Accelerator/Cyclotron	PIREX	590 MeV proton	5×10^{-7}	100	800
Accelerator/Cyclotron	Single beam, HMI, Germany	M^{+}, 10-20 MeV proton, and α-particle	10^{-4}		100

Table 1.1. Irradiation Sources, types, and available damage rates. Crossed out entries are either shut down or not currently operating facilities[17].

By process of elimination, this leaves ion beam accelerators as the most viable option for delivering high-damage radiation (up to 100 dpa) in realistic time scales for experimentation. Being charged particles, ion beam irradiation offers the advantage of continuous irradiation and very high LET, as well as not activating the sample (because there is no neutron bombardment). The price paid for this high LET is very shallow penetration depth. According to SRIM simulations (covered later in this chapter), the peak particle penetration of 5 MeV Fe ions into Fe is around 1.4 micrometers. That makes heavy ion irradiation essentially a surface effect and precludes tensile testing of irradiated material. But investigating this surface with nanohardness measurements will reveal the changes in hardness/embrittlement of AM Grade 91 steel resulting from very high radiation environments.

This investigation used damage theory based radiation modelling to determine the critical irradiation parameters (particle type, energy, current, time, etc) to execute a pair of high-damage ion-beam irradiation of steel specimens. Upon calculating the necessary

parameters, the irradiation was carried out in the Ion Beam Materials Laboratory (IBML) at Los Alamos National Laboratory [18].

1.4. A Damage-Based Radiation Interaction Model

Early work in radiation effects testing tended to treat radiation damage to materials in terms of flux and time, total radiation dose, or total deposited energy. Experiments carried out with one material under a thermal neutron flux, for example, would produce vastly different results in harder spectra or fast neutron systems. While careful attention to the energy of the neutron flux could make results reproducible, such studies weren't able to provide a comprehensive or predictive model of radiation behavior. A truly quantum-level model of radiation interactions leading to damage within a medium would require a far more detailed understanding of the solid-state crystallographic detail of a system than is practical for engineering applications. In lieu of a truly first-principles model, damage theory attempts to treat radiation interaction in a practical manner, using a number of assumptions and empirical correlations [19]. In this sense, it is a hybridized approach to radiation interactions that takes into account initial particle (energy-dependent) flux, interaction probability, and describes radiation damage in terms of dislocations produced by incident radiation. It begins with a basic and generalized description of the number of dislocations (N_d) caused by in incident PKA:

$$N_d = N \int_0^t \int_0^E \varphi(E, t\,)\sigma_D(E_d) dE dt$$

Equation 1.1

Where:

N is the lattice (target) atom density (i.e., number of atoms/cm^3)

$\varphi(E,t)$ is the energy and time-dependent incident particle flux

$\sigma_D(E_d)$ is the displacement cross section for a particle at energy E

By dividing Equation 1.1 by the total number of lattice atoms an arbitrarily defined volume, this equation is normalized and reduces to:

$$dpa = \frac{N_d}{N \int dV} = \int_0^t \int_0^E \varphi(E,t)\sigma_D(E) dE dt$$

Equation 1.2

In this way, rather than a dose-based model, a *damage-based* unit normalized to atom density, deemed "displacements per atom" (dpa), is introduced. As an example, 1 dpa of damage means that on average, every atom in a control volume has been displaced once. Or, an average of 6.022 x 10^{23} (Avogadro's number) displacements per mole of target material.

The displacement cross section term, $\sigma_D(E)$, can be further refined into differential cross sections for both incident particle energy (E) and resultant recoil energy (T), in much the same way differential scattering cross sections are treated in nuclear reactor theory. For a mono-energetic incident particle (E), the dislocation cross section is defined in terms of the differential displacement cross section as:

$$\sigma_D(E) = \int_T^{T'} \sigma(E,T)\nu(T) dT$$

Equation 1.3

Where $\sigma(E,T)$ is the cross section for an incident particle with E resulting in a recoil atom with energy T;

$\nu(T)$ is the number of resultant displaced atoms the above collision;

In order to make practical use of Equation 1.3, $\sigma(E,T)$ and $\nu(T)$ must be converted into functions that are useful for engineering calculations. Though this general treatment for determining the density of dislocations is mathematically straightforward, in actuality, there are a number of difficulties in calculating each of the terms in Equation 1.3 explicitly, for each and every incoming and resulting recoil particle. In particular, high-energy particles with low mass can approach velocities at which relativistic effects are not insignificant, and there are additional inelastic energy losses that are difficult to calculate. Additionally, the generalized definition of dpa doesn't account for anisotropic scattering behavior (which may not be significant for short penetration depths), or crystallographic direction (angle of incidence with respect to lattice). Even equipped with such data, calculations of appreciable sample size would be computationally expensive.

To address this complexity, a simplified function was created by Kinchin and Pease to describe the number of displacements, $\nu(T)$, (based on threshold displacement energy) created as a function of incident PKA energy [20]. A number of assumptions were made for this model:

- Damage cascade is made by a sequence of two-body collisions between atoms

- When an atom with initial energy T emerges from a collision with energy T′ and generates a new recoil (E_R) such that no energy is transferred to the lattice. Thus, $T = T' + E_R$
- Energy loss by electron excitation/ionization is finite value (E_c). If the PKA energy is greater than E_c, no additional displacements occur until electron energy losses reduce the PKA energy to Ec.
- For all energies less than E_c, electronic stopping is ignored, and only atomic collisions occur.
- Energy transfer in atomic collisions is given by the "hard sphere" model (perfectly elastic collisions)
- Atomic arrangement (crystal structure) is ignored and considered random

Using the KP model, it becomes possible to calculate the number of displaced atoms formed as a function of incoming particle flux, energy, interaction cross section, and strength per bond of the target material [21]. By averaging the threshold displacement energies, adjusting for damage efficiency and energy available for elastic collisions, the number of dislocations for a PKA is given by:

$$N_d = \nu(T) = \begin{cases} \dfrac{\kappa(T - E_e)}{2E_d} = \dfrac{\kappa T_{dam}}{2E_d}, & T_{dam} > E_d \\ 1, & T_{dam} < 2T_{dam} < E_d \\ 0, & 0 < T_{dam} < E_d \end{cases}$$

Equation 1.4

N_d is the number of displaced atoms produced by *one* PKA

T is the recoil energy of a PKA;

E_e is the total energy lost by electron excitation;

k is the damage efficiency; Binary Collision Analysis (BCA) has determined this number to be around 0.8, and mainly due to ballistic processes recombining the defect immediately after formation

T_{dam} is the damage energy available for elastic collisions; It is equal to the initial energy (T) minus the energy lost to electron excitation/ionization (E_e)

E_d is the threshold displacement energy.

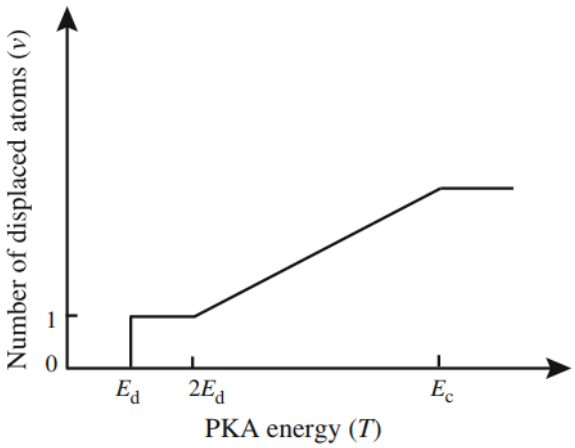

Figure 1.6 Visualization of Kinchin-Pease Linear Model for Calculation of Displacements as a function of PKA Energy[21]

While there have been modifications to the KP model that improve its accuracy for specific problems, it has been used successfully for decades to estimate radiation damage in a wide range of materials. Because of its simple displacement rate calculations, it is often used for the simulation of large numbers of particles. In this investigation, the KP model was used as the basis for the simulation 10^6 ions, which took fewer than 6 hours run on a

basic desktop computer. The simulation of Fe irradiation will be discussed later in this chapter.

From Equation 1.4 it immediately becomes apparent that the threshold displacement energy of the target material is very important in damage theory, and that particles or PKAs below the threshold energy (E_d) will cause no displacements. Thermal neutrons, for reference, have around 0.025 eV of kinetic energy and scatter readily, but do not on their own cause displacements in Fe, which has threshold displacement energies of 10s of eV (depending on incident angle). This is not to say that thermal neutron fluxes do not cause radiation damage to materials, however. In fission reactors, neutrons are born according to a thermal Maxwellian distribution with energies averaging around 2.4 MeV. These fast neutrons scatter elastically, causing dislocations in fuel, cladding, and reactor components. Additionally reactor core materials with high thermal neutron capture cross sections will absorb neutrons and transmute/decay, often with high Q-value nuclear disintegrations, leading to additional damage. It is also clear from Equation 1.4 that fast neutrons fluxes should be expected to cause orders of magnitude more damage than thermal neutrons per particle. It is this very fact that demands the high resistance to radiation for fast reactor designs.

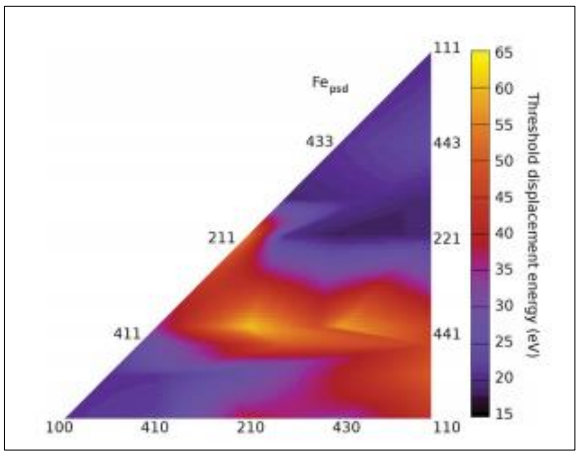

Figure 1.7. Threshold Fe Displacement Energy vs Crystallographic Direction[22].

2. Overview of Ferritic/Martensitic Steels in Reactors

The first consideration for industrial steels in reactor applications are their thermo-physical properties. These properties include high thermal conductivity, low/predictable thermal expansion, and advantageous mechanical properties (stress/strain relationships, hardness, strength, ductility). Additionally, a suitable steel must maintain these intrinsic properties to some degree throughout its design life. Because material properties are ultimately driven by the material's microstructure, changes to the microstructure will necessarily cause material properties to change.

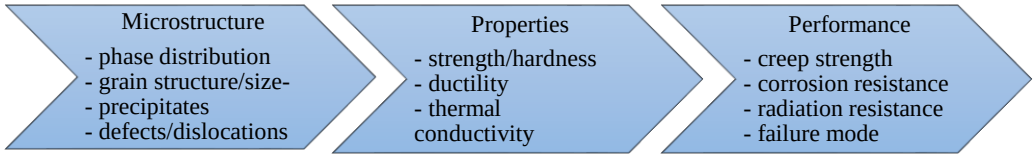

Figure 2.1. Illustration of microstructure, properties, and performance relationship

In some cases, materials with initially desirable beginning-of-life properties are irreversibly damaged when subjected to corrosive or oxidizing environments, high temperatures, high pressures, or intense radiation fields. For this reason, alloyed steels and stainless steels utilize alloying elements that improve properties of the steel (e.g., the addition of Cr to form a thin oxide layer to prevent subsurface oxidation).

The long-term phenomenological changes that occur in steels, such as creep, fatigue, and corrosion, are the result of the microstructural evolution and chemical reactons brought on by stresses, chemical/thermodynamic interactions, radiation damage, other interatomic phenomena, and combinations thereof.

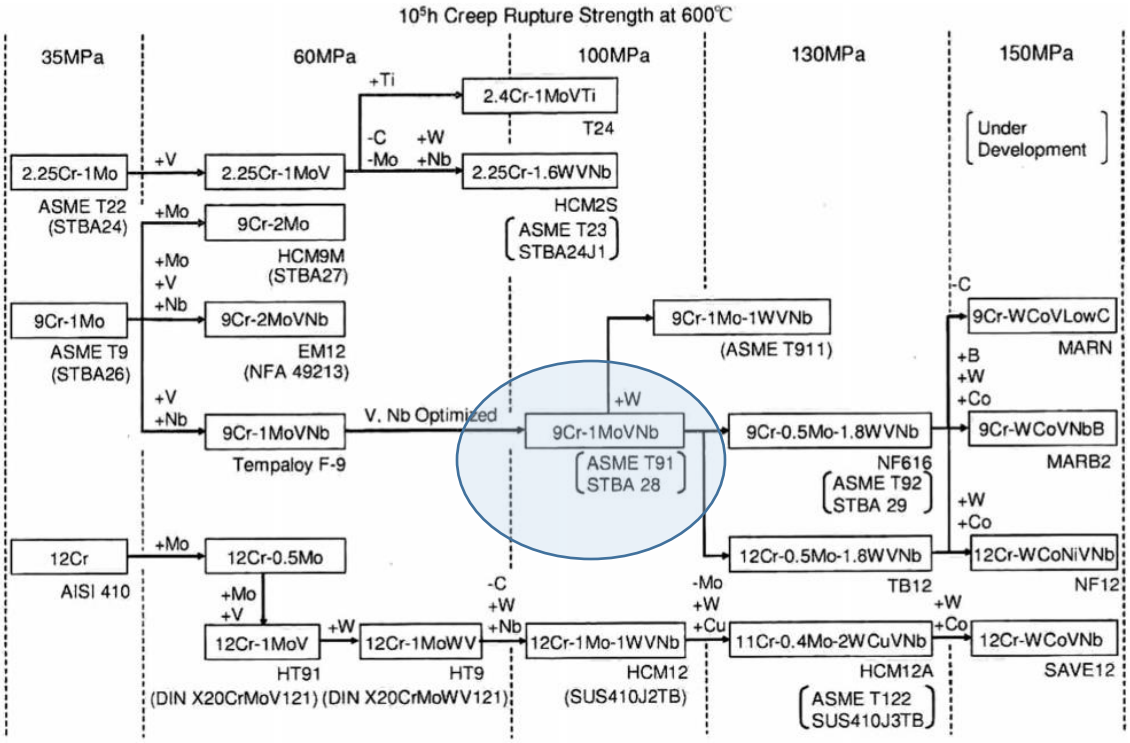

Figure 2.2. Family of high chromium creep strength enhanced FM alloys [23].

The first generation of high-chromium alloyed steels (Cr-Mo steels) was simple combinations of 12% Cr (AISI 410) and 9-12% Cr-Mo (ASME T-9) compositions. The drive to achieve higher profitability margins in traditional power plants pushed for improved plant efficiencies by increasing their operating temperatures. Improvements in metallurgy, materials science, and fabrication enabled the development of more optimized and highly alloyed steels with high performance at elevated temperatures and increasingly enhanced creep-rupture strengths. Namely, micro-alloying traditional Cr-Mo steels with V, Nb, W, and Oxide dispersions has led to the development of a family of Creep Strength Enhanced Ferritic (CSEF) steels with vastly improved strength and durability in high-temperature applications. Because of these advances the maximum temperature of boilers has been increased from below 450 °C to nominal operating temperatures of 620°C, and 10-year creep-rupture strengths to be increased from 40 to 140 MPa [23].

These high-chromium alloyed steels were considered for fast breeder fission reactors in the early 1970s and then in the late 1970s for fusion applications. The steels became of interest because of their swelling resistance compared to austenitic stainless steels, which had been the primary candidates for both fast reactors and fusion applications up to that time [24, 25].

In addition to high thermal performance and chemical resistance, the exacerbating factor of irradiation and neutron absorption/activation became a concern for fast reactor materials for a number of reasons. Firstly, neutron economy is particularly important in fast reactors, where absorption and fast non-leakage probability play a major role in criticality. Several metals, most notably Ni, have appreciable neutron absorption cross sections and tend to act as neutron poisons; these absorptions lead to activation of the components and significantly compound the cost, safety considerations, and technical ease of disposing of highly radioactive components after decommissioning. These considerations all but preclude Ni-based alloys from the primary systems in fast reactors. For this reason, low-activation FM alloys like Grade 91 are still considered leading candidates for fast reactor development.

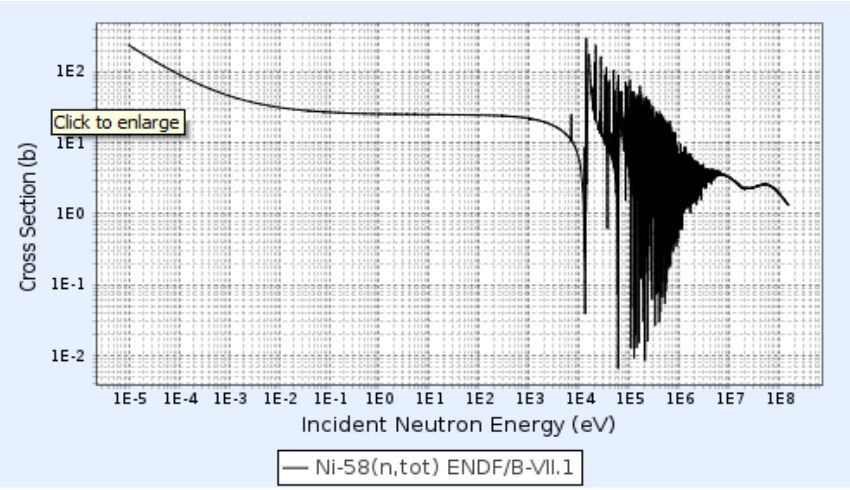

Figure 2.3. Neutron cross section of Ni-58 (68% abundance)[26].

2.1. Crystallographic Structure and Phase Diagrams

Martensitic steels are so called because they contain a crystallographic structure containing a microconsituent phase, known as martensite. The martensitic transformation is a type of diffusionless transformation in Fe-C systems in which its ferrite (α phase), a body centered cubic (BCC) phase, is heated to a high temperature (above 1000 °C), dissolving carbon and forming austenite (γ phase), a face centered cubic (FCC), then rapidly cooling (quenching) the carbon-saturated Fe-C system. This quenching forms martensite (and solid solution strengthening) as the C is retained as interstitial impurities, inhibiting the (time-dependent) C diffusion, and preventing the formation and precipitation of carbides. The resulting structure (martensite) is body centered tetragonal (BCT) supersaturated phase in a high internal stress state and high dislocations density, forming a characteristic martensitic lath (or "needle") grain structure [27]. Owing to this high-dislocation density structure and stress state, pure martensite is very hard and very brittle.

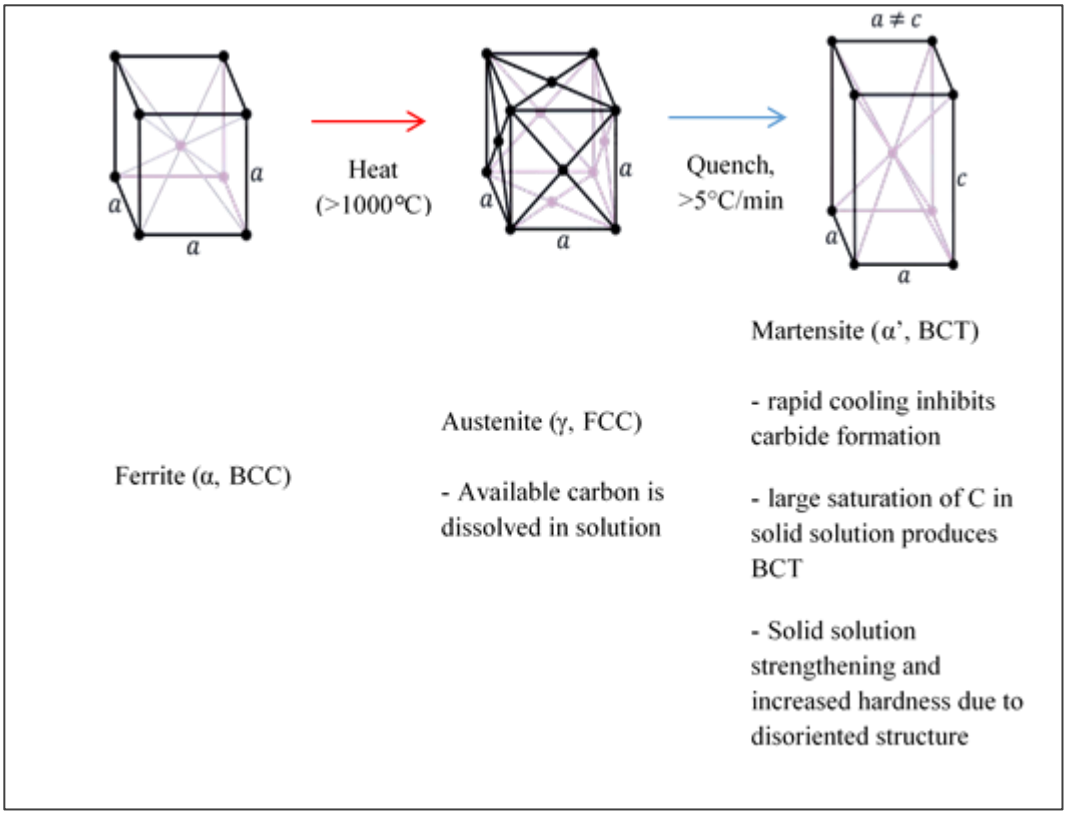

Figure 2.4 Illustration of diffusionless martensite transformation from ferrite.

The heat treatment used to austenitize and then quench (to room temperature) ferritic alloys is known as normalization, and will be discussed in greater detail later in this chapter. After normalization, an additional lower temperature heat treatment (tempering) is carried out, which relieves internal stresses, decrease hardness, and allows the saturated C in martensite to precipitate out, mostly in the form of carbides, returning the martensite lattice structure to ferrite BCC. This tempered martensite has ferrite crystallography, but has retained it martensitic grain structure. The precipitates formed during tempering are mostly $M_{23}C_6$-type carbides, with a smaller concentration of MC, nitrides, and other precipitates, collectively referred to as MX precipitates.

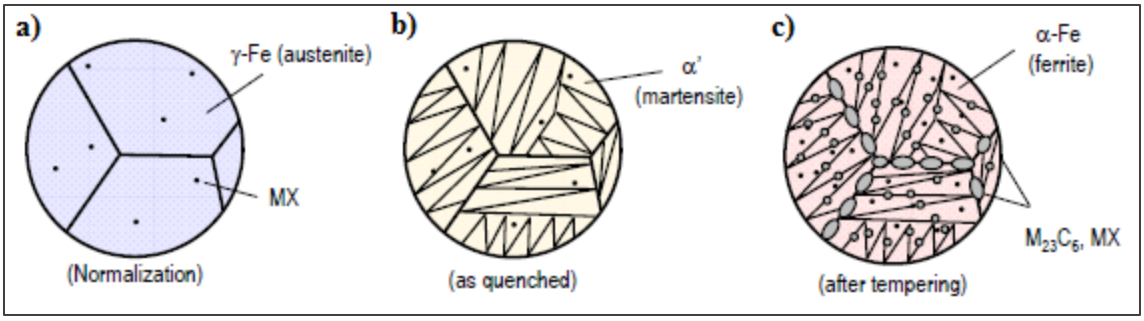

Figure 2.5. Illustration of a) austenitized grain structure; b) quenched martensite lath grain structure; c) tempered martensite (Ferrite composition in retained martensite lath structure), with M23C6 carbides along grain boundaries[6].

Because martensite is a non-equilibrium phase, it does not appear explicitly in an equilibrium phase diagram. Instead, Continuous Cooling Transformation (CCT) diagrams are often used for heat treating steel. In order for the martensite transformation to occur, it must happen quickly.

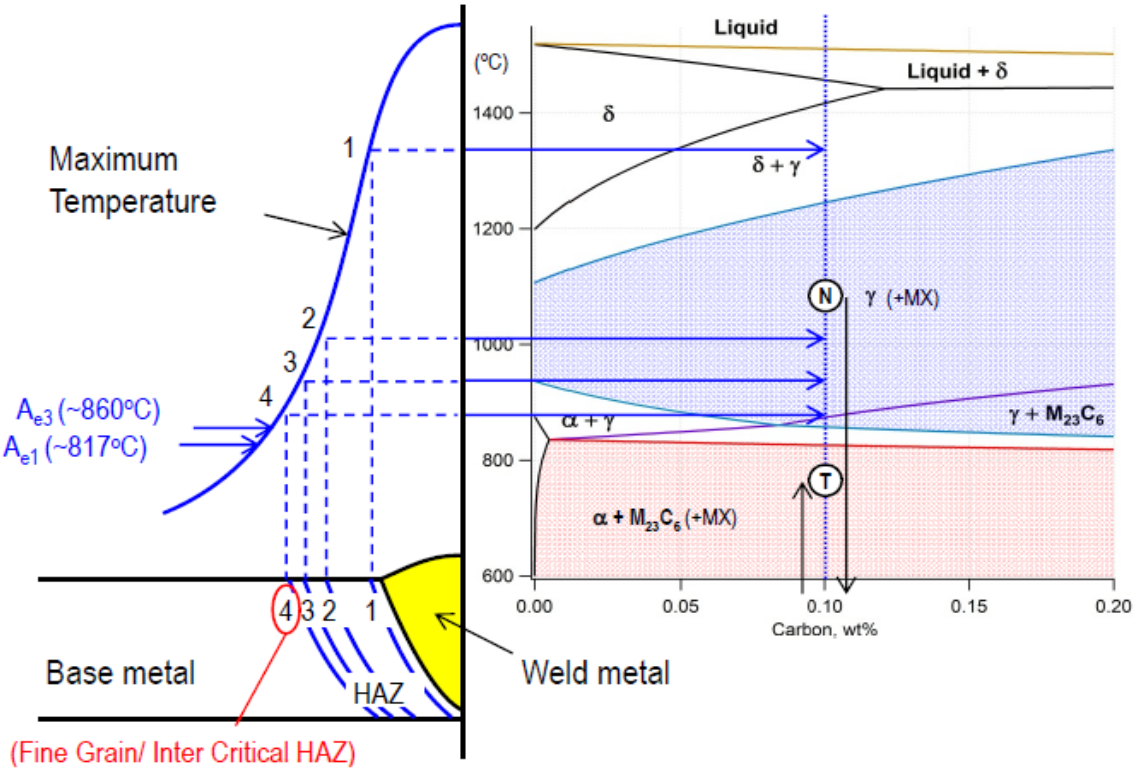

Figure 2.6. Phase diagram showing normalization and tempering regions for Grade 91 steel[6].

Though there will be some diffusion of carbon, the austenite to martensite transformation occurs very rapidly (approximately Mach 0.5) and the carbon is retained in the martensite, which exhibits a characteristic lath structure [27].

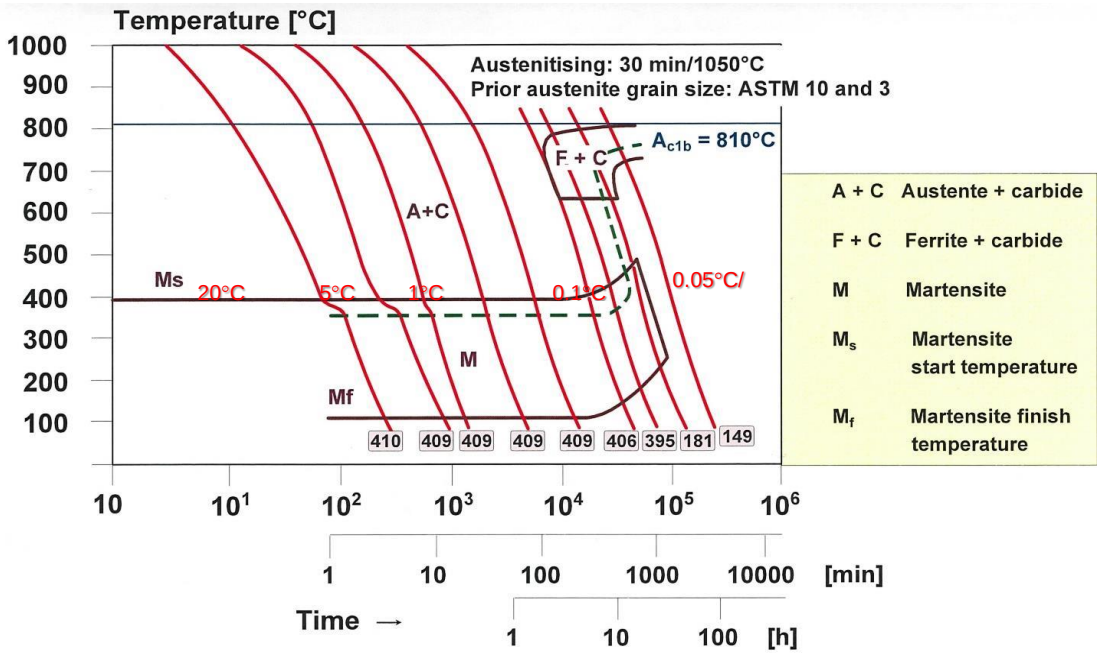

Figure 2.7. CCT phase diagram for martensite formation in FM steels[28].

Grade 91 steel, after its heat treatments, is composed of delta ferrite, tempered martensite (ferrite within the previous martensite lath structure), about 1.5 – 2% precipitates (mostly carbides), and some retained austenite [29].

Studies have shown thermal aging to cause microstructural changes above 450 °C, and Fe_2Mo Laves phase precipitation has been observed along grain and subgrain boundaries aging at 600 °C [30, 31, 32]. Laves phase presence has been shown to produce some strengthening in the early stages of the creep-rupture tests, but this decreases as a result of coarsening of the particles, and as available Mo in solution when these elements are incorporated into precipitates [33].

2.2. Grade 91 FM Steel

The “91” in Grade 91 refers to alloyed steel with approximately 9% Cr and 1% Mo, and small amount of other alloying elements. A robust body of knowledge on traditionally wrought Ferritic-Martensitic (FM) steels has been assembled over the last several decades. Grade 91 Steel, as it is so named, refers not to the original 9Cr-1Mo alloy, but to the commercially available product sometimes known as “modified 9Cr-1MoVNb”, P91 (for pipes), or T91(for tubes). In widespread industrial use, Grade 91 steel is usually referred to by one of its ASTM (or ASME) coded descriptors, which takes into account its intended end use and prescribed heat treatments. Commercial grade heater tubes, for example, may be designated A213 (SA213), while A387 (SA387) describes the same material, but in pipe form (higher thickness) [34]. European Norms (standards) label the material EN-10216. Inasmuch as these descriptions are precise, they assume their designated material is not only of code-sanctioned composition, but fabrication method, and heat treatments and well. AM material would not meet the strict definition for an ASTM number, so all material in this investigation is referred to by the generic term “Grade 91”, whether wrought or AM, and regardless of its heat treatment.

As with all FM steels, Grade 91 steel’s characteristics are derived not simply from its chemical makeup, but from its fabrication method and post-fabrication heat treatments as well [12]. By established ASME metallurgical standards, Grade 91 steel is melted, cast, formed into wrought products, and heat treated in a precise manner to achieve just the right microstructure and properties. Direct Metal Laser Sintering (DMLS), on the other hand, is an AM technology that builds a part directly by sintering or melting constituent powders with a precisely controlled laser. DMLS has been successful in producing parts from pure

metals and simple alloys, but to date, there is no known instance of Grade 91 steel being fabricated into parts using such AM methods. It is unknown to what extent the unpredictable heating patterns experienced during fabrication might affect the microstructure, properties, and performance of Grade 91 steel, whether such effects might be rectified with post-fabrication heat treatments, and how such steel might be affected by extreme radiation damage.

2.3. Thermal Properties of Grade 91 Steel

Though Grade 91 steel was originally developed for use in Liquid Metal Fast Breeder Reactors (LMFBRs), its high creep strength and chemical stability have led to its adoption and widespread use by the fossil fuel industry. Today, the majority of its commercial use is currently in boilers, pressure vessels and piping in fossil power plants [29].

Tempered martensitic Grade 91 steel is strengthened by three mechanisms to resist creep and deformation in general: i) solution hardening (e.g., Mo), ii) dislocation hardening (strain hardening), and iii) precipitation hardening (carbides, nitrides, and carbo-nitrides) [35].

2.3.1. Density and Thermal Expansion

The density of wrought Grade 91 varies linearly with increaing temperature (due to thermal expansion) between 7.73 g/cm3 and 7.54 g/cm3 at 20 °C and 600 °C, respectively [36]. Grade 91 compared to 316 Stainless Steel has slightly lower density and a significantly lower mean themal expansion coefficient (~12.5 $x10^{-6}$/°C) at 600 °C. This

results in a lower thermal induced stress for the same temperature gradient in the two steels [37, 38].

2.3.2. Heat Capacity and Thermal Conductivity

Grade 91 steel's thermal conductivity is significantly higher than 316 steel's. At 600 °C, their respective thermal conductivities are around 28 and 20 W/m °C, though 316 steel has a slightly higher specific heat [39-41].

2.4. Strengthening Mechanisms in Grade 91 Steel

In FM steels and Grade 91 steel in particular, there are three main strengthening mechanisms associated with resistance to creep deformation. As discussed in subchapter 2.1, the martensite transformation itself results in solid solution strengthening due to the supersaturation of carbon in the martensitic BCT structure. Additionally, the tempering process results in the formation of carbides, nitrides, and carbo-nitrides, which precipitate at the grain boundaries and resist sliding dislocations. It is worth noting that as precipitation occurs during heating/aging, it depletes species in solution. Thus, solid solution strengthening tends to decrease as precipitation hardening increases [42-44]. The third mechanism, which is important in all ductile material strength analysis, is strain hardening (also known as work hardening, or cold working). Material behavior and its effects on these three strengthening mechanisms will be discussed throughout this dissertation.

In addition to the previously discussed mechanisms, dispersion strengthened steels also show great promise. Dispersion strengthened steels, or more specifically, oxide dispersion strengthened (ODS) steels, are capable of retaining strength at much higher temperatures than traditional FM steels [49, 50]. By dispersing oxide powders during

fabrication, it is possible to maintain a very small (<1 μm) grain size. According to the Hall-Petch correlation, and the uniaxial creep-rupture strengths and ductilities are enhanced when these grains have a high aspect ratio (length to diameter ratio greater than 15) [49, 50]. Being oxides, the high melting temperatures in ODS steels also mean that they are not susceptible to rapid dissolution, as happens with precipitates at higher temperatures.

Early ODS steels were high (12 to 17%) Cr non-transformable ferrite matrix with a high concentration of small high-melt temperature oxides: titania (TiO_2) and/or yttria (Y_20_3) particles as the strengthening dispersion. Elevated-temperature strength is provided by the titania and yttria particles and by x-phase (70% Fe, 15% Cr, 7% Ti, 6% Mo) that forms at grain boundaries. Irradiation testing on ODS steels shows that having a density of grain boundaries to act as sinks, these steels and variations on these steels generally show excellent resistance to swelling under both neutron [51-55] and heavy ion irradiation [56, 32].

While ODS steels show promise, AM methods it is not clear that AM would be effective in making such alloys. Because of the difference in sintering temperature for metals and oxides, laser sintering techniques may not be able to sinter such structures together, but may instead, melt the metallic constituent while sintering or dispersing the oxide. Whether this is feasible, and whether it could produce even dispersions is the topic of ongoing research [57], but will not be evaluated in this dissertation.

2.5. Creep Analysis of FM Steels

Creep is simultaneously one of the most important and one of the most difficult to analyze material behaviors. It is generally accepted in the fast reactor community that creep

is the most salient lifetime limiting factor for structural materials, including advanced reactor core components. In general terms, creep is defined as the time-dependent deformation (strain) of materials under static mechanical stresses and/or elevated temperatures. While these stresses are less (often far less) than the yield stress of the material, static stresses (mechanical and thermal) can occur though a number of deformation mechanisms, including:

- Grain boundary slip
- Dislocation glide/dislocation climb
- Vacancy or dislocation diffusion

The effects of these creep mechanisms can be exacerbated by irradiation effects, and the combined effects of such interactions are still being understood. The above behaviors have been studied phenomenologically to produce empirical models of deformation-based creep and diffusion-based creep. For this investigation, the activation energies and proportional constants for the empirical models are not understood for AM Grade 91, and since this dissertation is the first known evaluation of creep strength of such material, it will focus on an engineering-level approach to creep.

In engineering practice, temperature-driven creep becomes important when metals and alloys reach around 40% of their melting temperature (T_m, in K) [27]. The Fe-Cr phase diagram shows a liquidus melting temperature of ~1500 ºC observed in G91 steel, indicating that a Grade 91 steel specimen would be considered vulnerable to creep around 425-450 °C, which is certainly within service temperatures of fast reactors (300~600 ºC) [41].

A standardized ASME creep test is carried out by hanging a weight from a tensile specimen and observing the creep rate as a function of stress (in this case the gravitational force divided by the specimen's cross sectional area) at different specified temperatures [58]. For a steady state creep rate of 10^{-5}/hr, this would mean a creep rupture test (assuming ~20% elongation) would take 20,000 hours, or over two years' time. Such a test presents a challenge for data collection from a time and money perspective, and a this investigation instead used a variable strain rate analysis and extrapolation methods to assess the creep behavior of Grade 91 steels.

Typically, creep from constant load (at a specific temperature) presents itself in three distinct phases. The primary phase is characterized by a decreasing strain rate, which is related to the increase the material's resistance to plastic deformation. In the secondary phase, a given stress causes the competing phenomena of strain hardening and recovery, resulting in a constant strain rate (manifested as a linear slope in Figure 2.8). In the Tertiary creep phase, the material experiences on-uniform elongation, accelerated deformation, necking, cavitation, and rupture (failure) [27]. Secondary creep is the longest in duration, and the most important of these phases from a material properties standpoint. Because it represents the creep behavior in which strain hardening and recovery are competing, a larger strain hardening region will generally result in a longer secondary creep regime.

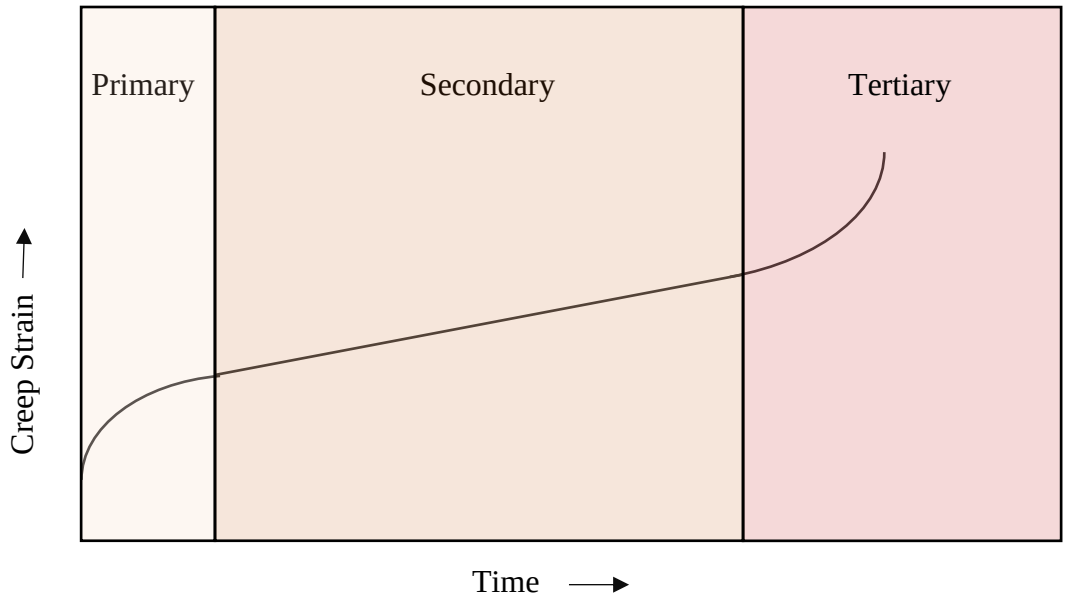

Figure 2.8. Illustration of Creep Stages

Observing a linear creep strain vs time response under a specific stress (or temperature) indicates that the material is experiencing a constant strain rate. This constant strain rate, known as the steady-state creep rate ($\dot{\varepsilon}_s$), can thus be expressed under isothermal conditions as a function of stress by using the following empirical function [27]:

$$\dot{\varepsilon}_s = K\sigma^n \qquad \textbf{Equation 2.1}$$

In this form, logarithmic plots can be used to generate *K* and *n* (known as the stress exponent) from data for a range of strain rates and stress values. In order to determine the steady-state creep rate of a material, a dataset must be generated in which a constant strain rate is generated for a specific stress. In Chapter 4, the specific methodology used in this experiment will be discussed.

The creep strength of wrought Grade 91 steel is evident in its observed time-to-rupture behavior, shown in Figure 2.9. The observed 10^5 h (~11 years) time to rupture at 600 ºC is around 80 MPa. Additional creep tests on Grade 91 steel by Srinivasan et al. [60] have calculated 10^5 h time to rupture stresses of 87 MPa at 600 ° C.

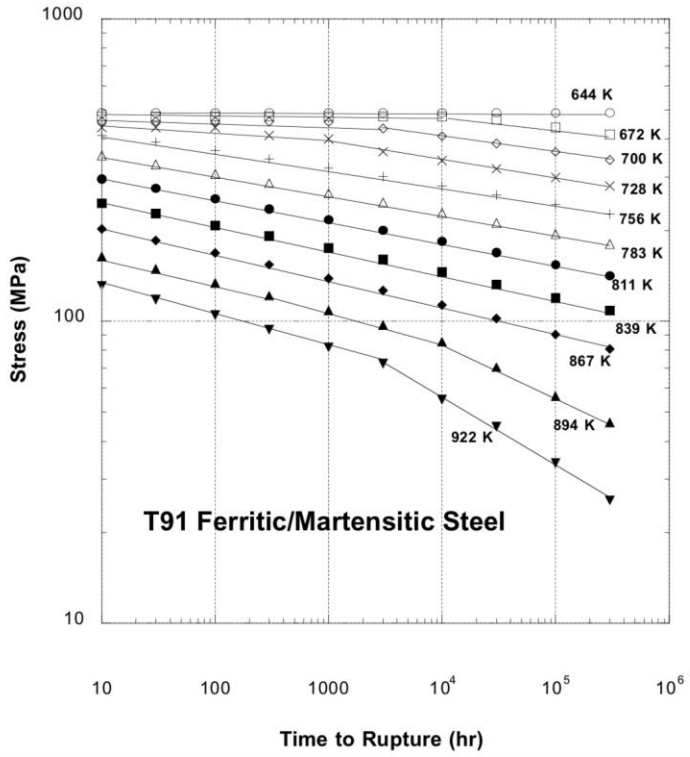

Figure 2.9. Time to rupture for ASME Grade 91 Piping [59]

2.6. Chemical and Corrosion Effects in FM Steels

Throughout their history, FM steels have been used with a wide variety of working/cooling fluids in a number of chemical environments, though the majority of commercial utilization of FM steels has been in the water-steam systems of power plants. Regardless of cooling medium, corrosion and oxidation are primary concerns from a component longevity and safety standpoint.

2.6.1. Aqueous Corrosion in FM Steels

As part of research and down-selection, an extensive number of studies have been carried out (mostly in the 1970s and 1980s) to quantify the corrosion rates of candidate FM steels in water for reactor heat exchanger systems [61-63]. High-Cr FM Steels have been shown to generally have superior waterside corrosion resistance to low-alloy steels (such as those from which the reactor pressure vessel is made) [64], but inferior to that of austenitic steels (such as 316L stainless steel) in well chemically controlled environments [65-67]. However, protective oxide films formed on austenitic steels can be degraded under heat and salinity conditions. This requires that austenitic steels in aqueous high-temperature must remain in very pure conditions. Additionally, fully tempered FM steels that don't contain austenite-stabilizing elements (e.g, Ni, Cu, and Co) have been shown to be virtually immune to transgranular stress corrosion cracking (SCC) in aggressive environments [68]. For this reason, FM steels can be considered superior in environments where water purity is difficult to control [69].

2.6.2. Steam and Air Oxidation of FM Steels

Grade 91 steel forms surface scales when oxidized in air at temperatures below 650 °C. These surface scales are protective and adherent, consisting of $(Fe,Cr)_2O_3$ and $(Fe, Cr, Mn)_3O_4$ [70]. These scales are observed to be thicker, and more prone to spalling in steam environments. Additionally, internal oxidation of Cr to form $(Fe,Cr,Mn)_3O_4$ occurs at the martensite lath grain boundaries. For these reasons, Grade 91 steel is considered unsuitable for long-term operation of as superheater or reheater tubes at high temperatures (above 650 °C) [71]. For such operation, higher Cr (12%) alloys may be more appropriate. This study

is focused with Grade 91 steel as a nuclear material, as opposed to a secondary side material.

2.6.3. Liquid Sodium Compatibility with FM Steels

Due to its initial development with SFRs in mind, Grade 91 steel is known to be compatible with liquid sodium at low oxygen concentrations. Still, a number of studies have been carried out to determine the corrosion and transport characteristics of FM steels under high fluid velocity/high temperature conditions (as duct and cladding materials). Anantatmula conducted an experiment with 9-Cr 1-Mo steel run at 600 and 650 °C in a liquid sodium loop at a velocity of 6.0 m/s (4×10^4 Reynold's number) [72]. The oxygen concentration was 1.0 +/- 0.2 ppm. Tests were run 4000 h at 600 °C and 8000 h at 650 °C. Both the austenitic and FM metals in the loop showed excellent sodium compatibility; the 9-Cr 1-Mo exhibited 0.70 μm loss in thickness due to corrosion, which was less than half that of the austenitic 316 steel. Additional mechanical studies have shown specimens exposed to liquid sodium to have little to no change in their creep rupture time, as shown in Figure 2.10.

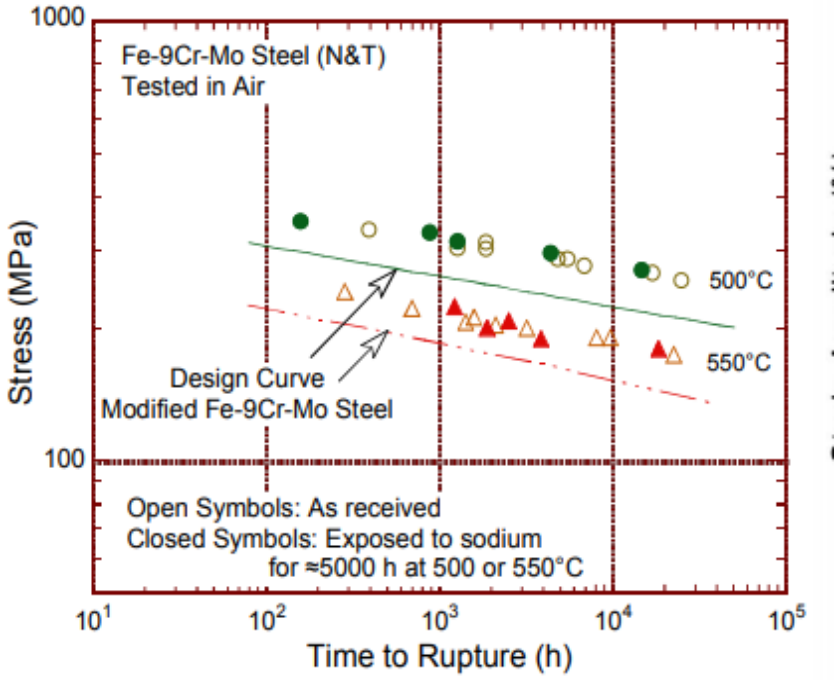

Figure 2.10. Creep rupture time of Na exposed Grade 91 steel [73].

2.7. Radiations Effects in Ferritic/Martensitic Steels

Radiation damage (dpa) is manifested in a sense by defects, which can cluster together, migrate to sink locations (grain boundaries, dislocations, etc.), recombine, or accumulate to form defect clusters, and ultimately voids. Because the sinks' ability to capture defects is driven by temperature, understanding displacement rate (function of incoming radiation), rate of collection at sinks (function of material and temperature), and recombination rate are very important in determining the long-term stability of a material. As defects build, they begin to affect microstructures, causing phenomena such as void swelling, irradiation-induced segregation (separation of chemical species), embrittlement, and radiation-induced creep.

In general, experience with steel irradiation indicates that at low temperatures, even at very low dpa, hardness and embrittlement increase, while ductility decreases. Depending on temperature, damage rate, and other factors, defect formation can outpace annihilation, and defects may cluster and form voids, leading to phenomena like increased ductile to brittle transition temperature and radiation-induced embrittlement [23]. As dpa continues to increase, longer-term phenomena like void swelling and radiation-induced creep can occur. The mechanisms that drive these phenomena have been observed, but first principles understanding of their generation and behavior is an ongoing field of study.

Figure 2.11 illustrates the rough temperature regimes and dose rates at which particular radiation-induces phenomena are known to occur.

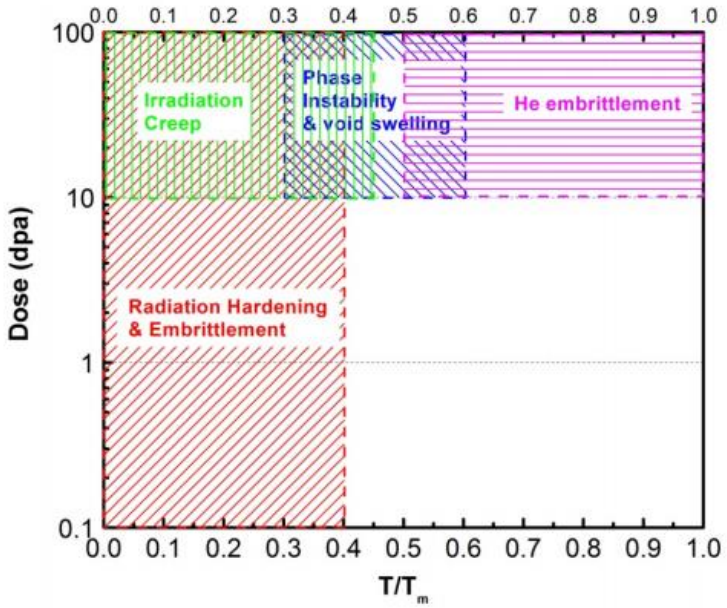

Figure 2.11. Map of radiation-induced microstructural effects and their observed regimes[74].

Even with facilities capable of fast neutron irradiation, conducting irradiation experiments over wide ranges of dose, temperature, and composition are time and cost

prohibitive. Therefore, most mechanical experiments in this field consist of using one steel type (composition) irradiated over a temperature and fluence range that is limited by the conditions of the facility. Because of this, current research in the study of FM steels under irradiation is limited to literature data and ion irradiations, and most experiments already carried out are not repeatable without fast neutron sources. This makes comprehensive knowledge of separate effects (e.g., embrittlement) of irradiation a difficult task, making quantitative comprehensive comparisons difficult. But, by using a combination of legacy data and ion irradiation data, this experiment was successful in irradiating AM Grade 91 steel for the first time, measuring its nanohardness, and comparing that result to wrought material.

2.7.1. Hardening and Embrittlement

As discussed in Chapter 2, irradiation temperature directly affects the magnitude of irradiation hardening in FM Steels. Though there are limited studies on the irradiation of Grade 91 material, early experiments by Klueh (et al.) involved long-term irradiations at the EBR II reactor in fluxes of ~2 x 10^{26} n/cm^2-s, resulting in total damage of approximately 12 dpa. It was shown that at after low-temperature irradiation (below 400°C), Grade 91 steel experienced significant irradiation-induced microstructural changes that led to lattice hardening, with an accompanying increase in strength [75]. The effect of this hardening decreases with increasing temperature, and its effects were no longer apparent by irradiation at 500 °C.

The hardening at 390°C was attributed to the dislocation and precipitate structure formed during the irradiation. The lack of hardening at 450°C and higher correlates with an absence of an irradiation-induced damage structure. The observed low-temperature

irradiation hardening was accompanied by a decrease in strain to failure (total elongation) at 400 °C test temperature, from 6% (unirradiated material) to 4.1%. This effect was nullified in the 500 °C irradiation temperature sample, which had a slight increase in strain to failure. This study also found no change in performance from thermal aging in unirradiated Grade 91 specimens [75].

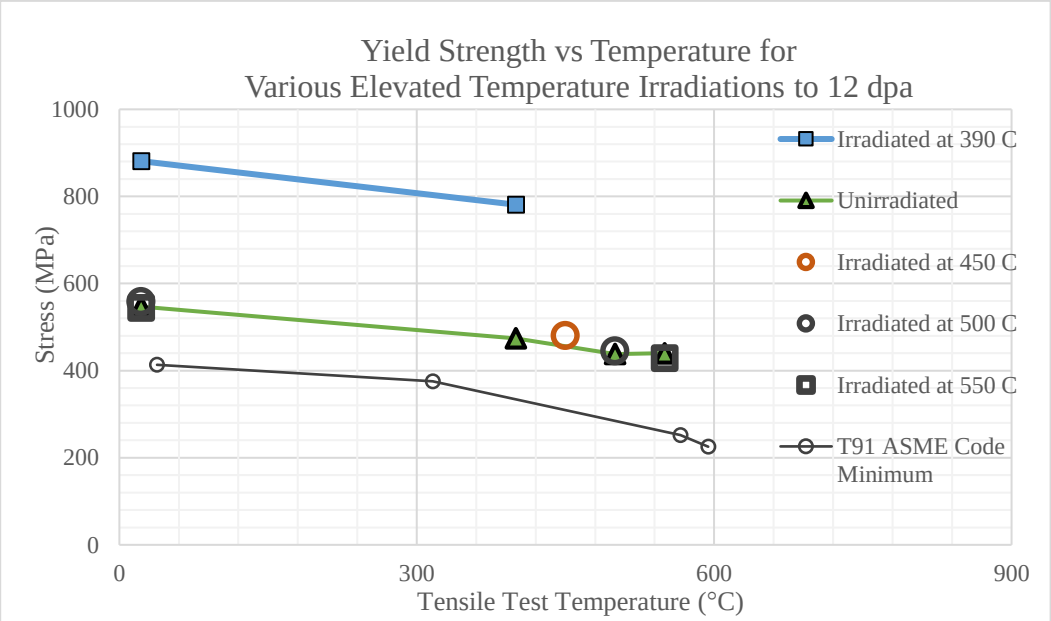

Figure 2.12. Yield Strength vs Test Temperature Plot of 12 dpa Specimens at Various Irradiation Temperatures[75].

2.7.2. Irradiation Creep

In addition to conventionally induced creep, it has been shown that time-dependent plastic deformation can also occur at much lower temperatures when subjected to both stress and irradiation [23]. This phenomenon is known as “irradiation creep”, and though it seems to be independent of temperature, it has been shown to be proportional to irradiation damage (dpa) [76]. Phenomenologically, it is attributed to the supersaturation

of point defects resulting from displacement damage. Radiation creep and void formation are related in that they both involve the redistribution of point defects and the evolution of the microstructure.

Irradiation creep has been studied for FM steels between 60 – 600 °C, at doses in excess of 200 dpa. For Grade 91 steel irradiated 400 C in HFIR, a diametral strain of ~1.2% was observed after 100 dpa. Of this approximately 0.25% was calculated to be from swelling, while the remainder from irradiation creep [23]. Increasing the dose to 200 dpa at the same stress resulted in a diametral strain of ~1.8%, with 0.7% from swelling. However, at 50 dpa the total strain was only ~0.25%, almost entirely the result of irradiation creep. These studies also suggested that irradiation creep is virtually independent of temperature [76].

2.8. Fracture Surface Analysis of Steels

SEM is often used for the analysis of post tensile testing fracture surfaces. In general, these micrographs can provide a qualitative analysis of the behavior of a material at the point at which it fails. Metals may fracture in highly ductile manner, in a brittle manner, or may exhibit characteristics of both ductile and brittle fracture. In evaluating AM steel for engineering applications, ductile fracture is desirable, and it is valuable to compare the fracture behavior of AM vs wrought material.

2.8.1. Ductile Fracture

The most obvious indicator of ductile fracture is the necking down/elongation of the specimen at the site of the fracture. The narrowing of the cross section of the specimen

is clear from images (Figure 2.13) that show the fracture surface is significantly smaller than the pre-test cross section (e.g., reduction of area).

In addition to elongation, ductile fracture generally exhibits the following characteristics:

- Considerable plastic deformation in the fracture region, specifically, in the necking region
- Fracture surface is often not related to the direction of principle stress, as it is in brittle fracture (due to shear stress)
- Characteristic appearance of fibrousness and dullness, owing to deformations on the face of the surface

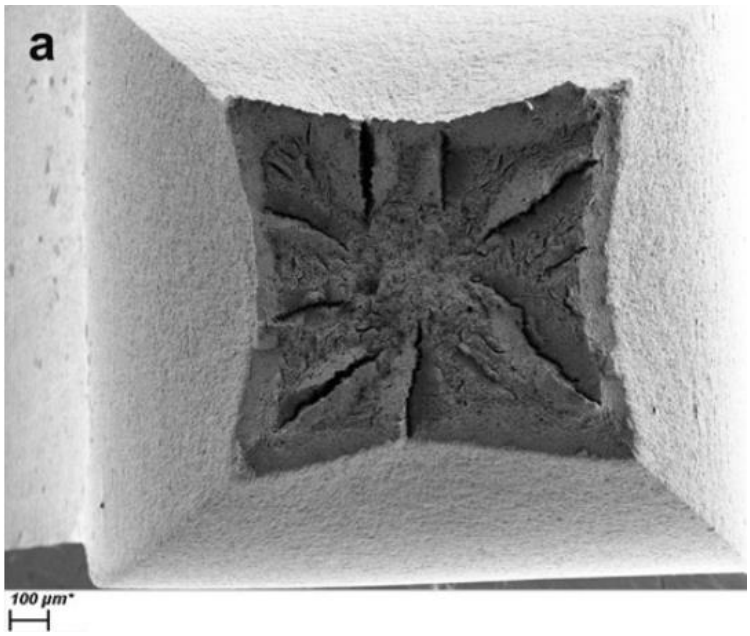

Figure 2.13. Fracture Surface of T-91 Steel [77].

The classic model of ductile fracture is the cup-and-cone model [27], which describes the convex/concave mating surfaces of the respective faces. Deformation, rather than being along tensile load direction, is dominated by shear stress. The shear stress reaches a theoretical maximum at around a 45° with the tensile load.

In a predominantly ductile fracture, the fracture itself originates as many tiny internal fractures, known as microvoids, near the center of the specimen cross section. These voids are indications that the UTS has been reached, and they would be expected to be observed in a specimen as soon as the stress-strain curve has passed its maximum, and the applied stress (in a constant strain rate test) begins to decrease.

As the fracture originates near the center of the reduced section, it spreads outward toward the surface of the necked-down area [77]. Before the fracture reaches the surface, however, it suddenly changes direction from generally transverse to the previously described 45° shear angle. This is known as the shear lip, and produces what is often called a slant fracture. In sufficiently thick samples, a slant fracture is useful in indicating the end of the fracture process at that location. As the thickness increases, however, the percentage of slant fracture around the central origin area will decrease, sometimes resembling a "picture frame," on a relatively thick rectangular specimen.

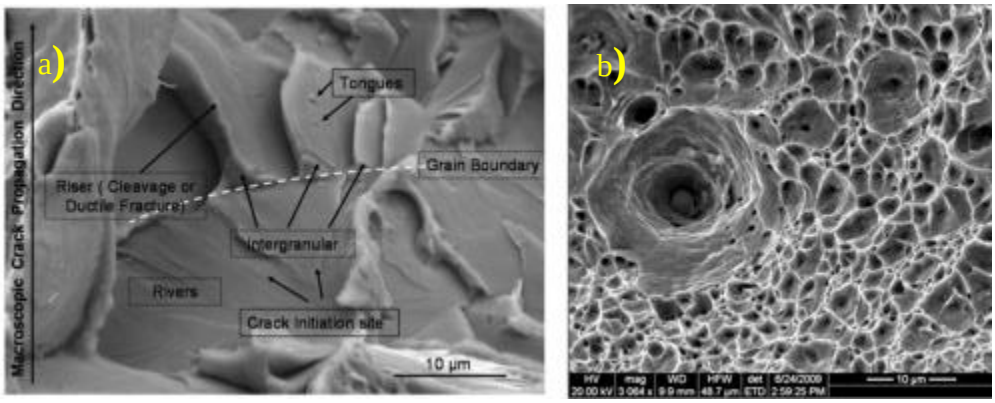

Figure 2.14 Cleavage-type (Brittle) Fracture (a), and Transgranular (Ductile) Fracture (b) at high magnification[78].

In tensile testing, fracture loci and crack growth resistance are also dependent on temperature and strain rate. Typically, strain at fracture increases with increasing

temperature in Fe, Cu, Al, and Mg alloys [79]. However, some austenitic and ferritic steels show the reverse, becoming less ductile until reaching a ductility minimum, after which strain at failure then increases again [80]. Other than at dynamic strains (high strain rates), strain at fracture in steels has, in general, been shown to decrease with increasing strain rate.

2.8.2. Brittle Fracture

Brittle fracture is undesirable in virtually all engineering applications, and especially for metals. Brittle materials tend to experience very little plastic strain between their YS and UTS [81]. Brittle fracture is characterized by little to no elongation of the specimen, and includes both cleavage-type fracture and intergranular cracking.

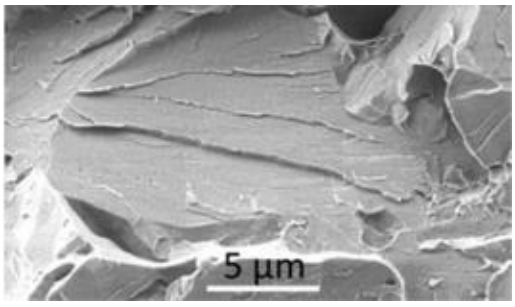

Figure 2.15. Cleavage fracture in low alloy steel[81].

Embrittlement, caused by excessive defect formation due to diffusion of H, He, or other gases, or excessive formation of voids due to irradiation can cause cracking behavior. Embrittlement of Grade 91 material has also been found to occur under conditions of critical hydrogenation [77].

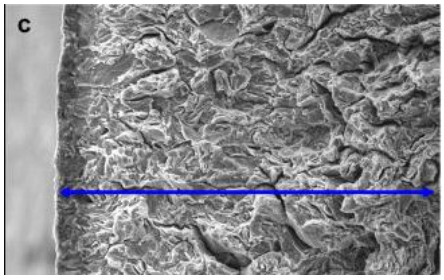

Figure 2.16. T91 Cracking from Hydrogen Embrittlement[77].

2.9. Challenges in the Use of Grade 91 Steel

Since heat treatment affects prior austenite grain size, martensite grain (lath) size, and precipitate concentration/size, research suggests that optimizing heat treatments for Grade 91 steels could improve their performance and creep strength, while poor heat treatments could cause premature failure. It is entirely plausible that AM Grade 91 and wrought Grade 91 steel might demand different heat treatments for the same applications. The second challenge to performance and lifetime is premature failure due to irradiation effects. Both of these challenges will be discussed in this subchapter.

The main difficulty with Grade 91 steel arises when more complicated structures than pipes and tubes need to built. While Grade 91 is generally stronger and less amenable to cold working than austenitic steels, welding is known to be a lifetime-decreasing procedure on components. This is generally due to "Type IV" cracking, which is a failure mode in which weakened microstructure in the heat affected zones causes stresses, creep and premature failure [82]. Evidence of this is clear when asessing the creep rupture lifetime of weldments vs base metals (Figure 2.18).

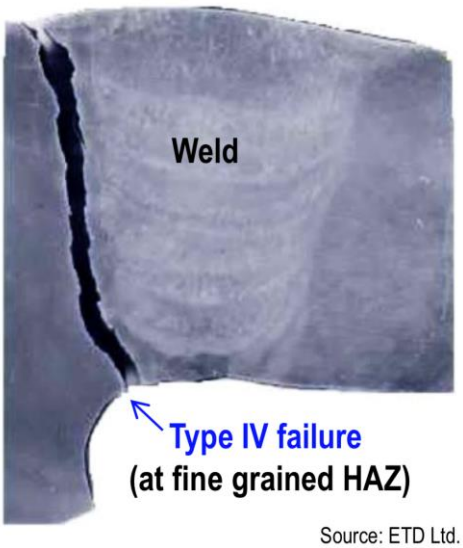

Figure 2.17. Weld showing failure at HAZ in Grade 91 steel[83].

Potential mitigation techniques have included various alterations of PWHTs, in

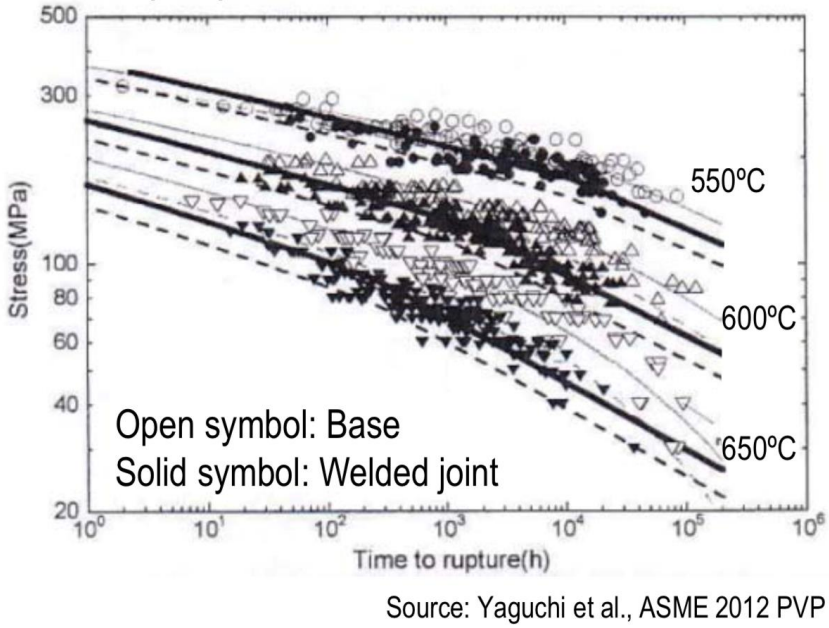

Figure 2.18. Creep-rupture lifetimes of base metal and weldment lifetimes, showing shorter lives of weldments[84].

attempts to re-temper the steel after welding. In doing so, some studies have demonstrated that lower temperature tempering (650 °C) prior to welding can result in more complete

dissolution of carbides during the weld, and improve the dispersion of carbide precipitates in the fine-grain HAZ, leading to higher strength and longer creep-rupture lifetime. It should be noted, however, that should AM fabrication be successfully carried out, entire parts could be printed as one component. Such components could, in theory have the same microstructural features as a base metal, and thus, could reduce or eliminate the need for post fabrication welding entirely.

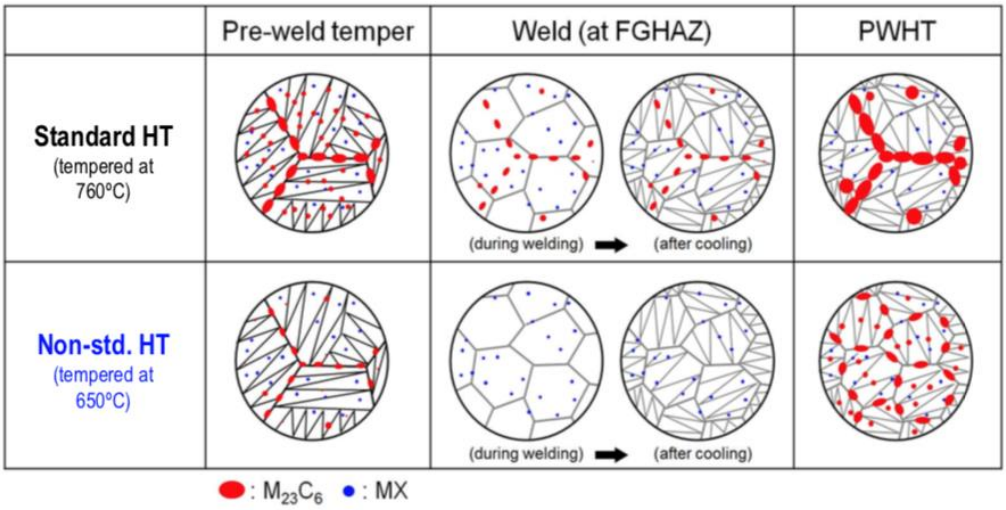

Figure 2.19. Dispersion effect of $M_{23}C_6$ carbides resulting from lower temperature tempering heat treatment[6].

3. Additive Manufacturing of Metal Components

The core principle of Additive Manufacturing is that virtually any computer aided design (CAD) drawing can be divided into finite 2-D elements, or slices, which are built, slice by slice, to form a 3-D component. AM can significantly reduce the production time for all but the most basic of shapes, and doesn't require additional iterative stages, adjustments, or craftsmanship. As complicated shapes and simple ones take about the same time to build, geometric complexity is essentially "free".

Though it has many advantages over traditional manufacturing, AM has some limitations that make it undesirable for a number of applications. Tailoring material properties can be a challenge, because heat isn't applied to the whole component at once, but rather localized, or in bursts. Other than specialized machines, AM units are usually bench top sized, and their build volumes are limited.

In addition to technical and process considerations, a clear route for ASME certification does not yet exist for the qualification of metals made by AM methods. Conventionally made metals and alloys take around 7-10 years to come to market, and even longer for advanced nuclear applications (both civilian and defense) [13]. Though there are efforts to accelerate certification through the use of modeling and simulation to assist in the understanding of AM phenomena [106], it is unclear whether broad guidelines will be issued for AM process certification, or whether certification would take place in a more piecemeal manner (e.g., a specific "part" could be certified for production on a specific machine).

In this investigation, the material under study was fabricated using Direct Metal Laser Sintering (DMLS), which is a form of powder bed AM. In Chapter 5, an additional

specimen of Grade 91 material made from powder feed AM was analyzed using X-ray diffraction. Powder based methods are most often used for metal based AM, and both powder bed, and powder feed are discussed in this chapter.

3.1. Powder Bed Additive Manufacturing

In powder bed AM of metals, thoroughly mixed metallic powder is placed in a build chamber, on a build plate, where the powder is bonded together using sintering or melting. This powder sintering process, known as Selective Laser Sintering (SLS) or Direct Metal Laser Sintering (DMLS), is done in an inerted atmosphere (N_2 or Ar) with a 200-400 W laser capable of moving directed towards the build plate to heat small volumes of material at a time to their sintering temperature, scanning across the X and Y axes of a surface,

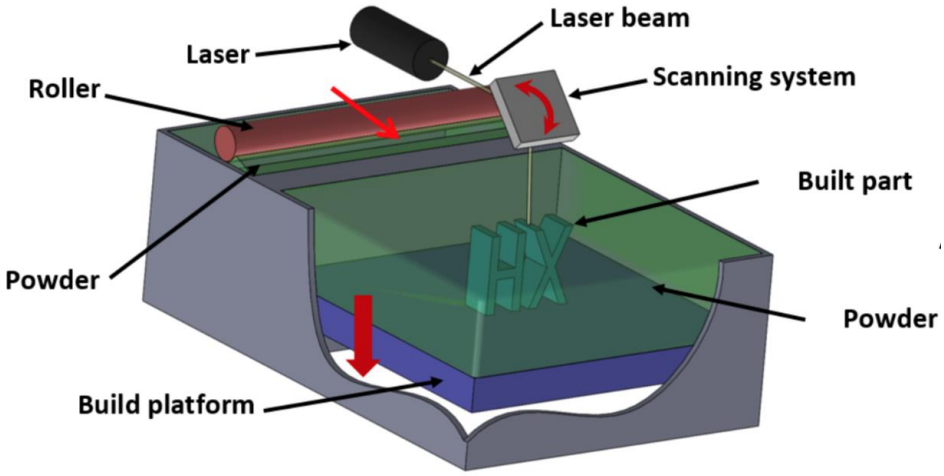

Figure 3.1. Illustration of a generic SLS/DMLS system[85] (used with permission)

completing a layer at a time [85]. After each layer is built, a piston moves the build plate down one later, and another moves the powder plate up one layer, and a roller or blade is used to redistribute the powder for the next layer. As a general benchmark, modern DMLS machines have dimensional accuracy up to +/= 0.25 mm, and can build in layers up to 0.1

mm thick [85]. DMLS has been shown to be compatible with a number of metals and alloys, most notably stainless steel, Al, Ti, Co, and some super-alloys like Inconel. Though DMLS can produce highly complex structures out of a wide variety of metallic powders, and does so with a high degree of accuracy (as compared to other powder based methods), there are potential drawbacks to using it. Potential issues include shrinking and warping due to high thermal distortion. And though the atmosphere is well controlled, even small impurities can cause build imperfections, and in most cases, post processing of surfaces is required to attain the desired finish.

Figure 3.2. An SLS/DMLS part made from alloyed Al[86].

There are additional powder bed methods that have achieved even higher accuracy than DMLS, most notably Selective Laser Melting (down to 30 μm layer thickness) [85]. These techniques were not investigated in this dissertation, but deserve further review as potential methods to fabricate FM steel in the future.

3.2. Powder Feed Additive Manufacturing

In powder feed AM, instead of material in a powder bed, powder is distributed to the melt location locally, where it is melted with a laser. This is known as Laser Metal Deposition (LMD). In this manner, new material is built on top of previous material (or a substrate) that has already solidified. Because of this, the substrate need not be made from the same material. So, powder feed AM can create differing layers of material with different powders, or even gradient mixtures of alloying elements in the same build by varying their concentration in the powder feed. Parts can thus be modified, or pieces can be replaced in this manner. The LENS specimen discussed in subchapter 5.1 was fabricated with an LMD type machine known as Laser Engineered Net Shaping (LENS) system.

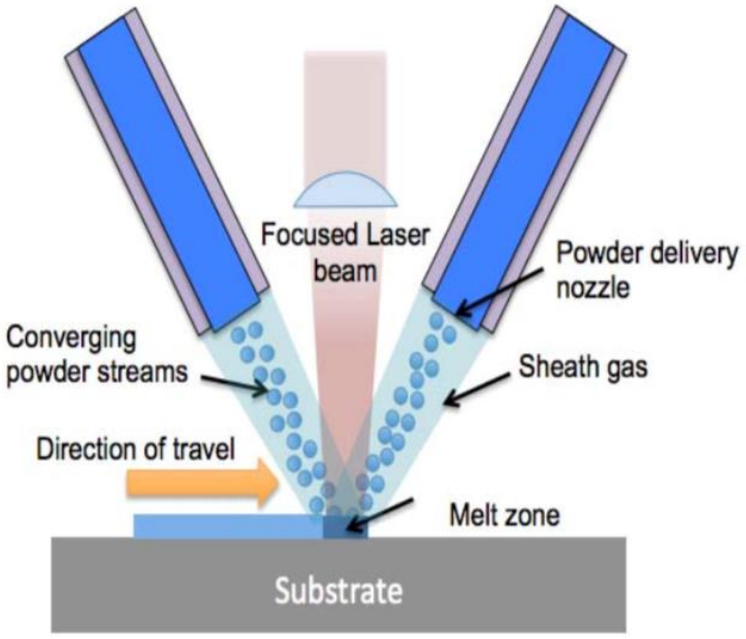

Figure 3.3. Illustration of LMD concept[85] (used with permission).

3.3. Quality and Characteristics of Metal Additive Manufacturing

The quality and properties of AM components are known to depend strongly on their processing technology. Because their microstructures depend on time-dependent phenomena, there are special considerations when considering metal AM. In DMLS systems like the one used in this investigation, laser passes can heat the target powder or already-built surfaces up to 105 °C per second [87], which can lead directly to:

- Hot cracking
- Species segregation
- Thermal residual stresses
- Suppressed phase transformations and super saturated phases

Alloys optimized for AM are generally those that already show good weldability, low heat-generated segregation, and low elemental losses. Some conventional alloys (like bronze) and exotic alloys (like high entropy alloys) are poorly suited for AM because their

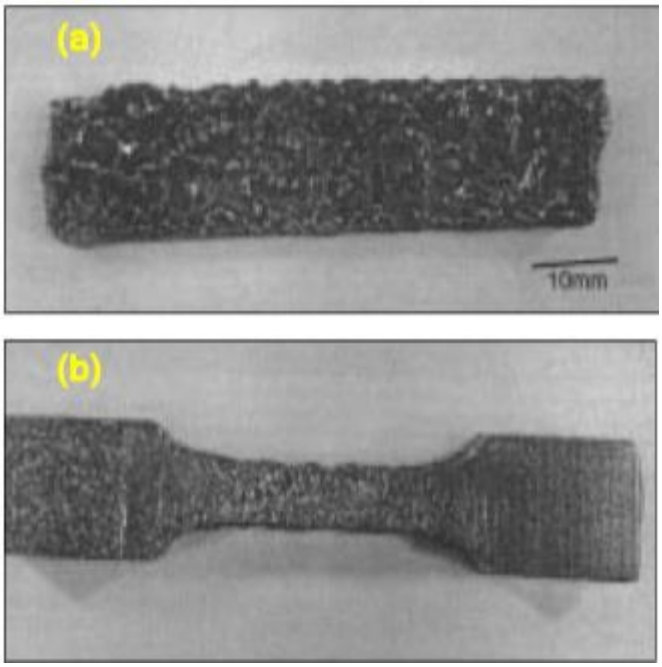

Figure 3.4. Poor surface finish (a), balling and warping (b) of 90Cu-10Sn produced by DMLS[88].

constituents' different physical properties (like melting temperature) induce unacceptable amounts of segregation. Early attempts (in the 1990's) to fabricate pre-alloyed bronze with DMLS resulted in poor quality surfaces and severe "balling" [88].

Control parameters can, to some degree adapt to necessary sintering or melting conditions, but only inasmuch as powder constituents' properties are compatible. For this reason, DMLS has had a number of spectacular failures in producing copper, lead, zinc, and tin alloys [88].

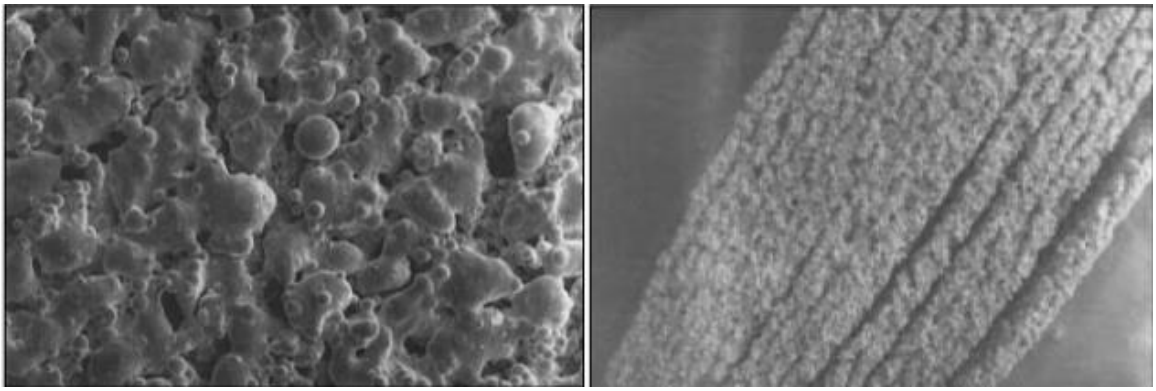

Figure 3.5. Bronze samples, showing balling due to poor atmospheric control, and poor interlayer bonding[88].

Finally, the control of solid-liquid ratio and melt viscosity are important in AM metal builds. For dense metal parts, best results have been obtained when using metal powder blends whose constituents' vary, as the partial liquid and solid phases during processes results in smooth and strongly sintered layers and minimum balling [88].

4. Methodology and Experimental Design

Using its constituent powders, the first known build of Grade 91 steel was carried out using DMLS at Los Alamos National Laboratory (LANL) as part of a Laboratory-Directed Research and Development (LDRD) initiative. Some of the material from this build was made available for this dissertation. As discussed Chapter 1, this investigation is a truly multidisciplinary study using a number of characterization and mechanical testing techniques to assess the suitability of AM Grade 91 steel as a potential advanced reactor core material. Inasmuch as this investigation explores new territory in the subject of Additive Manufacturing of high-alloyed steels, it offers an opportunity to inform a forward-looking strategy for moving forward with a licensing and/or code case assessment for AM in nuclear applications in general.

The evaluation of Grade 91 steel involves careful review of the DMLS fabrication parameters, followed by characterizing the newly fabricated material (both in terms of macroscopic properties and microstructure), performing mechanical (tensile) testing of specimens, providing additional microscopy of fracture surfaces, carrying out ion beam irradiations (up to 100 dpa), assessing the nano-hardness of irradiated samples, and finally, analyzing all data for comparison with base case, (wrought Grade 91) material. These tasks were broken up into several phases, which are enumerated below and discussed in the subsequent subchapters:

Phase I: Fabrication of Specimens

a) Obtain specimens of newly built AM Grade 91 material
b) Use Electrical Discharge Machining (EDM) to machine tensile samples to size for tensile, thermal, and irradiation specimens

Phase II: Heat Treatments of Specimens

a) Normalization and air quenching of some AM Specimens
b) Tempering of some AM specimens
c) Categorization and labelling of individual specimens according to heat treatments and fabrication type (AM vs wrought)

Phase III: Microscopy and Characterization

a) X-ray Diffraction (XRD), Electron Backscatter Diffusion (EBSD), Scanning Electron Microcopy (SEM) and other methods to describe microstructure
b) Thermal Diffusivity Measurement using Laser Flash Analysis (LFA)

Phase IV: Mechanical Testing of Grade 91 Specimens

a) Room Temperature Tensile Testing
b) 300 °C Tensile Testing
c) 600 °C Tensile Testing
d) Strain Rate Jump Testing
e) Microscopic Examination of Fracture Surfaces

Phase V: Radiation Damage Experiments

a) Simulation of displacement damage (dpa) using SRIM
b) Ion Beam Irradiation of AM and wrought steel specimens to 30 dpa
c) Irradiation of AM and wrought steel specimens to 100 dpa
d) Nanohardness testing of irradiated Samples

Phase VI: Results, Analyses, and Findings

4.1. Fabrication of Specimens

All AM specimens for tensile testing and irradiation were built using a single build procedure on the EOS M-280™ Direct Metal Laser Sintering (DMLS) system (Figure 4.1) owned and operated by Los Alamos National Laboratory (LANL). The M-280 is a powder bed type DMLS system capable of rapid prototyping of metals from fine powders using a fiber laser capable of laser powers up to 400 W.

Figure 4.1. EOS M-280 AM System installed at LANL[89]

The powder used for the AM build in this investigation was obtained from a commercial vendor. Its constituent makeup is given in Table 4.1.

Table 4.1. Chemical concentrations of pre-fabrication metallic powder (in percent).

C	**Mn**	**P**	**S**	**Si**	**Cr**	**Mo**	**Ni**
0.09	0.47	0.003	0.007	0.41	9.01	0.93	0.06
V	**Nb**	**B**	**N**	**Al**	**Ti**	**Zr**	**Fe**
0.18	0.07	<0.001	0.03	0.02	<0.01	0.01	rem

The concentration of each constituent was carefully controlled in order to produce powder for the DMLS system that was as close as possible to that described by the ASME code case (Table 4.2). Additionally, Laser Diffraction analysis was done to determine the mean particle size of the constituent powder (Figure 4.2).

Table 4.2. ASME (ASTM) A213 Standard Grade 91 Chemical Composition Ranges (in percent).

C	**Mn**	**P (max)**	**S (max)**	**Si**	**Cr**	**Mo**	**Ni(max)**
0.07-0.14	0.30-0.60	0.02	0.025	0.20-0.50	8.00-9.50	0.85-1.05	0.04
V	**Nb**	**B**	**N**	**Al (max)**	**Ti**	**Zr**	**Fe**
0.18-0.25	0.06-0.10	-	0.03-	0.02	-	-	rem

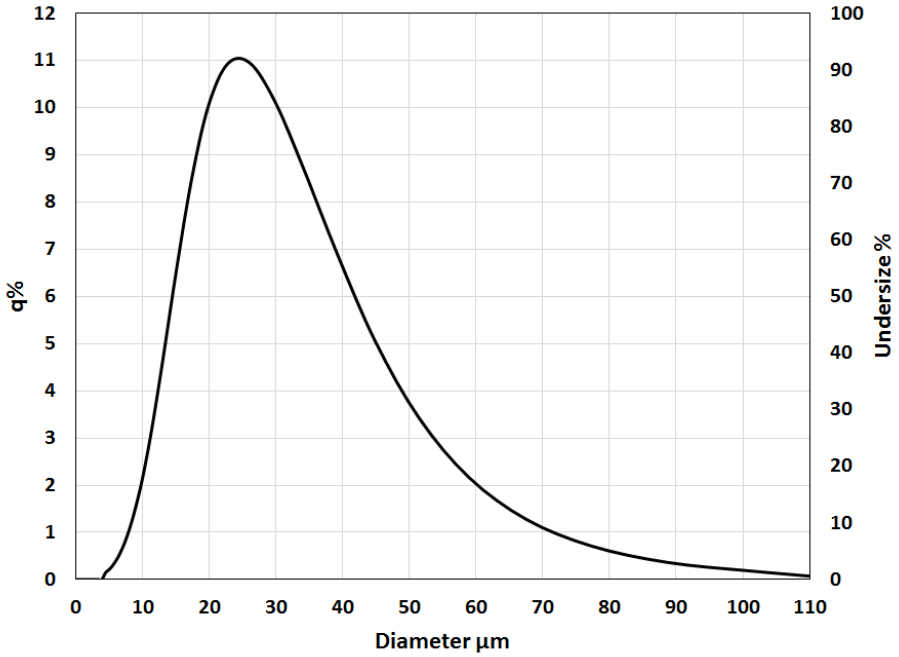

Figure 4.2. Laser diffraction analysis used to determine metallic powder size distribution[90].

Because of its presence in the precursor powder, nickel content in the AM Grade is slightly (0.02%) above the ASTM standard for wrought Grade 91 material. This small

difference is not expected to affect the thermomechanical properties of the material in this study. But, because nickel's high neutron absorption cross section, it will be both an activation hazard and burnable poison in reactors. For this reason, nuclear grade constituent AM powder would likely require powder with a lower nickel content.

The original intent of the AM build was to fabricate plates that could be machined into tensile, irradiation, and characterization specimens, as well as directly fabricated tensile specimens that could be tensile tested without additional machining. Additionally, a scaled section of a monolithic micro-reactor core design was included as a proof of principle. Due to an unanticipated collision between the wiper blade and a direct-fabrication tensile specimen, and the build was interrupted prematurely. Though the build was only about 75% complete, it did produce the plates, and enough material such that enough tensile, irradiation, and thermal specimens could be machined to carry out this investigation (Figure 4.3).

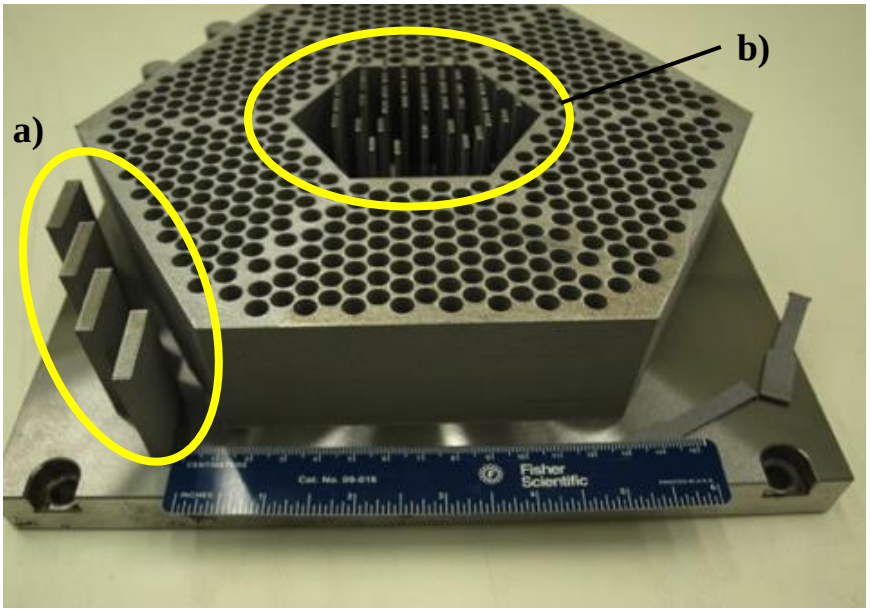

Figure 4.3. Photograph of the AM build, with plates for wedge-type specimens (a) and material for micro tensile specimens (b)

Though the interruption of the build precluded testing of direct-fabricated tensile specimens, between the incomplete tensile specimens and the plates, enough material was harvested to make micro-tensile tensile specimens with an onsite Electrical Discharge Machining (EDM) system.

4.1.1. Tensile Specimens

Tensile specimens were procured for both AM and wrought material. For all AM specimens in this investigation, material was machined in such a way that the testing axis was parallel to the build direction. Early testing has suggested that if AM specimens have not been properly laser sintered, they may be weaker in the build direction due a tendency for layers to delaminate [91]. Wrought material was procured in its cold-rolled state, and had not been exposed to post-fabrication heat treatments upon receipt. Two different sizes/shapes of tensile specimen were used in this investigation. Using EDM, a number of wedge shaped specimens were machined from both the AM plates and the wrought Grade 91 material. The gauge length of each specimen was around 13 mm, and the width and thickness 2-3 mm.

The unfinished direct fabrication tensile specimens were not of sufficient thickness to machine into wedge-type specimens. For this reason, they were instead machined into a smaller shape of tensile specimen, known as a micro-tensile sample. Each micro-tensile specimen had a gauge length around 5 mm, and its thickness and with were all between 1-2 mm.

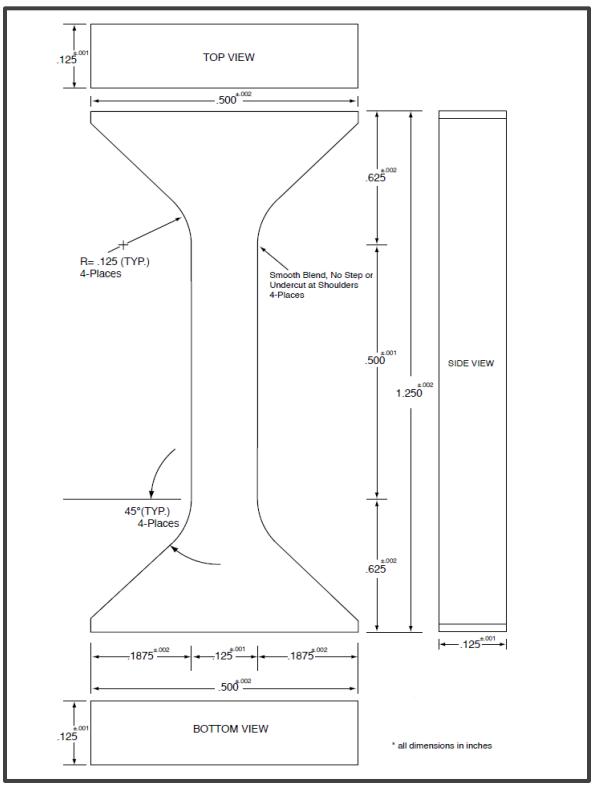

Figure 4.4. Wedge-type tensile specimen (dimensions shown in inches) [92].

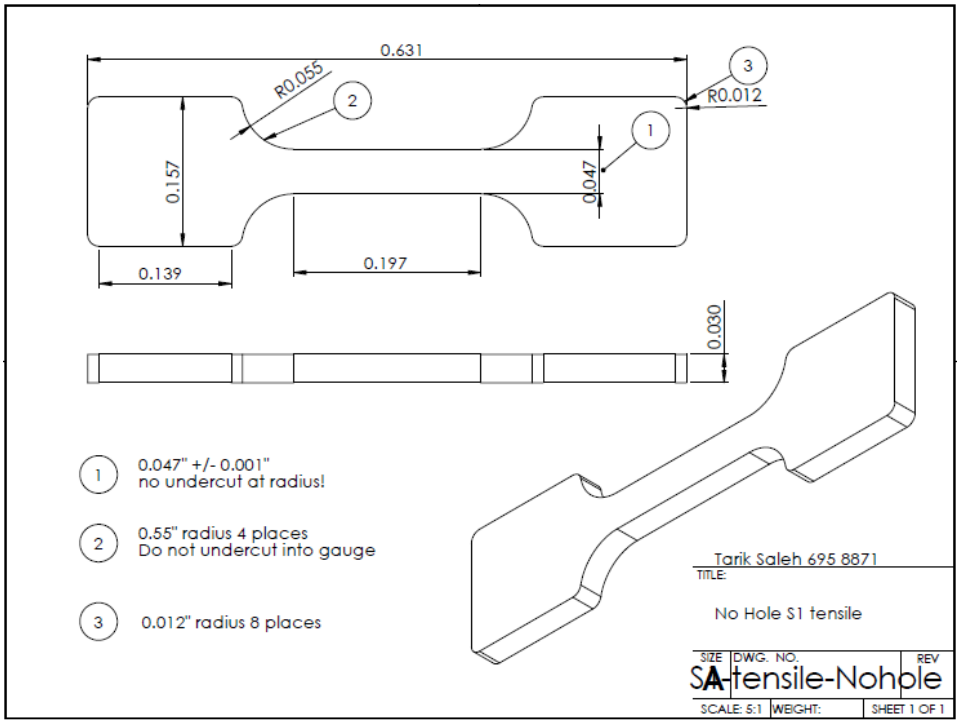

Figure 4.5. Micro-tensile specimen (dimensions shown in inches)[92]

In order to organize the samples, they were labeled by their fabrication type and intended heat treatments (Subchapter 4.2). Wrought specimens were given the prefix "WR" and AM specimens "AM". Normalized-only specimens were given the letter "N", normalized and tempered specimens were given the letters "NT", and direct tempered specimens (AM only) were given the letter "T". Wedge-type specimens were given numbers 1-2 and "S", and micro tensile specimens are numbers 3-6In this manner, each specimen was given a specimen ID so that it could identified by fabrication type and heat treatment. A summary of all machined tensile specimens is given in Table 4.3.

Specimen	Fabrication	Post-fab Heat Treatment	Test Temp	$\dot{\varepsilon}$ [s^{-1}]
WRN1	Wrought	Normalized	20º C	10^{-3}
WRN2	Wrought	Normalized	20º C	10^{-3}
WRNT1	Wrought	Normalized & Tempered	20º C	10^{-3}
WRNT2	Wrought	Normalized & Tempered	20º C	10^{-3}
AMAD1	DMLS	none (as-deposited)	20º C	10^{-3}
AMAD2	DMLS	none (as-deposited)	20º C	10^{-3}
AMN1	DMLS	Normalized	20º C	10^{-3}
AMN2	DMLS	Normalized	20º C	10^{-3}
AMT1	DMLS	Tempered (direct)	20º C	10^{-3}
AMT2	DMLS	Tempered (direct)	20º C	10^{-3}
AMNT1	DMLS	Normalized and Tempered	20º C	10^{-3}
AMNT2	DMLS	Normalized and Tempered	20º C	10^{-3}
AMNTt1	DMLS	Normalized and Tempered	20º C	10^{-3}
WRNT3	Wrought	Normalized and Tempered	300º C	10^{-3}
AMAD3	DMLS	none (as-deposited)	300º C	10^{-3}
AMNT3	DMLS	Normalized and Tempered	300º C	10^{-3}
WRNT5	Wrought	Normalized and Tempered	600º C	10^{-3}
AMAD5	DMLS	none (as-deposited)	600º C	10^{-3}
AMAD6	DMLS	none (as-deposited)	600º C	10^{-3}
AMNT5	DMLS	Normalized and Tempered	600º C	10^{-3}
AMNTf6	DMLS	Normalized and Tempered	600º C	10^{-1}
WRNT-S	Wrought	Normalized and Tempered	600º C	variable
AMNT-S	DMLS	Normalized and Tempered	600º C	variable

Table 4.3. Tensile specimens by fabrication type, heat treatment, test temperature, and strain rate.

4.1.2. Thin Disk Samples for Irradiation

Thin samples for ion beam irradiation were prepared to specifications using established machining and metal polishing techniques. EDM machining was used to produce 2 AM normalized and tempered (AMNT) disks and 2 WR normalized and tempered (WRNT) measuring 3 mm in diameter, and between 0.5 and 1 mm thick. For irradiation and nanoindentation testing, the surfaces should be polished to as smooth a finish as possible. This was achieved in the following procedure:

Figure 4.6. Thin disk sample mounted to polisher head

i) Samples were mounted to the polisher head using a temperature activated adhesive.

ii) Samples were ground down with 800 and 1200 grit SiC sandpaper (at 200 rpm) for several minutes at a time

Figure 4.7. Grinding/polishing of thin disks in preparation for irradiation.

.

iii) Samples were each polished with 4000 grit SiC sandpaper to a mirror finish and prepared for electro-polishing

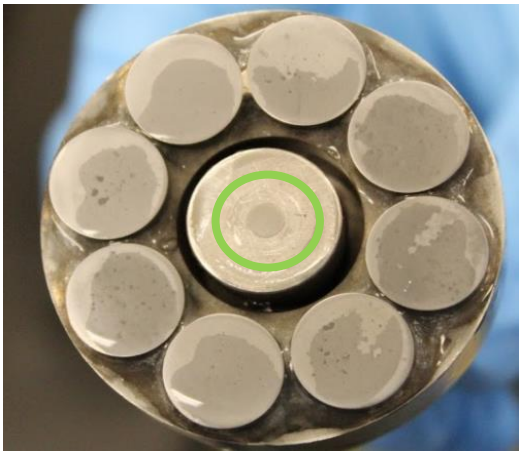

Figure 4,8 Polished thin disk sample

iv) Samples were electropolished to Transmission Edge Microscopy (TEM) surface finish standards.

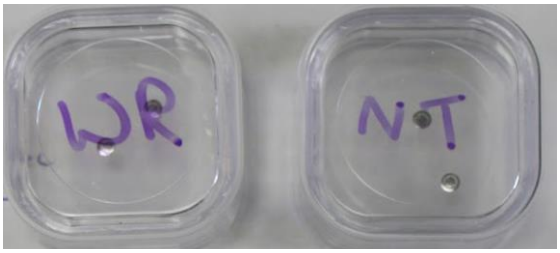

Figure . 4.9 Final electropolished finish

4.1.3. Disk Samples for Laser Flash Analysis

For Laser Flash Analysis (LFA), specimens of As-deposited (AMAD), AM normalized and tempered (AMNT), and wrought normalized and tempered (WRNT) were machined using EDM to the specifications given by the on site Netzsch 457 Microflash™ system [93]. The standard size of all samples was 1 cm diameter by 1-3 mm thickness.

4.2. Normalizing, Quenching, and Tempering Heat Treatments

ASME standard heat treatments for Grade 91 steel (SA213, SA335, SA387) include normalization at 1040 – 1080 °C, tempering at 730-800 °C, and post weld heat treatments (PWHT) at 730 – 775 °C [37]. Optimization of heat treatments (including PWHT) is an ongoing subject area, and while micro alloying, precipitation, and other phenomena are directly affected by heat treatment procedures, for this investigation a standard ASME heat treatment was chosen so that the microstructure and heat treatment responses could be compared directly between AM and wrought Grade 91 material.

Throughout this investigation, all normalized material was heated in a furnace to 1040 °C for 30 minutes and allowed to cool (quench) to room temperature in air. All tempered material was heated to 760 °C for 45 minutes, and allowed to cool to room temperature in air.

Because this investigation was primarily to compare AM and wrought Grade 91 material, the heat treatments were kept constant throughout the experiment. In future work, AM-specific optimizations should carried out as part of a path forward for qualifying AM Grade 91 steel for commercial use.

4.2.1. Normalization and Quenching

Metallurgically, normalization is a standardized practice of increasing the temperature of a metal or alloy to a specified temperature to increase its microstructural uniformity. $M_{23}C_6$ type carbides, which make up the majority of precipitates in Grade 91 steel, become soluble around 870 ºC, while the MC type carbides become soluble at 900 C. The small amount of nitrides present do not dissolve until around 1000 °C, but they are very important in inhibiting grain growth during normalization temperatures [94]. Normalizing temperature is chosen to be above the temperature required to dissolve precipitates and homogenize the microstructure, but not so hot that it causes unwanted grain coarsening/growth. For FM steels, these temperatures are roughly 1000 °C – 1100 °C, and for Grade 91 steel, this range is refined further by ASME standards to be 1040 – 1080 °C [37].

Quenching is the cooling of a material after a heat treatment, and can either be done in air, water, oil, or other effective heat transfer fluids. For practical and cost reasons, air quenching is used in large batch commercial FM steel fabrication. Air quenching from the normalization temperature to room temperature has been proven to produce sufficiently rapid cooling rates for the critical martensite transformation to take place.

4.2.2. Tempering

Tempering is a heat treatment that reduces the hardness of metals and alloys by heating to a temperature sufficient to relieve internal stresses. The amount of hardness removed is proportional to the tempering temperature. For FM (and other carbon steels) normalizing and quenching are usually done in sequence. Normalization strengthens the steel, and

tempering counteracts the resulting decrease in ductility to produce a strong, tough, and workable material.

4.3. Microscopy Methodology

An array of microcopy and characterization techniques at several institutions were utilized in this investigation to analyze AM material prior to and after various heat treatments and testing. The X-ray Crystallographic Center at the University of Maryland was utilized to perform X-ray Diffraction analysis on tensile samples, Los Alamos National Laboratory (LANL)'s Materials Science Laboratory was used for Electron Backscatter Detection (EBSD)/Scanning Electron Microscopy (SEM), and Optical microscopy (including etching). Additionally, a number of AM and wrought specimens were send to the National Synchrotron Light Source-II (NSLS-II) facility at Brookhaven National Laboratory for additional high-energy XRD analysis [95].

4.3.1. SEM and Electron Backscatter Diffraction and

EBSD is typically carried out within in a SEM system in which an EBSD camera is positioned in such a way as to exploit the constructive interference of interrogation electrons that meet the Bragg condition of the lattice being interrogated [96]. Used in other diffraction techniques (including x-ray and neutron diffraction), the Bragg condition occurs when particles/waves of sufficiently small wavelength scatter off lattice atoms at discrete angles related to their interatomic spacing, such that they cause constructive interference, and an increase in wave amplitude. The condition is given by Bragg's law, and is illustrated in Figure 4.10.

$$2d\sin(\theta) = n\lambda \qquad \text{(Bragg's Law)}$$

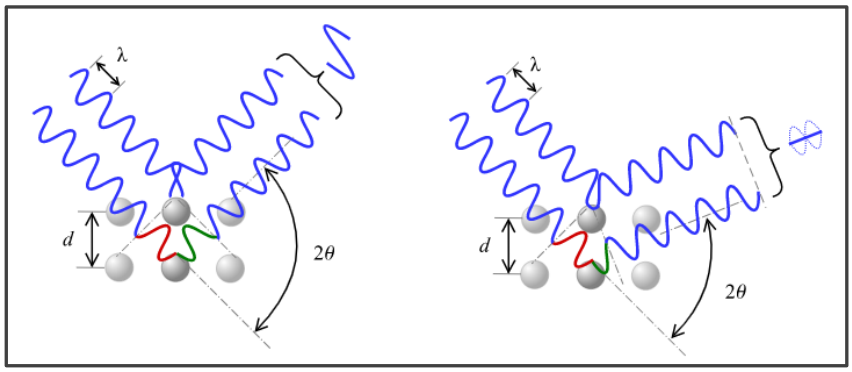

Figure 4.10. Illustration of Bragg condition (a), and destructive interference (b)[97].

Electrons backscattering through the Bragg condition then hit a phosphor screen, which fluoresces, and the resulting photons are collected. A diffraction patter is generated, and in this way a characterized crystal's direction and phase can be determined.

EBSD images were generated with the commercially available SEM/EBSD system on site at LANL for the AM as-deposited and normalized/tempered (AMAD and AMNT) to determine their microstructural features.

4.3.2. X-ray Diffraction Analysis

X-Ray Diffraction (XRD) was initially performed on a total of 8 different specimens to determine crystallographic features, specifically transformations in steel phases, carbides/precipitate concentrations, internal stresses and lattice parameters. XRD is a common characterization technique that utilizes monochromatic x-rays to interrogate the crystal structure (and thereby the lattice parameter) by means of diffraction. Like EBSD, XRD relies on waves scattering through the Bragg condition [93]. Unlike like

EBSD, the constructively scattered waves are x-rays (photons) and can enter the detector directly, and register as counts (with an associated angle) directly.

One-dimensional diffraction data sets consist of the incident/observed angle (2θ from the Bragg condition), and a number of counts for that channel. Based on crystallographic data libraries, species/phases are identified by lattice parameter (d in the Bragg condition) and locations (and relative intensities) of the diffraction peaks. and algorithms incorporating Rietveld Analysis techniques in the TOPAS™ software package (Brucker, Inc) [100].

The National Synchrotron Light Source-II (NSLS-II) facility at Brookhaven National Laboratory houses the X-Ray Powder Diffraction (XPD) beamline, which serves as user facility capable of performing high-intensity XRD analysis on solid samples. By using a sophisticated synchrotron source, XPD has a flux capability of 6×10^{13} photons/s and fully tunable energy range from 40 – 70 keV. This is considered a high-energy X-ray capability, which allows for more fine discrimination of interactomic spacing (lattice parameter), since smaller differences in lattice parameter can be observed with shorter wavelength (higher energy) x-rays. For this part of the investigation, the incident X-ray energy was tuned to 66.415 keV, corresponding to a wavelength of 0.18668 Å (0.018668 nm).

Of the 8 specimens analyzed with the XPD beamline, 4 were from the AM DMLS build used in this dissertation (AMN, AMT, and AMNT), two were from a similar build on the same machine of Grade 91 material from a related project (AMAD*, AMNT*), one was from a LENS AM machine build with the same powder precursor, and one was wrought normalized and tempered material.

Specimen	Fabrication	Post-fab Heat Treatment
AMN	DMLS (AM)	Normalized
AMAD	DMLS (AM)	none
LENS	LENS (AM)	none
AMAD*	DMLS (AM)	none
AMNT*	DMLS (AM)	Normalized & Tempered
AMT	DMLS (AM)	Direct Tempered
AMNT	DMLS (AM)	Normalized & Tempered
WRNT	Wrought	Normalized & Tempered

Table 4.4. Specimens analyzed in XPD beam, by fabrication type and heat treatment.

Additional XRD measurements were performed at UMD's X-Ray Crystallographic center on two fractured tensile specimens after they were shown to have exhibited extraordinary strength at 300 °C and 600 °C during testing. The purpose of the additional XRD at UMD was to determine the relative portions off FCC (austenite) and $M_{23}C_6$ phases in the specimen. All XRD analyses were carried out successfully, and their results are discussed in Subchapter 5.2.

4.4. Mechanical Testing of Unirradiated Steel Specimens

4.4.1. Tensile Testing Preparation

Uniaxial tensile testing is a well-established process used to determining the stress-strain behavior of materials under controlled tension loads. For this investigation, an MTS Model 880 Uniaxial Load Frame located in the Materials Science Laboratory at Los Alamos National Laboratory was used [101].

In preparation for testing, each tensile specimen was measured using a CCTV microscope and micrometer setup (Figure 4.11). The gauge length was measured, along with the width in three locations (top, center and bottom), and thickness (top, center and bottom). The orientation and measurements of each tensile sample were recorded, so that the thickness and width at the point closest to the fracture could be used in computing stress and strain during analysis of tensile data.

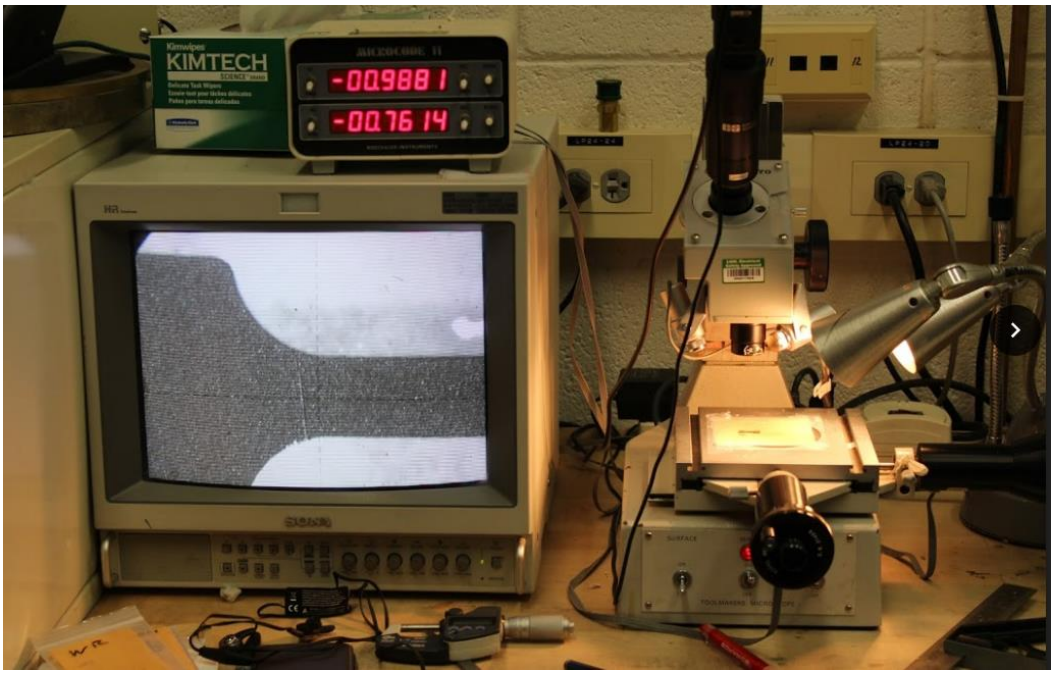

Figure 4.11. Tensile specimen measurement station at LANL.

4.4.2. Tenstile Testing Setup

Room temperature tensile tests were carried out in air, using the load cell, grips, and extensometer shown in Figure 4.12.

Figure 4.12. Room Temperature tensile specimen setup, showing load cell, grips and extensometer.

For 300 °C tensile tests, an MTS 651 Environmental Chamber (furnace) was added to the system, along with a thermocouple for monitoring temperature. In the 300 °C tests, displacement data was recorded directly from the load cell (as opposed to the mounted extensometer), as shown in Figure 4.13.

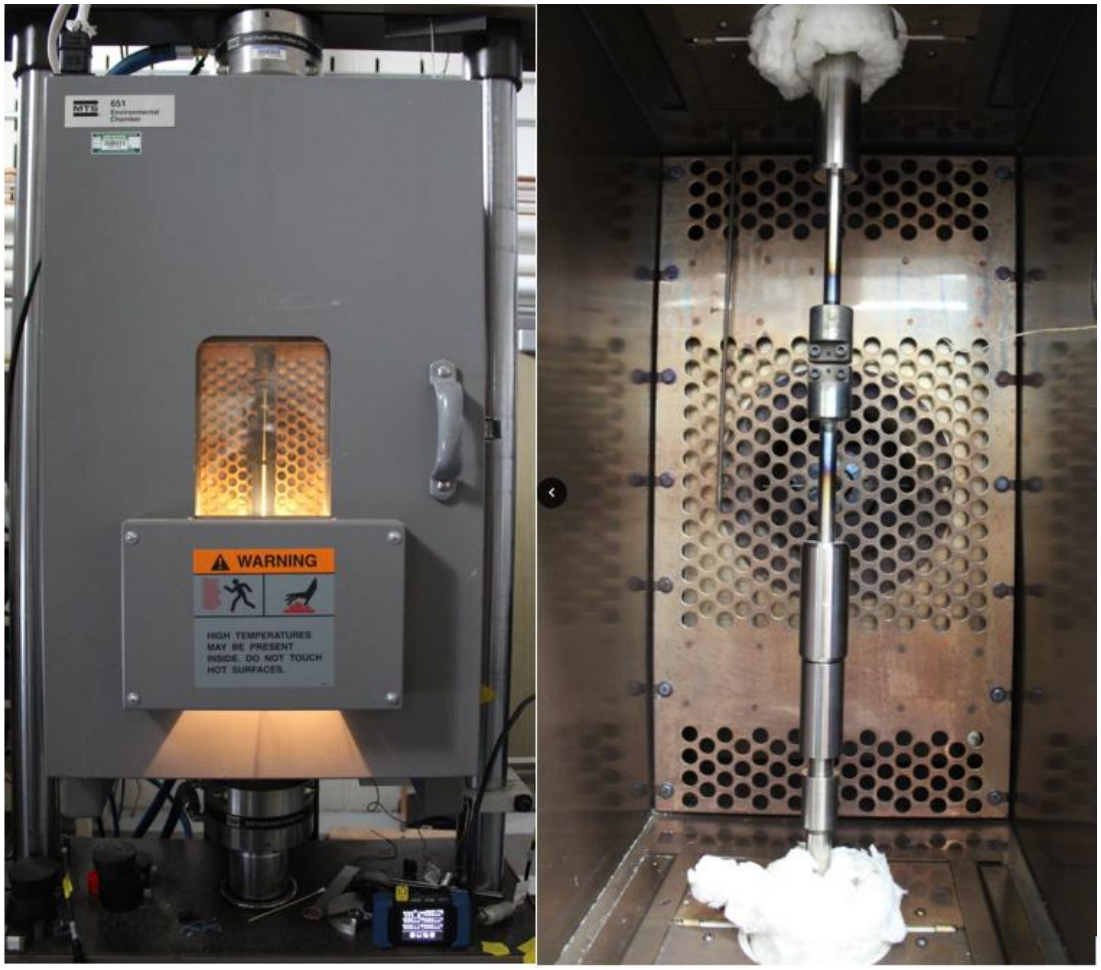

Figure 4.13. 300 °C testing setup, with grips and specimen inside environmental chamber

For 600 °C tests, a sealed vacuum chamber was used, to prevent excessive oxidation of the specimen surfaces (Figures 4.14-15.). In all elevated temperature tests, the chamber was heated and held at testing temperature for 30 – 45 minutes to ensure thermal equilibrium.

Figure 4.14. Outside view of vacuum chamber, furnace, and load frame for 600 °C testing setup

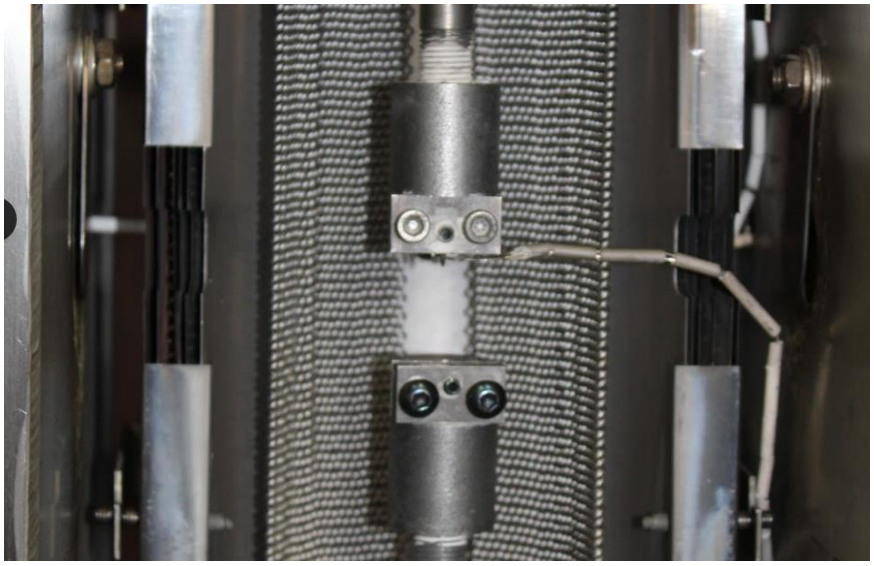

Figure 4.15. Inside of vacuum chamber used in 600 °C testing.

Each test generated a data file with a unique name corresponding to the sample ID, testing temperature, and strain rate. Table 4.1, reprinted here, provides a summary of the specimens tested in this investigation, including their testing temperatures and strain rates.

Specimen	Fabrication	Post-fab Heat Treatment	Test Temp	$\dot{\varepsilon}$ [s^{-1}]
WRN1	Wrought	Normalized	20º C	10^{-3}
WRN2	Wrought	Normalized	20º C	10^{-3}
WRNT1	Wrought	Normalized & Tempered	20º C	10^{-3}
WRNT2	Wrought	Normalized & Tempered	20º C	10^{-3}
AMAD1	DMLS	none (as-deposited)	20º C	10^{-3}
AMAD2	DMLS	none (as-deposited)	20º C	10^{-3}
AMN1	DMLS	Normalized	20º C	10^{-3}
AMN2	DMLS	Normalized	20º C	10^{-3}
AMT1	DMLS	Tempered (direct)	20º C	10^{-3}
AMT2	DMLS	Tempered (direct)	20º C	10^{-3}
AMNT1	DMLS	Normalized and Tempered	20º C	10^{-3}
AMNT2	DMLS	Normalized and Tempered	20º C	10^{-3}
AMNTt1	DMLS	Normalized and Tempered	20º C	10^{-3}
WRNT3	Wrought	Normalized and Tempered	300º C	10^{-3}
AMAD3	DMLS	none (as-deposited)	300º C	10^{-3}
AMNT3	DMLS	Normalized and Tempered	300º C	10^{-3}
WRNT5	Wrought	Normalized and Tempered	600º C	10^{-3}
AMAD5	DMLS	none (as-deposited)	600º C	10^{-3}
AMAD6	DMLS	none (as-deposited)	600º C	10^{-3}
AMNT5	DMLS	Normalized and Tempered	600º C	10^{-3}
AMNTf6	DMLS	Normalized and Tempered	600º C	10^{-1}
WRNT-S	Wrought	Normalized and Tempered	600º C	variable
AMNT-S	DMLS	Normalized and Tempered	600º C	variable

Table 4.1. Tensile specimens by fabrication type, heat treatment, test temperature, and strain rate.

4.5. Measuring and Interpreting Stress and Strain in Steels

Engineering stress-strain relationships are generated by measuring the tensile force applied and resulting strain induced within the control volume of the specimen. Engineering stress is then calculated by dividing the specimen's cross sectional area by the applied force, and the engineering strain is calculated as the displacement measured divided by the original sample length. Using strain as the abscissa and stress as the ordinate, a standard stress-strain curve is generated.

For most metals and alloys, as tension load is applied, the specimen stretches elastically until it reaches its yield strength (YS), plastically deforms as it strengthens to its ultimate tensile strength (UTS), begins necking and non-uniform deformation, and eventually fractures. These behaviors under tension are divided into distinct regions along the strain axis, as represented in Figure 4.16.

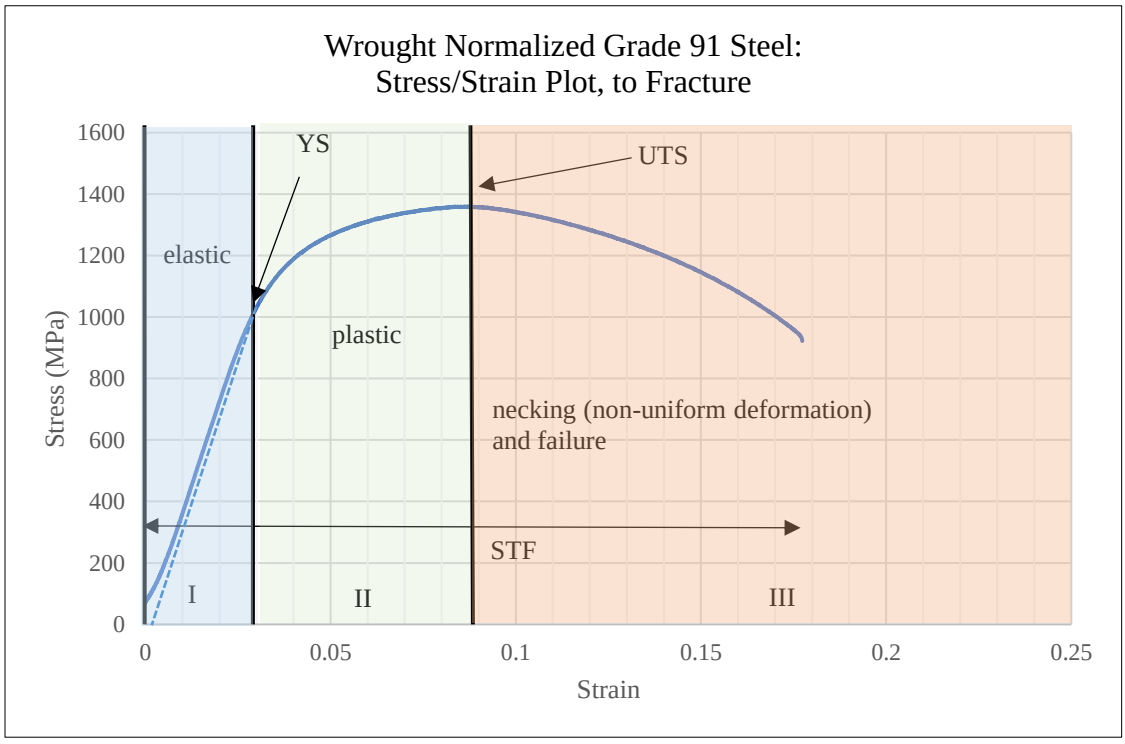

Figure 4.16. Typical Measured Stress-Strain for Normalized FM Steel

4.5.1. Elastic Strain Region

For most materials, the elastic strain region, often called the linear elastic region, represents the domain where strain is directly proportional to stress. Phenomenologically, this linear elastic response is the result of the stretching of interatomic bonds, continuously interaction through electrostatic attraction and repulsion. Much like an ideal spring, this region behaves according to Hooke's Law:

$$\sigma = E\varepsilon \qquad \textbf{Equation 4.1}$$

The proportionality constant, E, is called the Elastic Modulus (sometimes called Young's Modulus), and is an intrinsic property of the material that describes the resistance to deformation from an applied stress. It can also be thought of as the slope of the stress-strain curve within the elastic region (Region I in Figure 4.16). It is important to note that in practice, tensile testing does not usually provide an accurate measure of *E*, because in the elastic region, miniscule strain in the testing apparatus system tends to compound, which makes it difficult to isolate the strain in the specimen from the total displacement recorded by the extensometer. However, evaluating the slope of this linear elastic region is useful for determining when a specimen has reached its elastic limit and begun to plastically deform, and by extension, can be used to determine YS.

4.5.2. Plastic Deformation Region

As stress is increased up to the maximum in its elastic region, a material approaches the upper limit of its proportionality (elastic) region, and eventually reaches its Yield Strength (YS), which is the stress at which the material begins to plastically and permanently deform. In high-strength steels (including FM steels), the true yield point is

difficult to determine [27]. Because of this difficulty, Yield Strength is usually taken to mean the Offset Stress (also known as the Proof Stress), which is defined as the stress value at which the specimen experienced 0.2% plastic strain. That convention is used throughout this investigation as the definition of Yield Stress and was determined in the following way:

- Plot the stress-strain curve
- Calculate the slope of the linear elastic region $(\Delta\sigma/\Delta\varepsilon)$
- Create the 0.2% Offset line with the same slope as the linear elastic region, originating at 0.2% strain and 0 MPa stress (0.002,0)
- Record the stress value where this 0.2% offset line intersects the stress-strain curve (labeled YS in Figure 4.17).

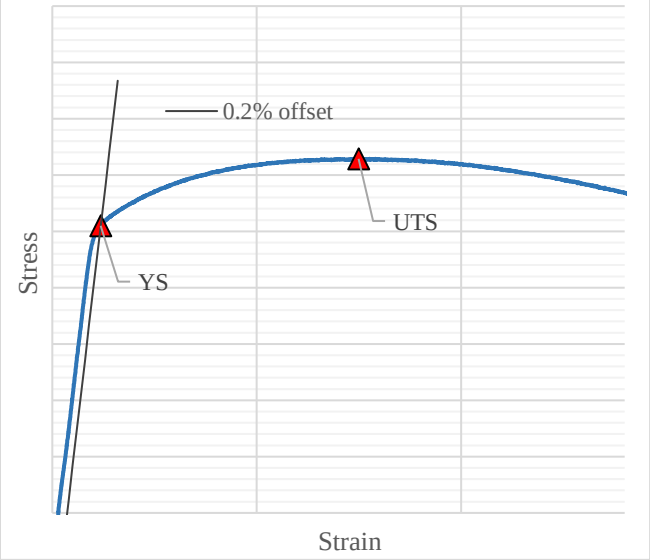

Figure 4.17. Illustration of the 0.2% Offset line, YS and UTS points.

Beyond the yield strength, the material will continue to plastically deform (Region II in Figure 4.16) until it reaches a maximum point, known as its Ultimate Tensile Strength (UTS). This plastic deformation, known as Uniform Elongation (UE) described the domain of the strain hardening region. In general, plastic deformation of engineering and structural materials is undesirable, as it causes geometrical

changes, possibly introducing complex stress states and failure. In nuclear applications, especially fast spectrum systems, small geometrical changes can cause profound changes in reactor physics calculations, due to neutron transport phenomena at small scales. The plastic deformation region (Region II in Figure 4.16), however is extremely important for safety margin and design purposes, because it represents the material behavior in transient conditions (acute high stress, or impact, for example), or long-term deformation phenomena such as creep. In this region, ductile materials (including steels) exhibit behavior known as strain hardening (or work hardening), in which additional stress and deformation increases the strength of the material, until it reaches its UTS. YS and UTS values are practical engineering scalar quantities and are used in this investigation to describe the strength of materials.

In addition to strength alone, the material's strain hardening behavior is important in determining its performance. In the strain hardening region, phenomena that cause permanent deformation, such as grain-boundary slip, dislocation glide, and dislocation climb (Region II), are described by an exponential function (Power Law):

$$\sigma = K\varepsilon^{n} \qquad \textbf{Equation 4.2}$$

Where *K* is a proportionality constant (in units of stress) and *n* is the strain hardening exponent computed from empirical data.

This investigation used empirical fits to generate, for the first time, the proportionality constant and strain hardening exponents (*K* and *n*) for AM Grade 91 steel. This relationship provides the basis for application-based and sophisticated descriptions of plastic deformation behavior. The domain of this region relates to materials' ductility, as the metal continues to strengthen, while the range describes the magnitude of the strain

hardening over that strain range. By describing the strain hardening of each specimen in terms of *K* and *n*, a quantitative comparison of strain hardening is achieved.

In addition to YS, UTS, and strain hardening parameters it is useful to describe a specimen's overall ductility. As measure of the strain over the course of an entire tensile test, the parameter total elongation (TE) is used. TE should be thought of as an extensive property, specific to the specimen being tested because non-uniform elongation (necking) past the UTS point results in a complex strain state of localized strain concentration and cavitation. For this study, the TE is defined as the total strain (elongation) at which the sample catastrophically fractures, encompassing all three regions in Figure 4.16. In this dissertation, TE is expressed in percent elongation.

In an engineering sense, YS and UTS are used to describe strength and TE to describe ductility. These are engineering properties, and thus calculated from the engineering stress and strain. For additional strain hardening analysis, the Power Law equations (functions of *K* and *n*) were generated to describe the strain hardening behavior in terms of true stress and strain. In addition to describing the strain hardening regions as functions, they are also described in term of toughness. While toughness can be used in more than one context (i.e, fracture toughness or notch toughness), in this investigation, the general definition of toughness will be used. Toughness can be defined as the capacity to absorb energy and resist failure. It's dimansions are usually given in units of energy per unit volume (KJ/kg^3)/ Mathematically, it is represented as the strain-integrated function of a given portion of the stress-strain curve:

$$\frac{Energy}{Volume} = U = \int_0^{\varepsilon} \sigma \, d\varepsilon$$

Equation 4.3

In a material's linear elastic region, this toughness function is known as resilience, and describes its capacity to absorb energy (per unit volume) elastically, and then return to its original form. The resilience function can thus be expressed as the integral of the elastic deformation function:

$$U_r = \int_0^{\varepsilon_{YS}} \sigma \, d\varepsilon$$

$$\sigma = E\varepsilon, \quad \varepsilon = \frac{\sigma}{E}, d\varepsilon = \frac{d\sigma}{E}$$

Substituting $d\varepsilon$:

$$U_r = \int_0^{\varepsilon_{YS}} \frac{\sigma d\sigma}{E}$$

$$U_r = \int_0^{\sigma_{YS}} \frac{\sigma d\sigma}{E} = \frac{\sigma^2}{2E}\Big|_0^{\sigma_{YS}} = \frac{{\sigma_{YS}}^2}{2E}$$

Equation 4.4

As previously mentioned, the behavior in the strain hardening region is also extremely important from the standpoint of safety margins, transient reactor effects, off-normal stresses, and long-term material stability (creep strength), and is described both by strengthening magnitude and ductility properties. In order to quantify and compare the toughness of the material in the strain hardening region, this investigation introduces the Strain Hardening Toughness (U_{SH}) to described as the integral of the strain hardening function, defined between the true YS and UTS as described on the true stress-strain curve such that:

$$U_{SH} = \int_{\varepsilon_{YS}}^{\varepsilon_{UTS}} \sigma \, d\varepsilon = \int_{\varepsilon_{YS}}^{\varepsilon_{UTS}} K \, \varepsilon^n d\varepsilon = \frac{K\varepsilon^{n+1}}{n+1}\Bigg|_{\varepsilon_{YS}}^{\varepsilon_{UTS}}$$

or in simplified form:

$$U_{SH} = K\left(\frac{{\varepsilon_{UTS}}^{n+1} - {\varepsilon_{YS}}^{n+1}}{n+1}\right)$$

Equation 4.5

It should be noted that because of non-uniform elongation (necking and cavitation) beyond the UTS point, the power law is not valid beyond the (true) UTS, and the strain function cannot be readily determined over the specimen's gauge length. In application, a sustained stress equal to the UTS would necessarily lead to failure, and thus should always be avoided. Nonetheless quantifying the strain hardening behavior is useful in determining performance and safety margins, and in comparing steel specimens to one another.

4.5.3. Compliance Correction Approach for Tensile Testing

In practice, a tensile specimen cannot be loaded into a testing rack such that it maintains perfect contact with the gripping surface while under a zero load. Similarly, the load required to achieve perfect contact will necessarily introduce strain into the specimen. As a sample is gripped and a load applied, there will be some movement, adjustment, or "seating" of a specimen within the testing apparatus's gripping mechanism, as well as

additional play at the points on contact and in the joints of the testing apparatus. This movement/adjustment of the sample, known as contact compliance, will cause the extensometer to overestimate the strain imposed in the specimen by the specified load. This erroneous measurement of strain (elongation) will in turn cause an underestimation in the stress required to elastically deform the specimen. This is part of the reason simply measuring the slope of the line on a stress-strain plot for metals is not an effective way to measure the Elastic Modulus in practice.

As the grips initiate contact with the specimen, the high compliance region of the stress strain curve is evident as a nonlinear curvature (highlighted in Figure 4.18). This curve can either be positive or negative, and represents the compliance region as the specimen moves into a more stable position under load. Though this region registers displacement

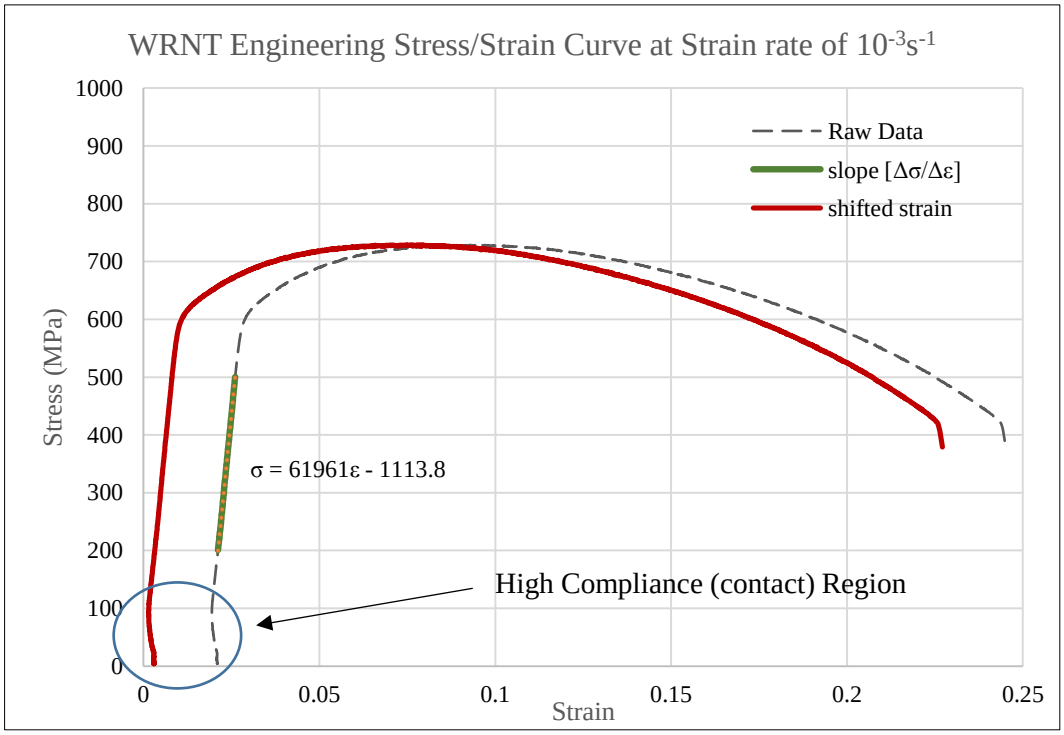

Figure 4.18. Shifted stress-strain curve showing contact region.

from the extensometer, the reading isn't a proper measure of strain because the

displacement is occurring within the system, rather than by elongation of the specimen itself. As the load is applied and the strain begins to register beyond this compliance region, the expected linear elastic response becomes apparent. Once this linear response is observed, the slope of the elastic region is computed with a linear fit.

An additional goal of compliance correction is to shift the stress-strain curve in such a way that the linear elastic region begins at the origin of the plot (0,0). To determine the adjustment required to shift the curve to the origin, the y-intercept (b) of the generalized $y = mx+b$ linear function is used to determine the x-intercept, such that:

$$y = mx + b,$$

$$0 = mx + b,$$

$$x = \frac{b}{m}$$

This x-intercept represents the shift in strain that is subtracted from all strain values to correct for the high compliance region. The new "shifted" stress-strain curve (Figure 4.18), in red) is now generated to represent the compliance-shifted engineering stress-strain curve. This shifting correction technique is used throughout the investigation, and all subsequent stress-strain relationships presented will be expresses as compliance-shifted curves.

4.5.4. Determining True Stress and Strain

Understanding the engineering stress and strain is useful in determining mechanical data for materials databases. Yield Strength and Ultimate tensile strength (UTS), for example, are engineering quantities computed from the engineering stress. However, because engineering stress is defined as the force per unit area on the initial cross sectional

area of the specimen, A_o, it does not account for the fact the true cross sectional area of the specimen is decreasing as a function of the strain. For this reason, a more phenomenologically accurate model of stress and strain, known as true stress and true strain, are often used for understanding and predicting the behavior of the material. The true stress is thus defined as the load divided by the instantaneous cross sectional area:

$$\sigma_T = \frac{F}{A_i} \qquad \textbf{Equation 4.6}$$

Assuming the specimen experiences no change in volume, instantaneous volume is equal to initial volume, such that:

$$A_i l_i = A_o l_o$$

$$A_i = \frac{A_o l_o}{l_i}$$

Substituting into Equation 4.6,

$$\sigma_T = \frac{F * l_i}{A_o l_o} = \sigma \frac{l_i}{l_o}$$

From the definition of strain,

$$\varepsilon = \frac{l_i - l_o}{l_o}$$

$$\frac{l_i}{l_o} = 1 + \varepsilon$$

$$\sigma_T = \sigma(1 + \varepsilon) \qquad \textbf{Equation 4.7}$$

For computing true strain under continuum conditions,

$$\varepsilon_T = \frac{\Delta l}{l} = \int \frac{\partial l}{l} = \left(\frac{l_o + \Delta l}{l_o}\right) = \ln\left(\frac{l_o}{l_o} + \frac{\Delta l}{l_o}\right),$$

$$\varepsilon_T = \ln(1 + \varepsilon) \qquad \textbf{Equation 4.8}$$

By using these definitions, engineering stress-strain can be converted into true stress-strain, as shown in Figure 4.19 for wrought normalized material. The analysis presented in this investigation will use engineering stress-strain when describing the YS, UTS and TE, and true stress when describing the strain hardening behavior (K and n) and creep deformation behavior.

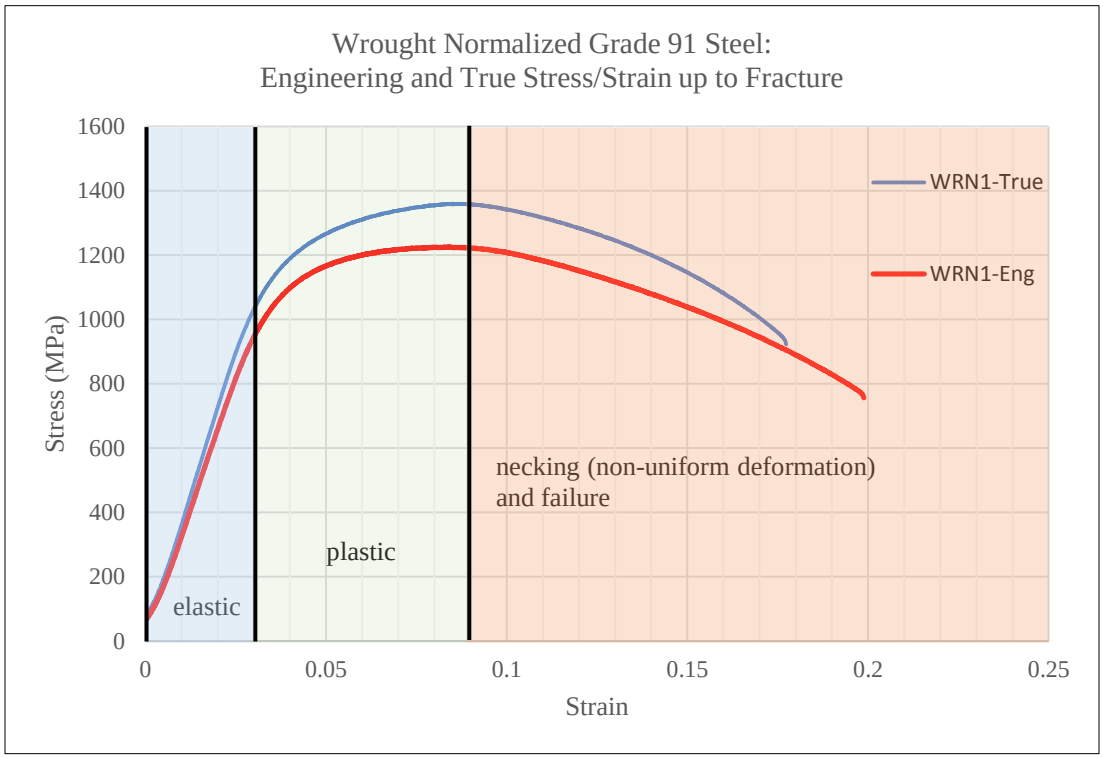

Figure 4.19. Engineering and true stress-strain for WRN specimen.

4.5.5. Creep and Strain Rate Testing Approach

As discussed subchapter 2.5, an engineering approach was taken to establishing the creep behavior of AM Grade 91 steel. Specifically, this experiment developed a methodology for calculating the steady state creep rate of AM Grade 91 in the secondary creep regime, where creep strain is generally linear with time.

When a constant stress results in a linear strain rate, then the linear secondary creep behavior is assumed, and the slope of that line is taken to be the steady state (minimum) creep rate ($\dot{\varepsilon}_s$) at that stress. It is the logarithmic function that describes the $\dot{\varepsilon}_s$ at a given temperature or stress that useful in estimating the rupture lifetime of a material.

Since the steady state creep rate is taken to be where strain hardening and elastic recovery are competing, the stress exerted on the specimen should be between the YS and UTS. In order to achieve this, to a linear stress value observed at a constant strain rate indicates $\dot{\varepsilon}_s$ has been reached. To generate a table of values for $\dot{\varepsilon}_s$, this strain rate was measured at a number of intervals within the strain hardening region of WRNT and AMNT specimens at 600 °C. This is known as a Strain Rate Jump Test (SRJT), and was achieved with the following procedure:

- Load specimen into vacuum furnace in load frame and heat to 600 °C
- Use strain rate of 10^{-4} to load specimen and observe force channel
- When specimen has reached its YS, jump to 10^{-3} strain rate
- Watch increase in stress value, and then plateau (at $\dot{\varepsilon}_s$)
- After a plateau is observed, decrease strain rate to 10^{-5}, watch elastic recovery, and resulting plateau
- Jump strain rate to 10^{-4} and then run until fracture

After carrying out this procedure, the stress/strain curve was generated, and a table of stress versus steady state creep rates ($\dot{\varepsilon}_s$) was generated.

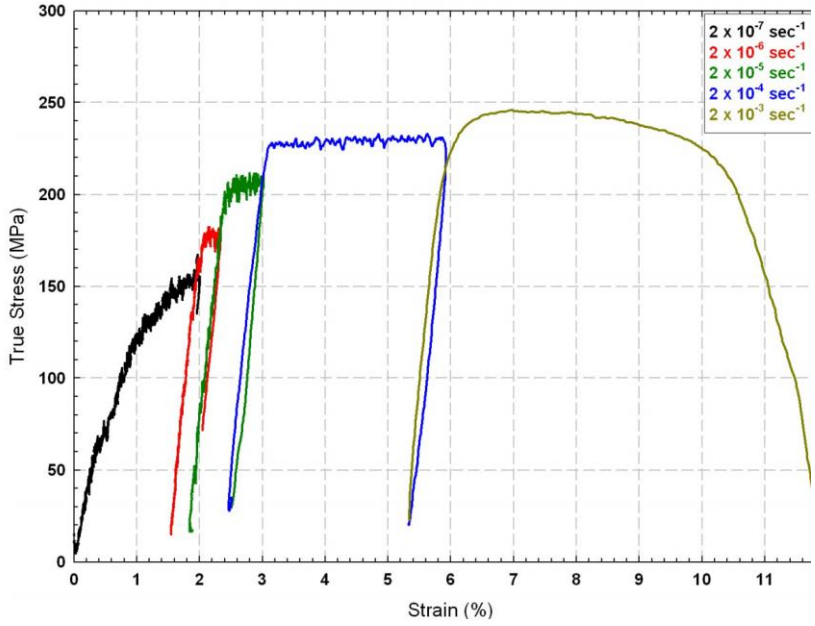

Figure 4.20. Strain Rate Jump Test (SRJT) illustration. Creep stress is the plateau values, and $\dot{\varepsilon}_s$ is the strain rate in the legend associated with that stress[98]

4.6. Method for Calculating Ion Damage

As described earlier in chapter 1, in a fast reactor, high-energy neutrons would scatter off Fe atoms (in Grade 91 steel targets), creating PKAs of Fe with recoil energy. By using the IBML positive ion accelerator to accelerate Fe ions directly, it is possible to simulate the effects of the initial PKA that would result from an n-Fe nuclear interaction. This "self-radiation" is essentially a shortcut in which, Fe^{2+} ions are accelerated into a Grade 91 steel target (mostly Fe), initiating a damage cascade with a PKA directly.

The IBML beam can accelerate Fe^{2+} ions up to a maximum 5 MeV. With penetration proportional to energy, this maximum value of 5 MeV was used to deliver the Fe^{2+} beam

peak as deep as possible. Stopping and Range of Ions in Matter (SRIM) and its complement, Transport of Ions in Matter (TRIM) [99] is open source scientific software that calculates the stopping and range of ions into matter based on tabulated physical data on interatomic bond structure and quantum mechanical treatment of ion-atom collisions.

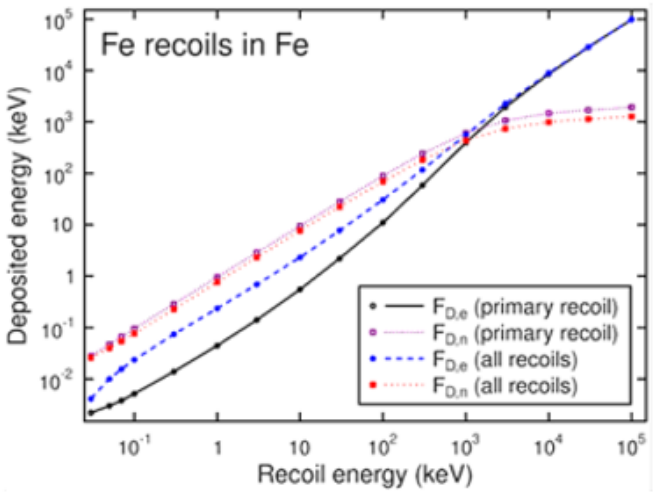

Figure 4.21. Recoil Energy vs Deposited Energy of Recoils in Fe-Fe Irradiation [103]

This calculation assesses the target's collective electronic structure and the charge state of the ion, and then uses the concept of effective charge to calculate electron excitation reactions and inelastic nuclear reactions. This includes using velocity dependent charge state data and long range screening due to the collective electron sea of the target. In this way, SRIM/TRIM calculates the amount of incident energy lost in inelastic excitation. Due to these interactions, there is not a 1:1 relationship between ion recoil energy and deposited energy. Figure 4.21 shows the deposited energy (F_D) for recoils of Fe ion self-irradiation. $F_{D,e}$, the "electronic" /ionization energy corrected term is obtained from the SRIM output file using the effective charge concept. The $F_{D,n}$, "nuclear" energy loss corrected term is the summation of the vacancies and phonons energy loss term percentages in SRIM.

The primary recoil data is obtained by including all the recoil energy loss fractions in the $F_{D,n}$ value of the primary recoil, while the "all recoils" data comes from the sum of the energy loss for electronic and nuclear energy loss.

At a given recoil energy, the difference between the curves illustrates that the total electronic deposited energy ($F_{D,e}$) is considerably higher when the electronic stopping of secondary recoils is also counted. For higher recoil energies, this difference disappears, and down to the threshold displacement energy, a round 20% of the initial recoil energy is lost to electronic stopping.

4.6.1. Determining Ion Penetration Range

To calculate the ion penetration range, the 5 MeV target and ion information were input into SRIM and executed. A SRIM-generated data file of the displacements and penetration depths was created. This input file file (Figure 4.22) was used with the KP model to generate a depth map (Figure 4.23) and depth histogram (Figure 4.24). Displacement

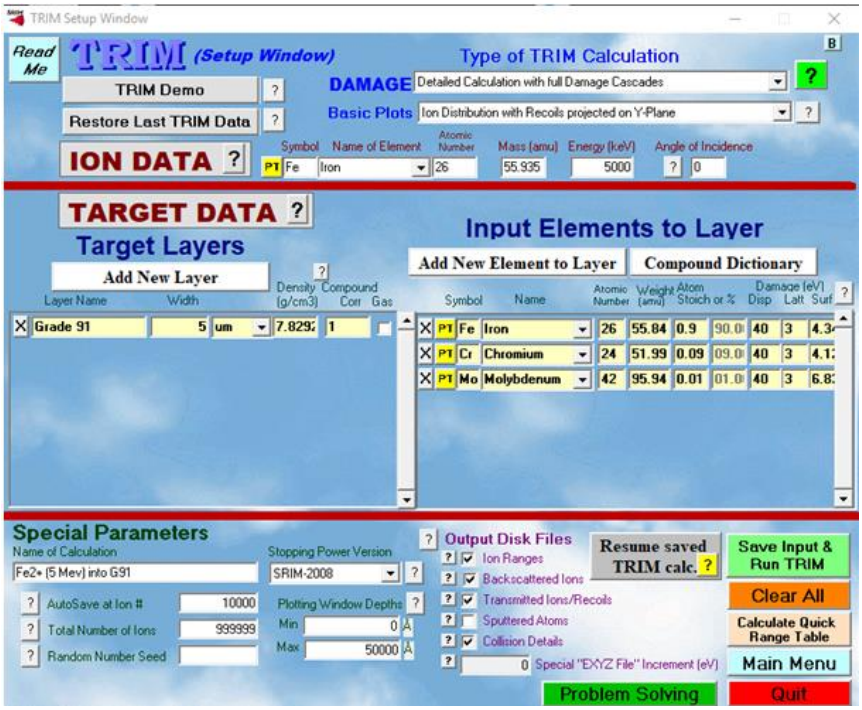

Figure 4.22. SRIM/TRIM input file

generation map (Figures 4.24) and establishing a damage peak at ~ 1.38 µm beneath the sample surface.

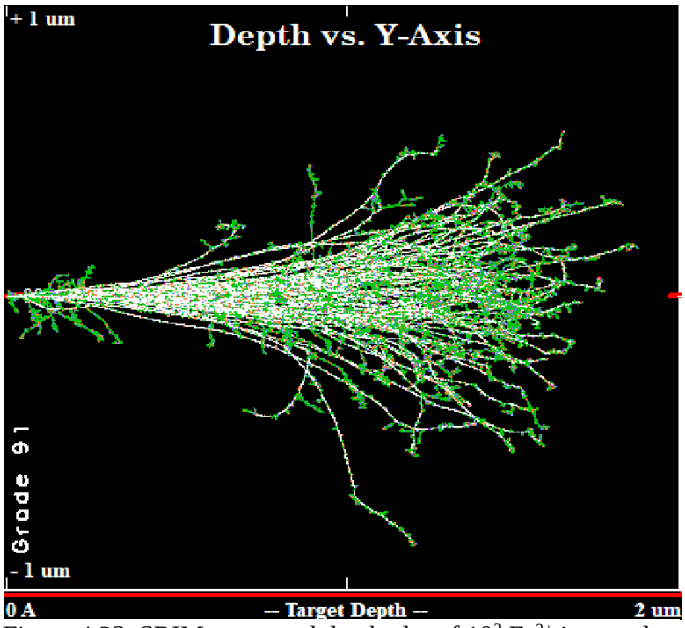

Figure 4.23. SRIM-generated depth plot of 10^3 Fe^{2+} ions and recoils into Grade 91 Steel

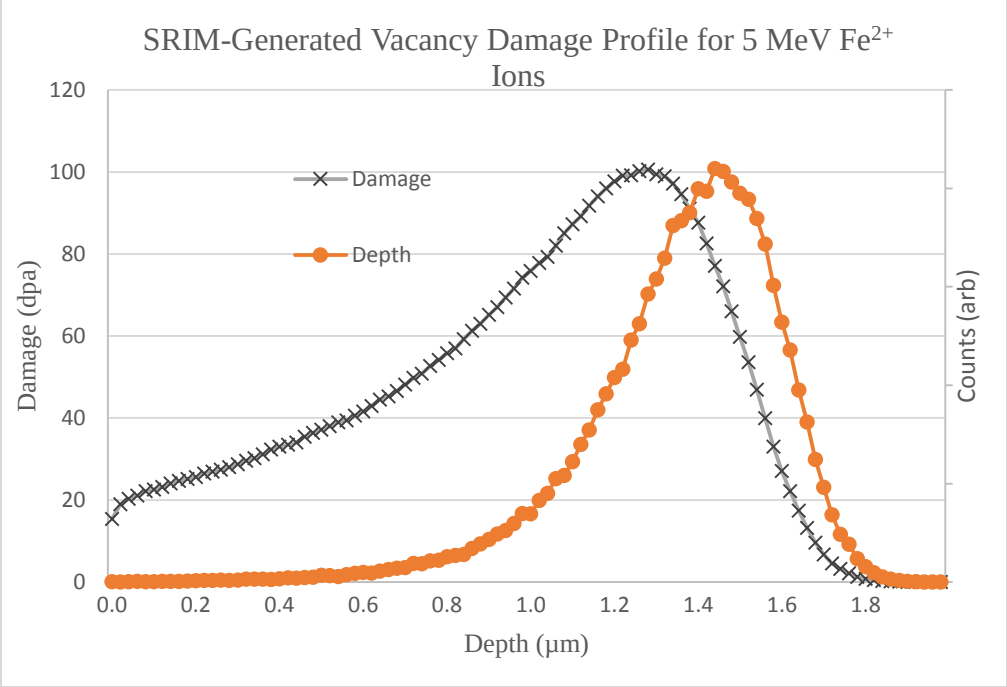

Figure 2.24. Depth and damage profile generated in SRIM/TRIM

4.6.2. Determining Lattice Damage Rate from 5 MeV Fe^{2+} Ion Flux

All irradiations were carried out at 450 °C. This temperature was chosen because it is low enough to prevent excessive annealing, and is in the middle of the fast reactor operating range. After determining the damage map and range, the next step was to calculate the rate at which the 5 MeV Fe^{2+} ion beam could produce damage at the Bragg Peak location, up to 100 dpa. Using SRIM simulation feedback, a peak damage of 1 dpa is achieved with ~10^{15} incident 5 MeV Fe^{2+} ions.

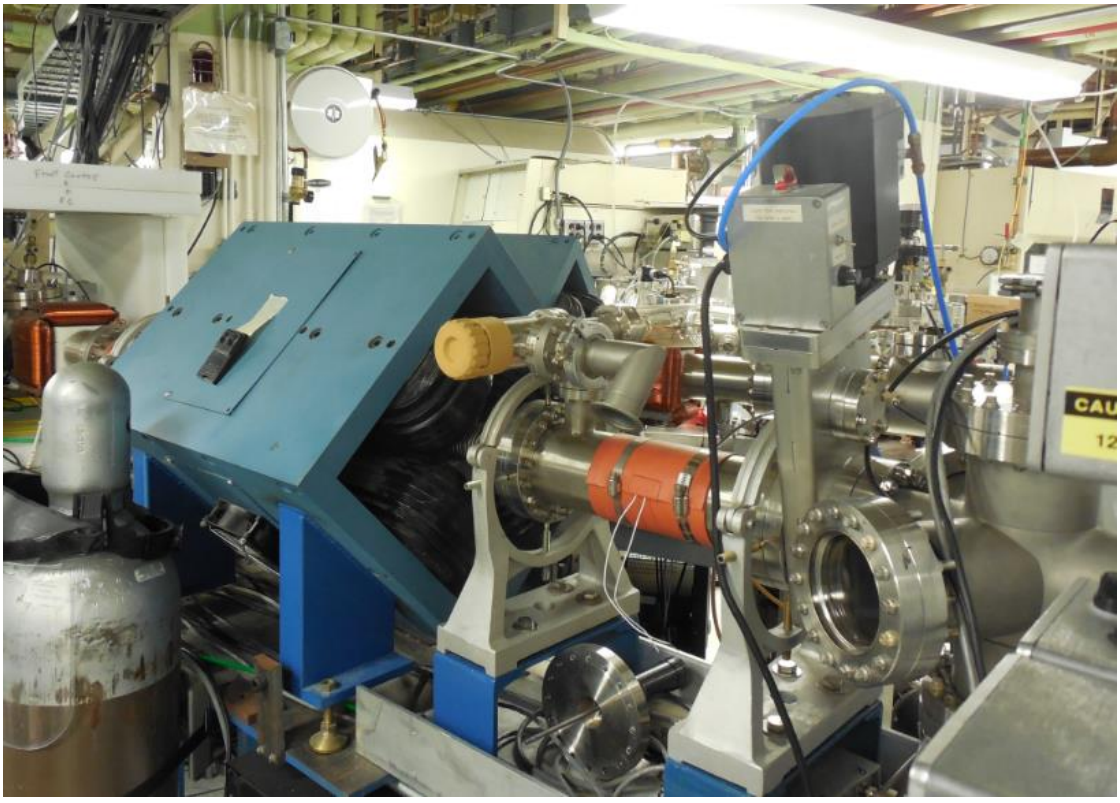

Figure 4.25. IBML Beam Line.

For Fe ion irradiation, the IBML accelerator system begins with molecules of the oxidized iron mineral hematite (Fe_2O_3), which are magnetically separated into O and Fe by mass ratio, and then the Fe^{3+} and Fe^{2+} ions are separated by charge. The Fe^{2+} ions are then accelerated by an additional voltage source up to the maximum beam voltage (5 MV), creating a stream of 5 MeV Fe^{2+} ions accelerating towards the irradiation chamber.

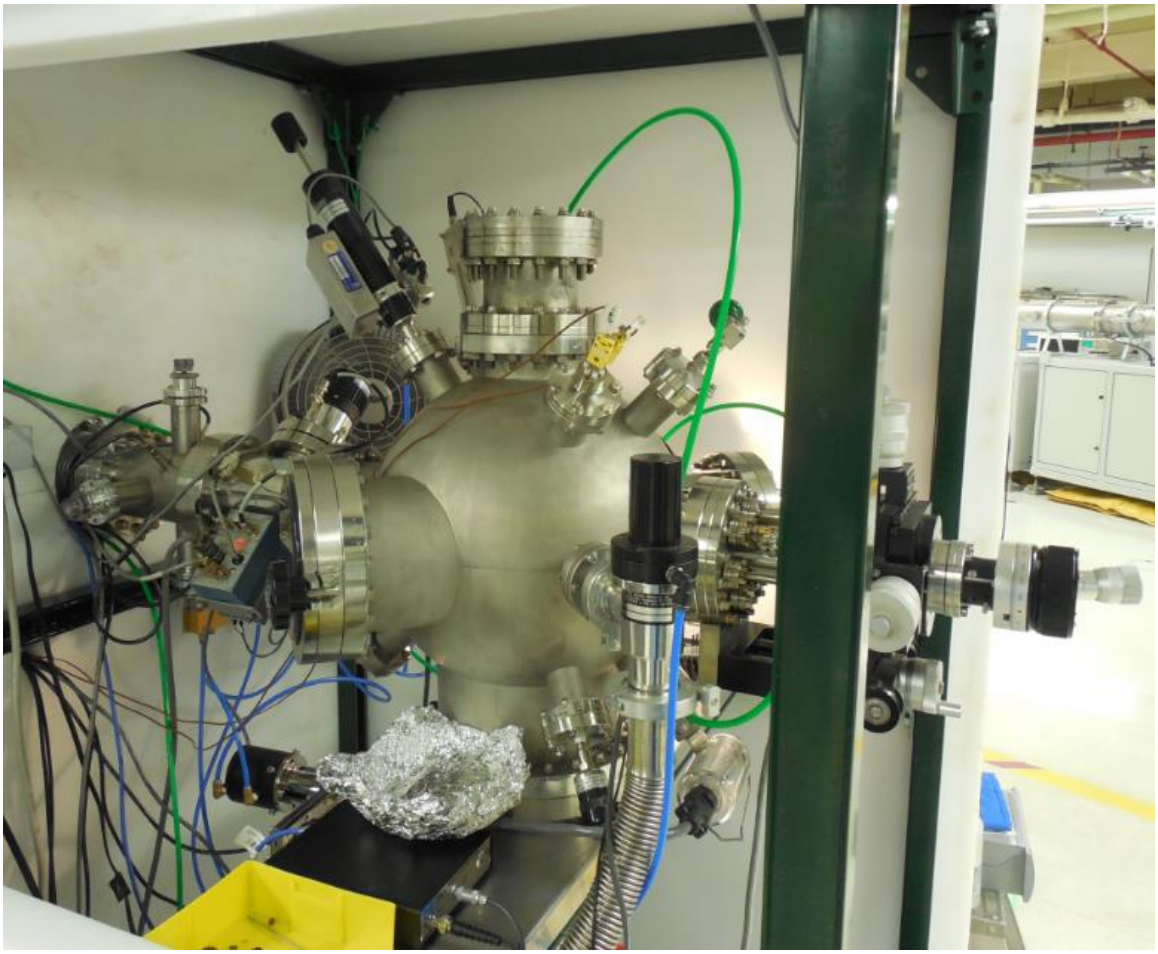

Figure 4.26. IBML Irradiation Chamber

By measuring the electrical current entering the irradiation chamber with a real-time faraday cage, it is possible to convert the current measurement to ion flux using the fundamental atomic charge definition, such that ~ 2hrs at 210 nA produced ~15 dpa. With

this estimated electrical current requirement, the specimens were loaded into the irradiation chamber (Figure 4.26-27).

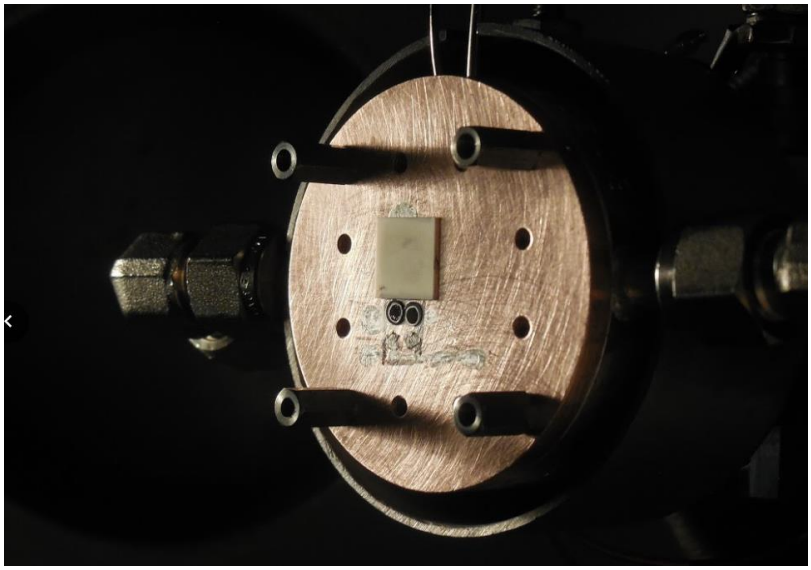

Figure 4.27. Copper plate with mounted Grade 91 specimens in irradiation chamber.

Because the mounting plate is copper, the only Fe the that the ions are incedent upon are the actual specimens. Thus, an x-ray detector can detect a signal at the x-ray K-edge x-ray absorption energy of Fe (7.112 keV) that is proportional to the incident intensity. A short measurement at the initial electrical current can thus generate an x-ray intensity proportional to the damage rate. This technique was used as an additional method to calculate when the specimens had reached 30 dpa.

This method was used to calculate that 30 dpa would be reached around 478,000 x-ray counts in the peak centroid. When this x-ray count was reached, the beam was turned off, and one of each WRNT and AMNT specimens were removed. After removal, the same method was used to irradiate the remaining specimens an additional 70 dpa. The x-ray counts are given in Figure 4.28. After 30 and 100 (total) dpa were achieved, the specimens were removed for nanohardness testing.

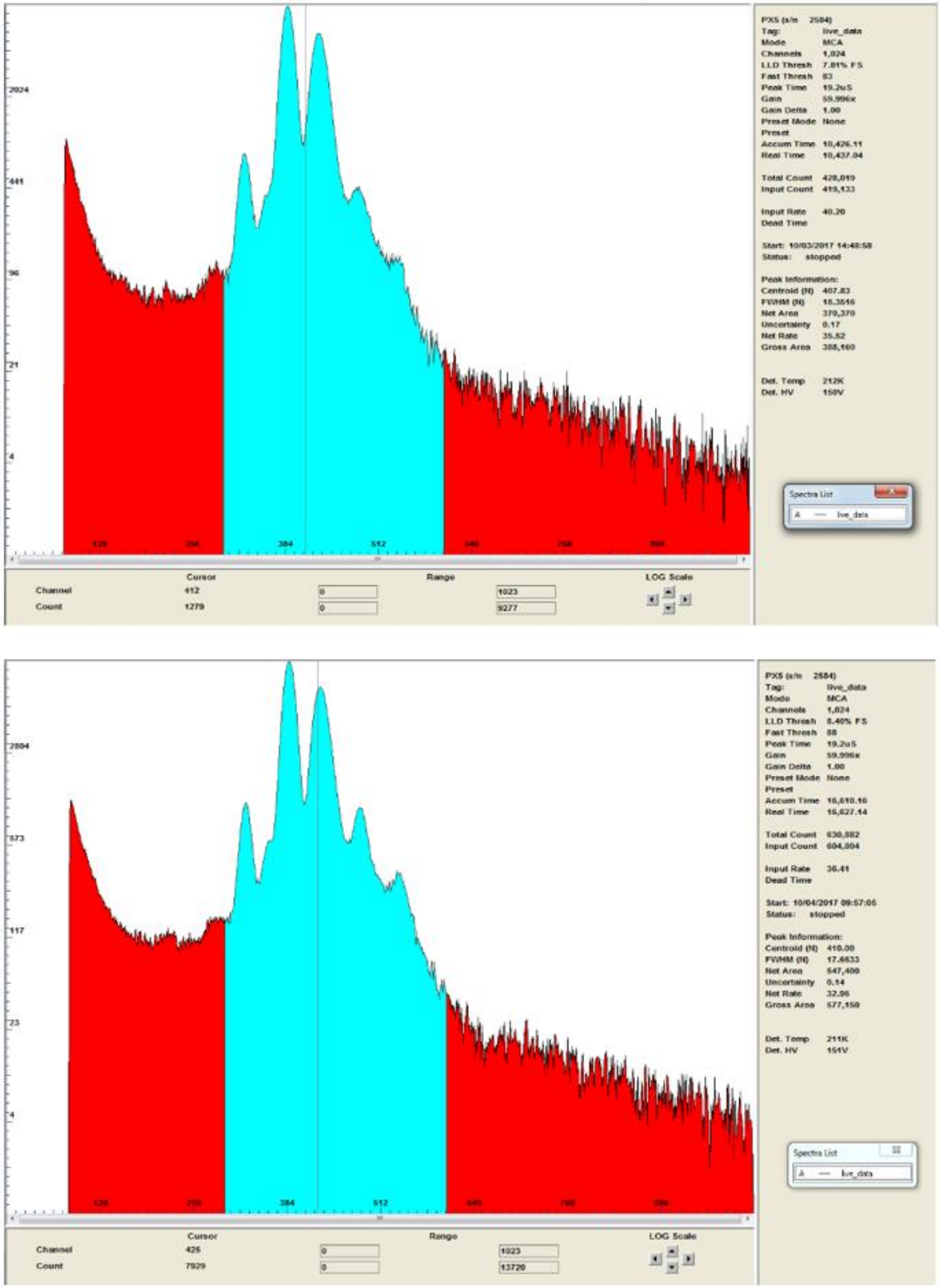

Figure 4.28. X-ray counts for 30 and 70 dpa irradiations.

4.7. Nanoindentation and Hardness Testing

Precision nanoindentation is a common testing procedure used for determining the surface hardness of materials. At scales in the hundreds of nanometers, it has been shown that the indenter tip interaction volume extends far beyond its penetration depth. Prior to this irradiations carried out in this investigation, similar nanohardness measurements were carried out as part of the LANL LDRD project by Weaver (et al.) on specimens that had been irradiated at 0, 3, and 30 dpa. From the estimates in the Oliver-Pharr method [104], hardness measurements through the nanoindentation range interaction region were chosen to be mean hardness measurements in the displacement depth of 100 – 300 nm. Using the assumed ~3-5 factor depth interaction volume, this corresponds to an interaction volume in the range of 300 to 1500 nm. While this range is considerably wide, it ensures that the nanoindenter interaction region does in fact pass through the peak dpa region.

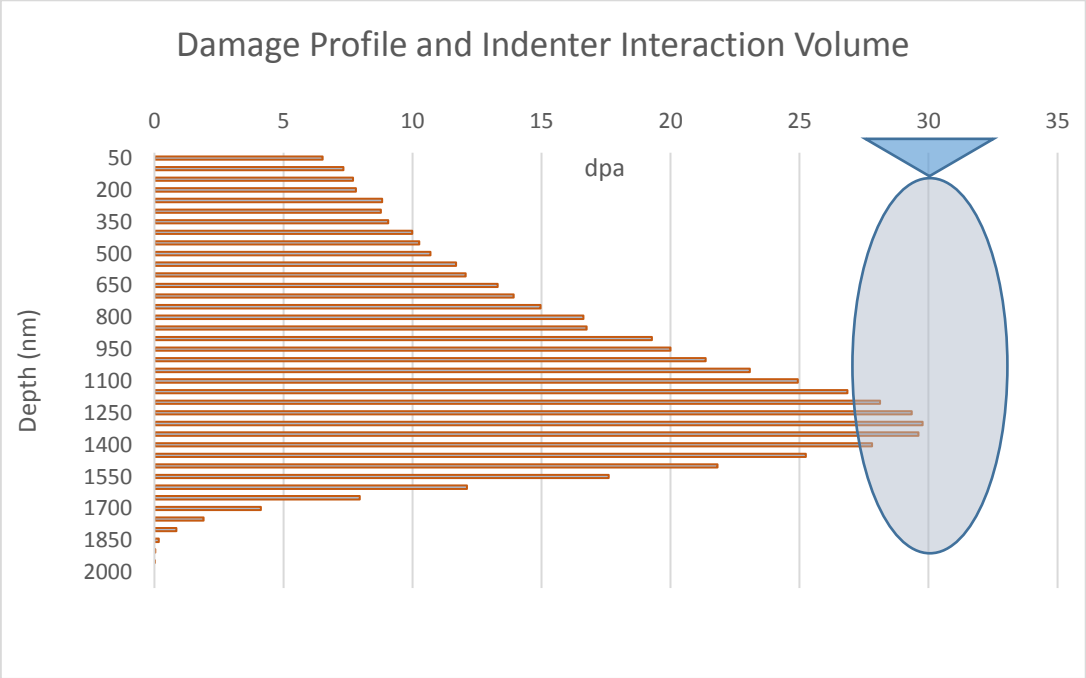

Figure 4.29. Damage region plotted with interaction volume of nanoindenter.

By using the modified Oliver-Pharr method, the interaction volume of the nanoindenter was ensured to pass through the peak radiation damage layer (and into the unirradiated layer). The machine used was an Agilent Technologies Nano Indenter G200™, commercially available and on site at LANL's Materials Testing Laboratory.

Irradiated specimens of AMNT and WRNT (30 dpa and 100 dpa) were loaded onto the nanoindenter, and an optical microscope was used to find a smooth, relatively featureless region on electro polished surface of the specimens. Upon completion of nanoindentation, force/shape data was output for analysis (Chapter 7).

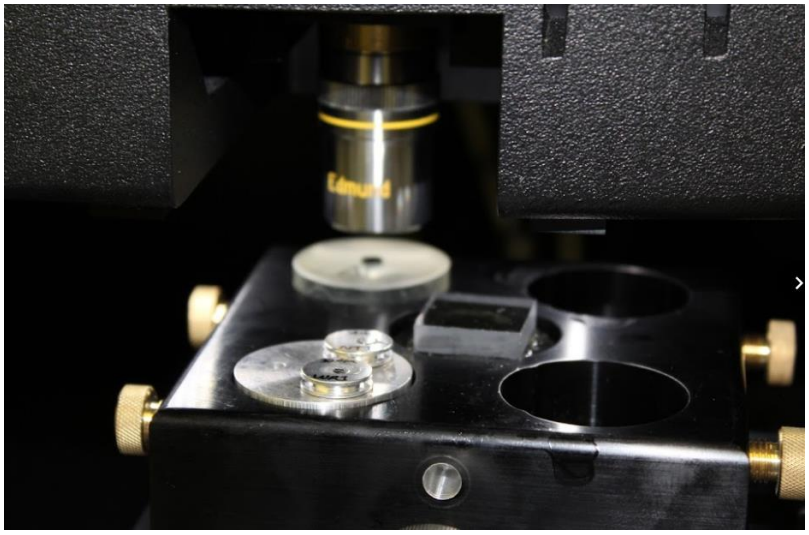

Figure 4.30. Photo of specimens in nanoindenter.

Figure 4.31. Nanoindentation locations of 36 data points for AMNT (left) and WRNT (right) specimens

5. Results of Microstructural Characterization of Grade 91 Steel

5.1. EBSD and Optical Microscopy Characterization

EBSD and optical micrographs were taken of each of the specimens to determine crystallographic direction and microstructural features. The AM As-deposited material (AMAD) shows a highly disordered grain structure, with widely varying grain sizes and a large degree of heterogeneity. This is not unexpected, as the fabrication process by nature causes uneven and unpredictable heating and cooling cycles within the material. In a sense, the fabrication process itself is akin to welding. However, unlike welding, the DMLS process results in incidental heating and re-heating of volume elements according to the hatch spacing, speed, and power of the sintering laser. This results in highly unorthodox heating and cooling cycles that vary in position and magnitude as the specimen is built, layer by layer. For a FM alloy, whose non-equilibrium phase formation is dependent on cooling rates, this results in a chaotic microstructure consisting of large featureless regions, punctuated with complex fine-grain regions throughout.

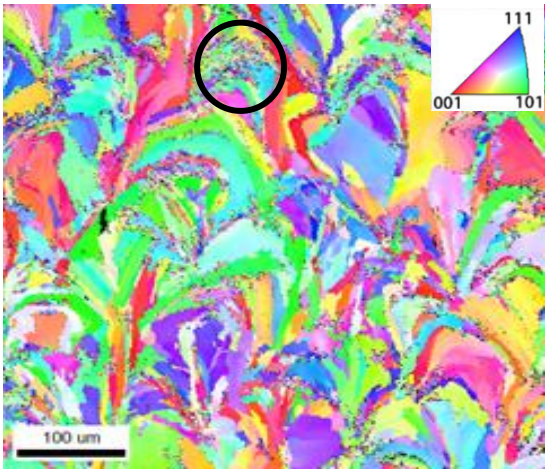

Figure 5.1. EBSD Image of As-Deposited Grade 91 Material (fine-grain region emphasized)[105]. Image taken by B. Eftink. Used with permission.

As part of a concurrent LDRD project on AM of FM steels, the fine-grain regions of the microstructure were interrogated with a Focused Ion Beam (FIB) system at LANL. These regions were found to have high plastic strain in the form of dislocations, as well as platelets of martensite. The "speckel" features described in Figure 5.2. are likely due to subgrains on the order of hundreds of nm in size. Worth noting, is that the fine-structure areas with high dislocation densities are similar in size and density to the wrought (normalized and tempered) material, and thus may have similar potential for resisting radiation damage.

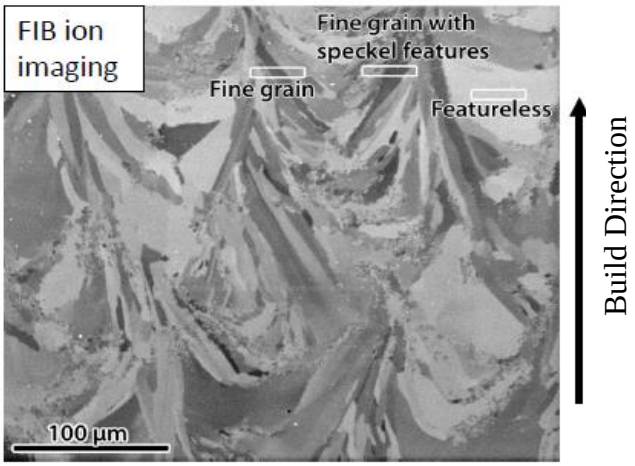

Figure 5.2. Focused Ion Beam Image of AMAD material[105]. Image taken by B. Eftink. Used with permission.

5.1.1. Direct Tempered AM Grade 91 Material

Direct tempered material (AMT) was also characterized using FIB analysis. The overall microstructure did not change significantly; 760 °C is below the austenization temperature, but within the temperature region that promotes carbide precipitation. As expected, the FIB analysis showed the presence of $M_{23}C_6$ carbides at the grain boundaries in the fine grain regions (Figure 5.2). This carbide formation is typical of Grade 91 steel, and generally makes up about 1.5% (by weight) of the material in the base case (WRNT).

Additionally, the AMT specimen showed less prevalence of martensite platelets, though the dislocation density remained similar to that within the AMAD specimen. The overall reduction of microstructural features brought upon by tempering will likely decrease the radiation tolerance of AMT material, since it will offer fewer sink sites for point defects formed under irradiation.

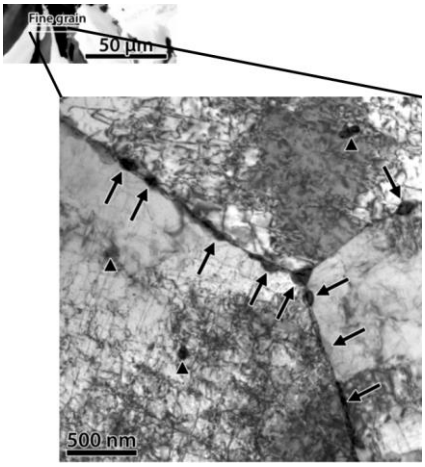

Figure 5.3. High magnification TEM image showing presence of $M_{23}C_6$ Carbides along Grain Boundaries[105.] Image taken by B. Eftink. Used with permission.

5.1.2. Normalized and Tempered AM Grade 91 Material

Finally, AM specimens that were given the full normalization and tempering heat treatments were analyzed. EBSD imaging showed a profound difference in the new microstructure of the heat-treated AM material (Figure 5.4). The average grain size was drastically reduced, resulting in a large degree of homogeneity as compared with the As-deposited (AMAD) specimen. Small grain size is advantageous in that it increases the material strength (according to the Hall-Petch correlation), as well as resulting in a high grain boundary (GB) density, which act as defect sink sites for irradiated materials.

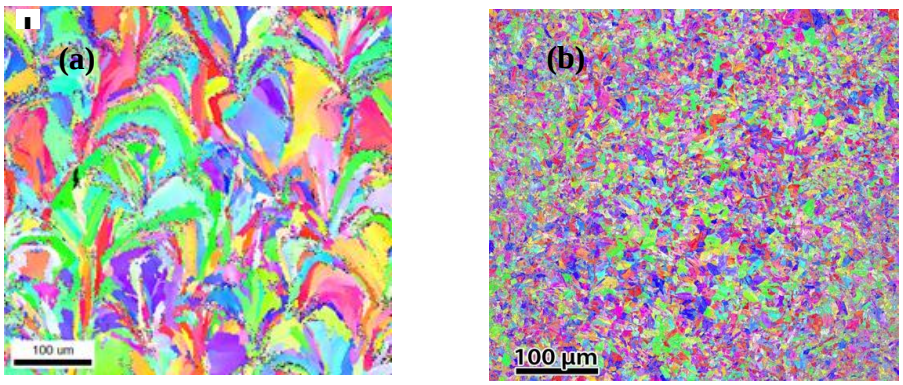

Figure 5.4. EBSD Micrographs of (a) As-deposited (AMAD) and (b) Normalized & Tempered (AMNT) AM Material[105]. Image taken by B. Eftink. Used with permission.

Following the EBSD comparison of pre and post heat treated AM material, the AMNT material was compared with the base case material (WRNT). The WRNT material displays the characteristic martensitic lath structure of Grade 91 material, but the AMNT sample shows a significant shrinkage of prior Austenite grain size, with smaller overall grain size. As with the AMT material, this smaller grain size is beneficial from a radiation tolerance standpoint, and Chapter 7 will discuss the results of ion beam irradiation on these materials.

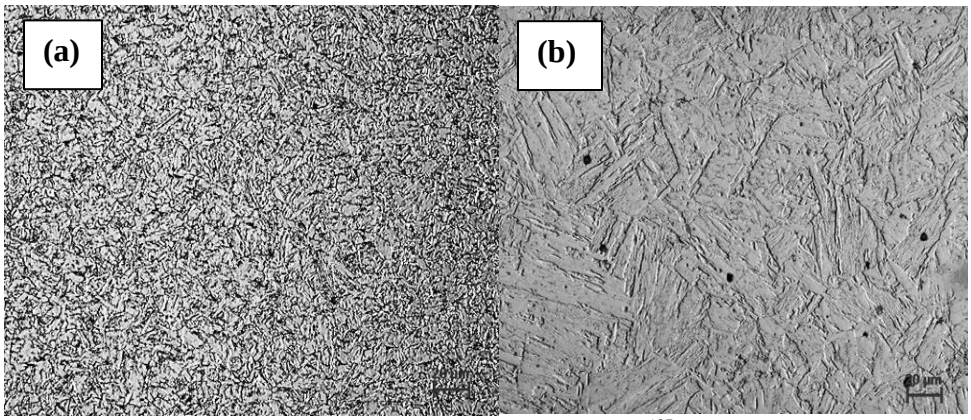

Figure 5.5. AMNT (a) and WRNT (b) Grade 91 Specimens[105]. Image taken by B. Eftink. Used with permission.

5.1.3. Identification of Grade 91 Phases with XRD

A typical 2D diffraction pattern was collected and plotted for Grade 91 samples (Figure 5.6). In such a pattern, incident angle is represented by the radial distance and intensity by color.

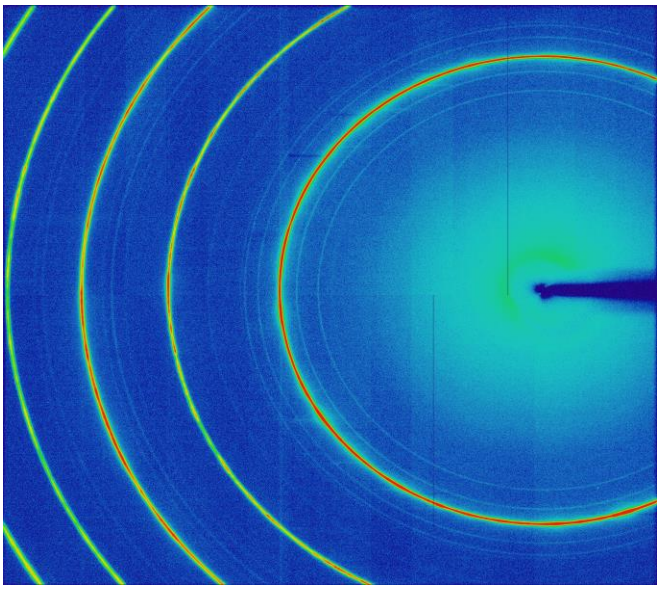

Figure 5.6. 2-D Diffraction Pattern for Grade 91 Specimens[102].
Image taken by D.Sprouster. Used with permission.

A 1-D plot of intensity vs angle was also generated (Figure 5.7), in which crystallographic libraries along with the Rietveld method was used to identify peaks, refine peak shapes, determine grain size and lattice parameter, and determine constituent fractions according to phase.

Analyzing Figure 5.7, the most obvious constituent, Fe, was identified by its α phase (ferrite – BCC) around 5.25 degrees, which was the most prominent peak in all samples. Additionally, some samples contained FCC peaks, which were identified as

retained austenite (γ phase Fe). These specimens with appreciable retained austenite were grouped together (top 4), and those that showed the prevalence of carbides (and not austenite) were grouped together (bottom 4). The eight specimens are included together on a single inset plot with the (110) diffraction peaks identified for comparison.

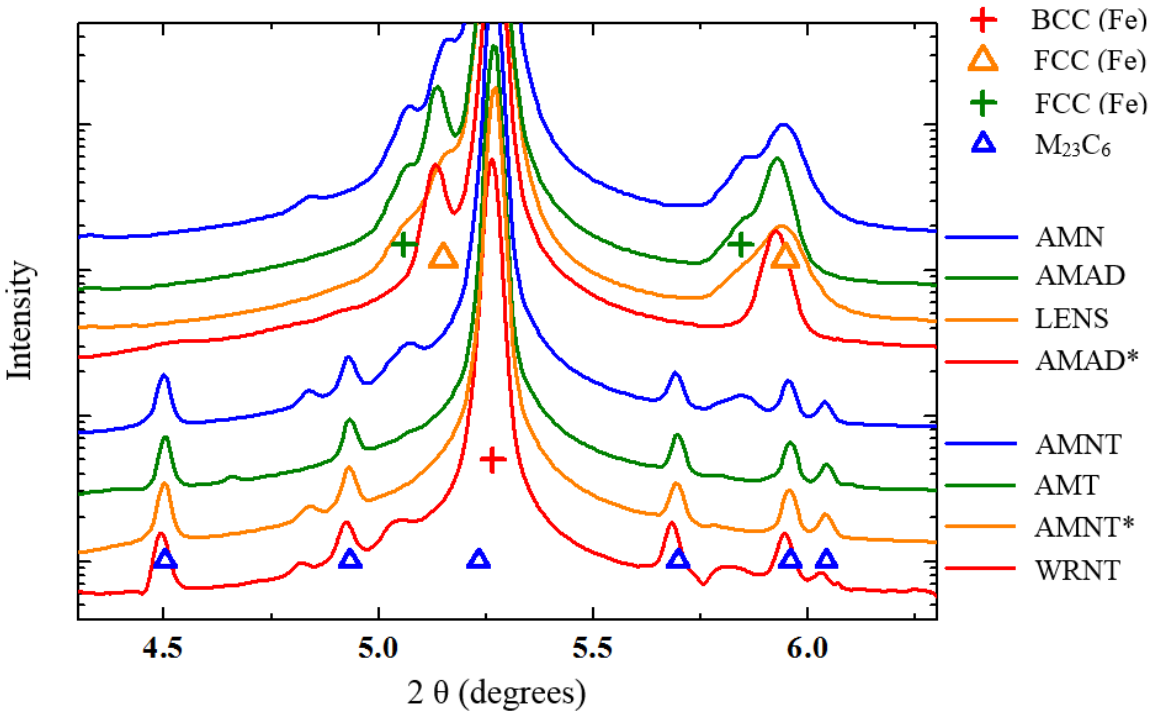

Figure 5.7. XRD Spectrum showing known Fe BCC (α-ferrite), Fe FCC (γ-austenite), and location of M23C6 peaks[102]. Analysis performed by D. Sprouster. Used with permission.

As expected, the As-deposited specimens (AMAD, AMAD*, and LENS) and normalized specimen (AMN) clearly show retained austenite (around 5.15 and 5.9 degrees). Tempered specimens show the presence of carbide precipitates ($M_{23}C_6$), and small residual peaks in two of the three normalized and tempered (AMNT and WRNT) suggest a small portion of retained austenite is still present after tempering. In comparing AMAD* and AMAD (Build 1 and Build 2, respectively), there appears to be some retained austenite in the AMAD build, but not the AMAD* build. This indicates that as

hypothesized in Chapter 1, that reproducibility and quality may be an issue in As-deposited material, especially as it relates to AM technologies for which time and temperature-dependent phenomena drive microstructure structure.

5.1.4. Quantification of Grade 91 X-Ray Diffraction Spectrum

After identifying the primary phases in the spectrum, Reitveld refinement method was used to refine the spectrum, determine lattice parameters and quantify the constituents by mass fraction. Upon refinement of peak shifts, it was shown that the FCC lattice parameters in the three As-Deposited specimens (AMAD, AMAD*, and LENS) are slightly different from that compared to the known austenite FCC phase (0.3591 nm) [102]. Typically, this type of shift is due to chemical impurities, large vacancy concentrations, residual stresses, or combinations thereof. These are likely results of the process conditions of the DMLS and LENS processes themselves. The identification of these anomalies provide a confirmation that FCC phases in non heat treated As-deposited specimens have distinct microstructural differences from pure austenite. Conversely, the AM normalized specimen's (AMN) FCC diffraction peaks lined up more precisely with the austenite FCC lattice parameter, thus demonstrating that the normalization heat treatment rendered the austenite phase of the AM specimen uniform.

A summary of Rietveld refinement fits for each sample is given in Table 5.1, giving lattice parameter, grain size, strain, and mass fraction, with associated errors. As previously stated, the As-deposited and normalized specimens contain ferrite (BCC), retained austenite (FCC), and (presumably) martensite (BCT). The percentage of austenite in these untempered specimens varies from 3.4% to 5.8%. In the tempered specimens, carbides

were present at concentrations of 1.1% (direct tempered AM) to 2.2% WRNT. Retained austenite in all tempered specimens was below 1%.

Table 5.1 Summary of Rietveld fits for all specimens[102]. Analysis performed by D. Sprouster. Used with permission.

phase	**lattice par**	**err±**	**grain size**	**err±**	**strain**	**err±**	**fraction**	**err±**
id	**(nm)**		**(nm)**		**-**		**(%)**	
sample	**AMN**							
BCC	0.287292	0.00008	105.8	3	0.9	0.007	94.1	0.2
FCC	0.359662	0.00057	23.6	2.5	0.97	0.067	4.7	0.1
FCC	0.366022	0.00131	42.7	16	0.87	0.138	1.1	0.1
sample	**AMAD**							
BCC	0.287272	0.00007	142	4.8	0.59	0.006	94.4	0.2
FCC	0.360847	0.00046	24.6	6.1	0.6	0.005	4.1	0.1
FCC	0.365576	0.00251	16	6.5	1.13	0.2	1.5	0.1
sample	**LENS**							
BCC	0.28735103	0.00009	135.6	4.7	0.901	0.007	95.6	0.2
FCC	0.35989558	0.00093	24.6	3.9	1.289	0.101	3.8	0.1
FCC	0.36629472	0.00361	31.6	19.3	0.976	0.322	0.6	0.1
sample	**AMAD***							
BCC	0.287184	0.00005	196	6.5	0.375	0.005	96.6	0.1
FCC	0.361214	0.00032	37	3.2	0.592	0.046	3.4	0.1
sample	**AMNT**							
BCC	0.287239	0.00003	487.8	16.5	0.202	0.004	98	0.1
FCC	0.366401	0.00121	44.1	26.5	1.48	0.17	0.5	0.1
$M_{23}C_6$	1.063221	0.00078	93.2	15	0.19	0.04	1.24	0.1
sample	**AMT**							
BCC	0.287236	0.00003	1031.5	66	0.119	0.006	98.8	0.1
$M_{23}C_6$	1.062567	0.00086	139.9	30	0.14	0.05	1.1	0.1
sample	**AMNT***							
BCC	0.287144	0.00003	539.8	25.2	0.15	0.006	98.5	0.1
$M_{23}C_6$	1.06293	0.00063	156.9	48.5	0.25	0.044	1.3	0.1
sample	**WRNT**							
BCC	0.287519	0.00004	287.1	17.3	0.15	0.011	96.9	0.1
FCC	0.367431	0.00186	12.5	2.7			0.7	0.1
$M_{23}C_6$	1.064624	0.00098	62.5	16.7	0.22	0.08	2.2	0.1

It is worth noting that upon initial analysis, the α' martensite phase (BCT) was not distinguishable from the BCC peak. Thus, the BCC fraction in Table 5.1 represents the sum of both the BCC (ferrite) and BCT (martensite) phases. Martensite lath grain structures were observed in optical micrographs of both AM and wrought Grade 91 material. With this knowledge, the previous Rietveld fits were revisited to distinguish the BCC and BCT phases that were manifested in the large BCC peak. By overlaying the expected BCC, FCC, and BCT phases, and superimposing them with the measured data, the individual peaks for Fe BCC, FCC, and BCT were deconvoluted using the commercially available TOPAS™ software package by BRUKER, Inc. This superimposition is illustrated in Figure 5.8.

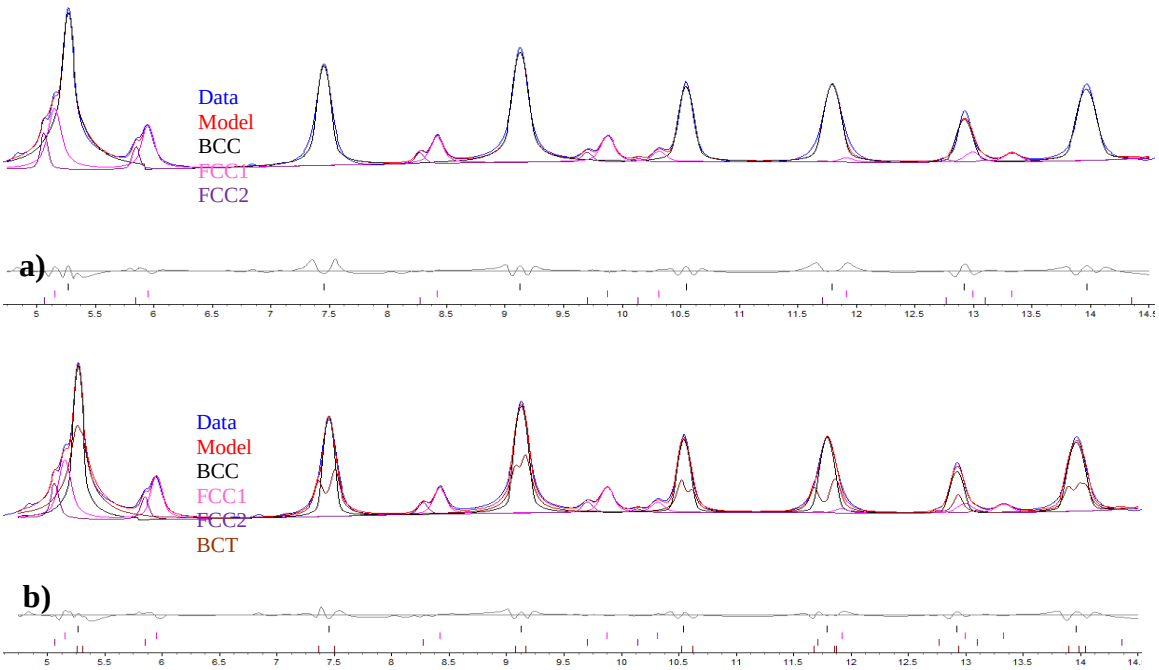

Figure 5.8. Overlay of BCT (martensite phase) on measured XRD spectrum without (a) and with (b) BCT correction. Analysis performed by D. Sprouster. Used with permission.

A selected region of the BCT overlay is emphasized in Figure 5.9, in which the BCT peaks are visible within the BCC peak. Using this quantification technique, the

martensite fractions were calculated from within the ferrite BCC peaks, and the results summarized in Table 5.2

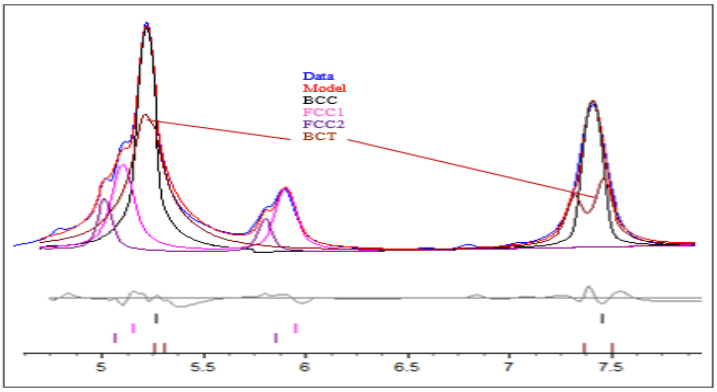

Figure 5.9. Overlay of BCC and BCT spectra

phase id	lattice par (nm)	err±	lattice par (nm)	err±	grain size (nm)	err±	fraction %	err±
sample	**AMN**							
BCC	2.87301	0.00008					78.60	0.41
FCC	3.59699	0.00037			23.3	1.7	4.10	0.09
FCC	3.65945	0.00084			32.7	6.3	1.10	0.06
BCT	2.85365	0.00043	2.90573	0.0006	42.3	2.0	16.20	0.41
sample	**AMAD**							
BCC	2.87164	0.00006					76.10	0.50
FCC	3.60860	0.00030			69.0	9.8	3.50	0.10
FCC	3.65653	0.00153			29.5	6.7	1.20	0.10
BCT	2.86187	0.00034	2.89670	0.0004	30.5	1.0	19.20	0.50
sample	**LENS**							
BCC	2.87421	0.00009					80.60	0.40
FCC	3.59893	0.00059			22.6	2.4	3.40	0.10
FCC	3.65076	0.00271			20.6	6.3	0.70	0.10
BCT	2.85232	0.00036	2.90590	0.0005	24.8	1.0	15.30	0.40
sample	**AMAD***							
BCC	2.87211	0.00005			-	-	81.80	0.61
FCC	3.61203	0.00022			50.7	4.5	2.80	0.10
BCT	2.86112	0.00030	2.88950	0.0004	38.3	1.5	15.40	0.60

Table 5.2 Summary of BCT-corrected Rietveld fits for martensite-bearing specimens. Analysis performed by D. Sprouster. Used with permission.

Using this method, the martensite fractions were determined to be between 15.3% in the LENS specimen and 19.2% in the AMAD specimen. This result indicates that despite nontraditional heating cycles, martensite transformation occurs in both the powder bed system (DMLS) that was used to fabricate the AMAD specimen, and in the powder feed LENS system. Strangely, however, there was a relatively large difference (15.4% vs 19.2%) in the martensite fraction detected in subsequent builds in the DMLS system. This result suggests a strong dependence on position and likely on build direction in DMLS AM systems.

5.2. Analysis of Room Temperature Tensile Sample Fracture Surfaces

SEM fractographs of four of the room temperature broken tensile specimens were taken (Figure 5.10). Each heat treatment and fabrication type resulted in a specimen with markedly different fraction behavior. As discussed in subchapter 2.8, the most obvious signs of ductile fracture are high deformation/reduction in cross section, and in the fibrous surface appearance on the fracture face itself.

From the perspective of elongation, the WRNT and AMNT specimens clearly show a decrease in the cross sectional area orthogonal to the tensile load. The As-Deposited specimen (AMAD) shows some elongation, along with cracks that originate from the central region. The normalized-only specimen showed the least elongation, though it is still evident to some degree.

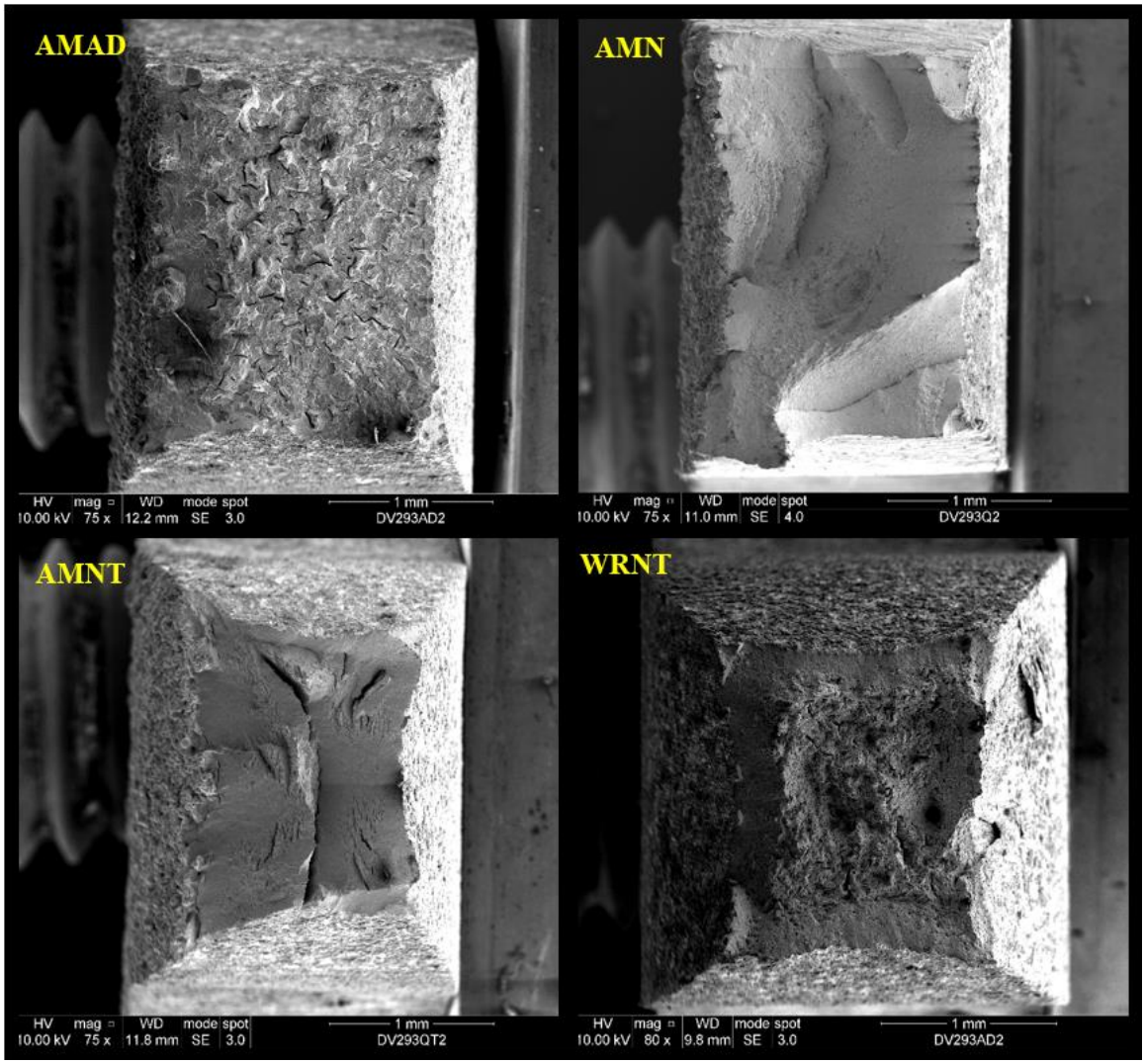

Figure 5.10. SEM of fracture surfaces of four selected room temperature tensile specimens.

The WRNT and AMAD specimens have dull faces, though only the WRNT specimen exhibits the characteristic fibrous textured face features indicative of classic cup-and-cone ductile fracture. Additionally, the WRNT specimen seems to exhibit the slant fracture "picture frame" behavior described in the previous section, known to appear in rectangular specimens whose 45 degree shear stress concentration is indicative of ductile fracture.

The demonstrable and predictable response of the AM and wrought material to the code-prescribed heat treatments provides additional evidence that the heat treatments for

wrought material are likely appropriate for AM material as well. The mechanical properties of AM and wrought material also show similar behavior as functions of heat treatments (discussed in the next chapter), indicating that future work should include optimizing these heat treatments for improving and tailoring their properties for intended use.

5.2.1. Wrought Normalized and Tempered Specimen

The WRNT, or base case specimen, fractured as expected for ASME Grade 91 material. It showed the typical 45 degree cup and cone slant fracture in the "picture frame" shape described in Subchapter 2.8.1, as well as transgranular fracture and dimples; this is a hallmark ductile fracture.

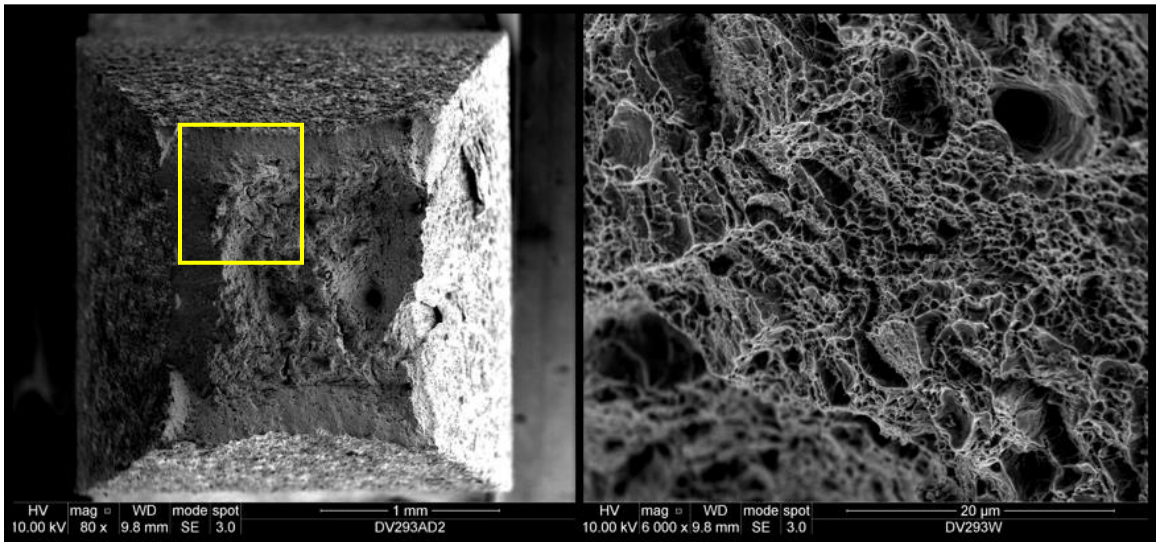

Figure 5.11. Wrought Normalized and Tempered (base case) fracture surface showing shear lip and ductile fracture dimples.

5.2.2. As-Deposited Fracture Surface Analysis

The AMAD specimen fractograph did not exhibit obvious characteristics of ductile fracture. In fact, at 200x magnification, cracks in the range of 50 – 100 µm

become apparent, originating near the center and extending part of the way towards the perimeter. However, as is shown in Chapter 6, the AMAD material exhibited more than 17% total elongation, most of which was uniform elongation. Such behavior suggests that the fracture behavior is governed by the ductile properties of the matrix, but that there is brittle behavior in the martensitic platelet regions.

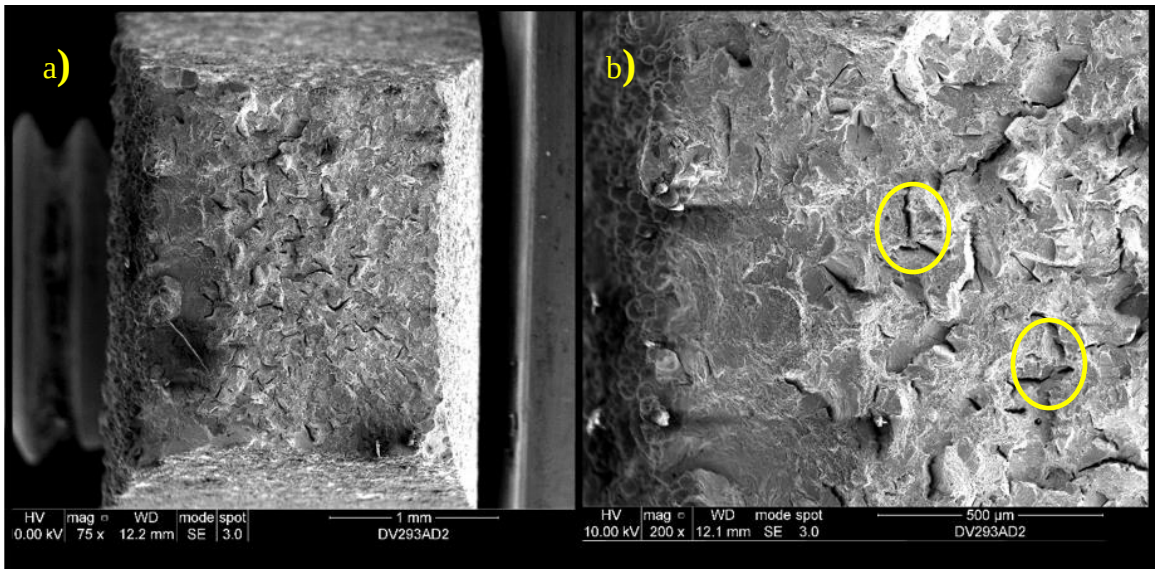

Figure 5.12. AMAD Fracture Surface at (a) 75x and (b) 200x Magnification, showing cracking in brittle region.

In addition to examination of the fracture surface, SEM magnification (1500x), reveals the "balling" phenomenon at the surface, which is associated with DMLS AM methods. At further magnification still, the non-homogenous microstructure of the AMAD specimen becomes clear once again, revealing a highly disordered structure containing both fine-grain porous regions (yellow) and featureless regions (red), as shown in Figure 5.13.

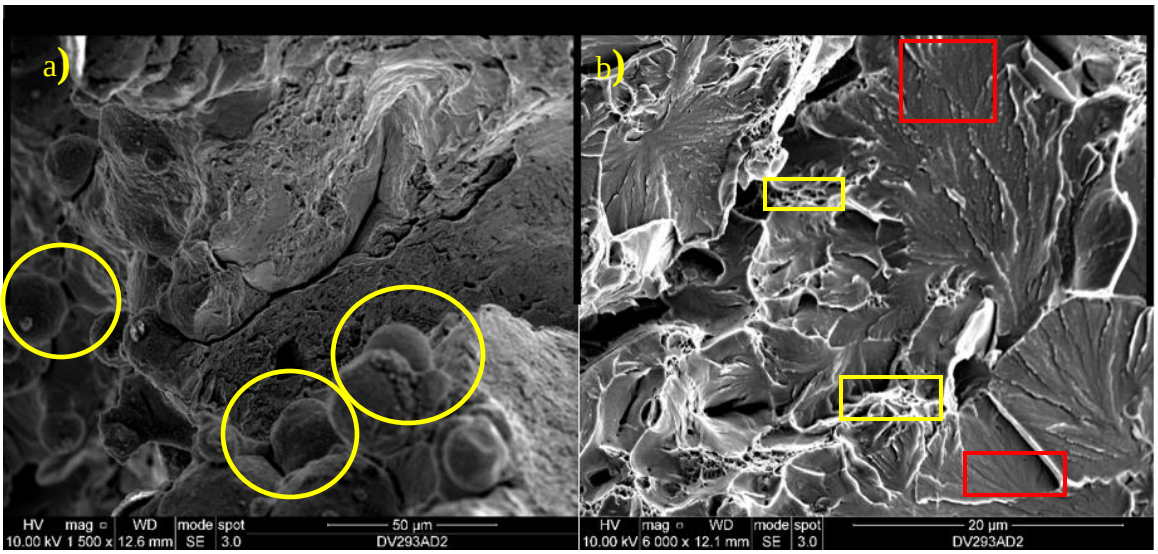

Figure 5.13. Balling, indicative of AM processing (a), and revealed AMAD microstructure (b).

5.2.3. AM Normalized Fracture Surface

The AMN specimen has limited elongation. The small rection is area is in agreement with low ductility of the specimen observed in tensile testing. The fracture surface face appears cleaved, though and at high magnification, the transgranular dimples are visible. This is neither highly brittle, nor highly ductile fracture.

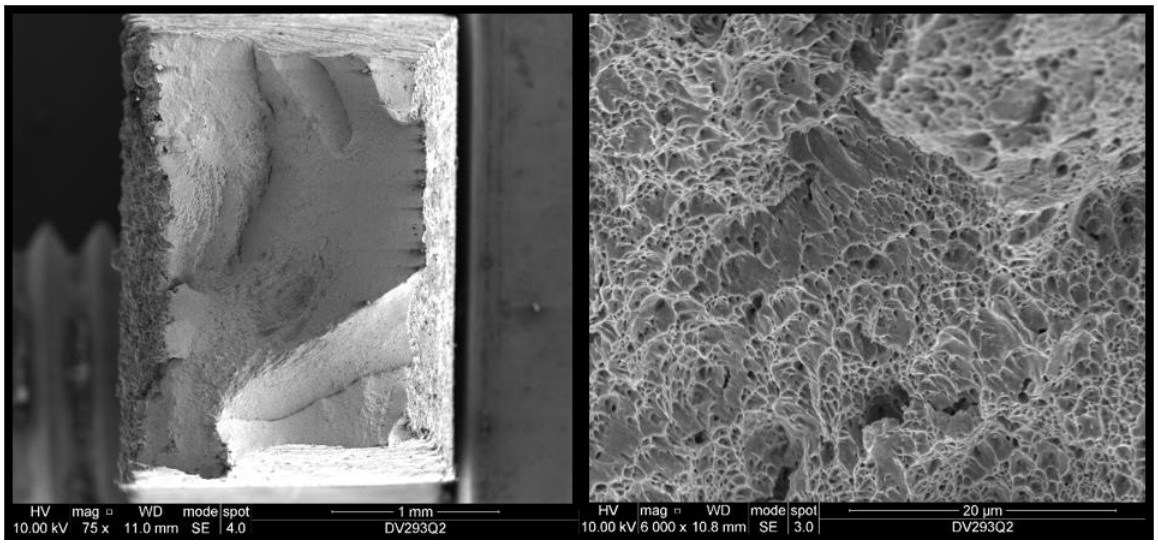

Figure 5.14. AM normalized specimen fracture surface at low and high magnification.

5.2.4. AM Normalized and Tempered Fracture Surface

Finally, the AM normalized and tempered (AMNT) specimen's fracture surface was analyzed. Like the WRNT specimen, the AMNT material exhibited significant deformation in the form of necking down and decreasing its cross sectional area. Additionally, its fracture surface at high magnification showed the familiar transgranular fracture behavior of a ductile break, and resembled the wrought material quite closely.

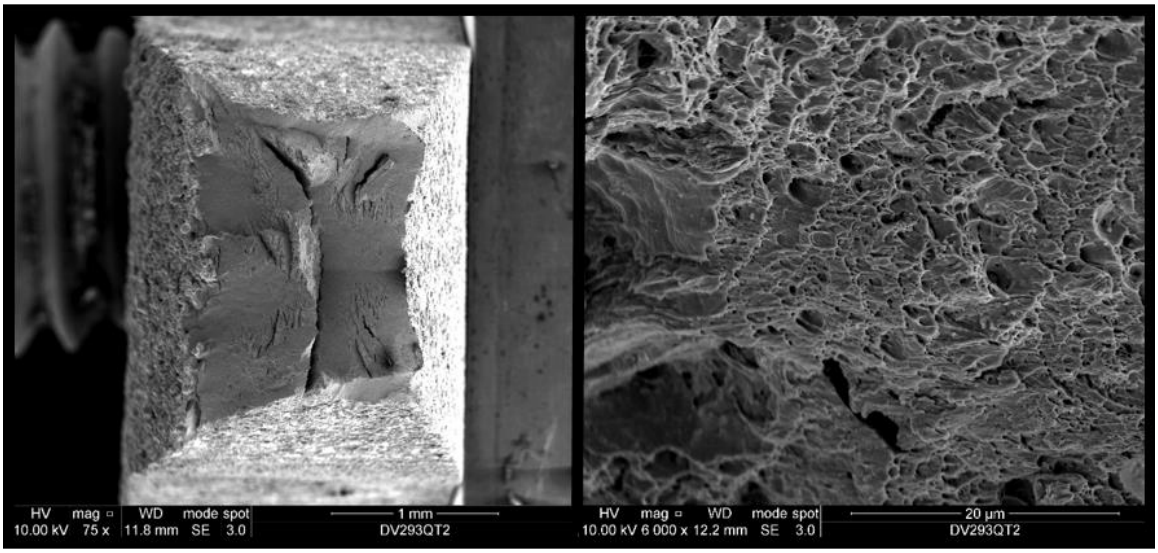

Figure 5.15. Low and High Magnification of AMNT Specimen, showing ductile elongation (a) and dimpled, transgranular ductile fracture behavior (b).

In summary, this investigation has shown that while the As-deposited material has an unpredictable and heterogeneous microstructure, it was more ductile than expected for non heat treated FM steel. The AM Grade 91 material subjected to the heat treatments has been shown to:

i) Produce a uniform microstructure though normalization, thereby removing the as-deposited heterogeneous microstructure produced during AM

ii) Become more ductile with tempering at (760 °C)

iii) Exhibit similar fracture mechanics and fracture surface features to wrought (base case) material

5.3. Summary of Microstructural Characterization Findings

Once appropriate surface finishes were achieved, the EBSD and optical microscopy techniques were successfully carried out to characterize the microstructure of AM Grade 91 steel for the first time. Subsequently, X-ray diffraction was used to identify and quantify crystallographic features and phase fractions in each of the specimens, by fabrication type and heat treatment. And finally, SEM fractography was performed on the broken tensile specimen' fracture surfaces to analyze the failure behavior of four room-temperature tensile specimens. In summary, by carrying out a range of tests to characterize the Grade 91 specimens, the following was discovered:

i) The DMLS process produces irregular steel microstructures that manifest as fine-grain regions and course, featureless regions, with appreciable internal stresses, that in some ways resemble the miscrostructure welds.

ii) Normalizing the AM material at 1040 °C for 30 minutes produces a fine austenite grain structure (<1 μm average grain size, which, when tempered, creates a homogenous microstructure and precipitates carbides from solution

iii) Direct tempering (760 °C for 45 minutes) of As-deposited material tends to cause it to precipitate carbides, but retain its basic heterogeneous structure.

iv) XRD revealed that all As-deposited samples of both AM types contain ferrite, austenite, and martensite phases. This is due to the irregular heating patterns experienced during fabrication.

v) Tempering of specimens (both post normalization and direct) removed all or most of the retained austenite phase, and caused precipitation of carbides.

vi) Though exhibiting a finer grain structure, AMNT material was very similar to WRNT (base case) material, revealing through XRD that their fraction of BCC, FCC, and $M_{23}C_6$ constituent phases were within 1% of one another other.

vii) Martensite (BCT) fraction was ~15% - 19% in all pre-tempered specimens, and normalization did not have a strong effect on observed martensite fraction.

viii) All three heat treated specimens exhibited the "dimples" indicative of ductile fracture along the faces of their fracture surfaces, though only the tempered specimens experienced significant reduction area (elongation).

ix) No gross defects or large voids were seen in any AM specimens.

x) "Balling" often due to oxygen contamination, was observed on the surfaces of all AM specimens, regardless of heat treatment. While this is typical of AM of metals, it suggests additional post-processing/surface finishing of AM metals would be necessary for engineering applications.

6. Results of Mechanical Properties Testing of Grade 91 Steel

In this experiment, various heat-treated specimens of both wrought and DMLS material were fabricated, machined, measured, and subjected to controlled strain-rate tensile tests to determine strength, ductility, and instantaneous stress-strain behaviors, as well as to analyze creep and other thermomechanical deformation phenomena. Grade 91 steel has been subjected to a rigorous and wide-ranging mechanical testing to establish and approve an ASME Code Case for its use in industry. As an exception to established code for "traditional" steels, the Grade 91 Code Case prescribes not only composition and performance specifications, but fabrication methods and heat treatments.

In industry, wrought Grade 91 bars and rods are fabricated using melt furnaces and continuous casting systems to produce solid bars or rods, and then hot worked to produce pipes (P91) or pierced and drawn to form tubes (T91). Heat treatments are done at this stage in the fabrication process, after which final dimensions are achieved through mechanical means (grinding, milling, boring, etc) to ASTM end use specifications. The DMLS production of Grade 91 material used in this experiment was directly sintered into form, layer by layer, with each subsequent layer re-heating the previous, and causing an irregular cycle or heating, cooling and reheating of adjacent material layers. For this reason, AM Grade 91 material would not fall under the code case as written.

By measuring the mechanical properties of both wrought and AM Grade 91 steel, the effects of DMLS fabrication on mechanical performance was directly compared to that of industry standard wrought Grade 91 steel.

6.1. Room Temperature Strength Analysis of Grade 91 Steels

As part of the code qualification process, tensile testing is carried out on thousands of specimens over an extended period of time. This investigation is focused not on generating or refining mechanical data for qualification, but instead on establishing an initial data set on AM Grade 91 steel and using it for quantitative comparison with code (wrought) material. Room temperature testing was carried out on two tensile specimens of each fabrication and heat treatment type to assess repeatability of specimen fabrication. No significant dissimilar results were found; in all fabrication and heat treatment types, the force, gauge length, width, thickness, and displacement data were measured, and had very little variability. So, between the two specimens of each steel, one was chosen at random to be representative of that specimen type. Since Grade 91 Steel described in ASME code is considered to be appropriate for boiler and pressure vessel use after normalization and tempering, that specimen type (WRNT) is considered the base case in this investigation

Specimen	Fabrication	Post-fab Heat Treatment	Temp	$\dot{\varepsilon}$ [s^{-1}]
WRN1	Wrought	Normalized	20º C	10^{-3}
WRN2	Wrought	Normalized	20º C	10^{-3}
WRNT1	Wrought	Normalized & Tempered	20º C	10^{-3}
WRNT2	Wrought	Normalized & Tempered	20º C	10^{-3}
AMAD1	DMLS	none (as-deposited)	20º C	10^{-3}
AMAD2	DMLS	none (as-deposited)	20º C	10^{-3}
AMN1	DMLS	Normalized	20º C	10^{-3}
AMN2	DMLS	Normalized	20º C	10^{-3}
AMT1	DMLS	Tempered (direct)	20º C	10^{-3}
AMT2	DMLS	Tempered (direct)	20º C	10^{-3}
AMNT1	DMLS	Normalized and Tempered	20º C	10^{-3}
AMNT2	DMLS	Normalized and Tempered	20º C	10^{-3}

Table 6.1. Room Temperature Tensile Specimens

In all cases, the testing fixture successfully gripped and engaged the sample, and following an initial loading region, exhibited linear elastic behavior followed by plastic deformation, a maximum (ultimate) tensile strength, and a region of non-uniform elongation leading to eventual fracture.

6.1.1. Comparisons of Room Temperature Steel Specimens

The first comparison was between normalized (non-tempered) specimens of wrought and AM material (Figure 6.1). Both the WRN and AMN material exhibit extremely high strength. However, the AM material has a significantly lower elongation (strain to failure) than the wrought Grade 91 material, meaning it has relatively low ductility in comparison. This high-strength, low ductility is expected, as the normalization

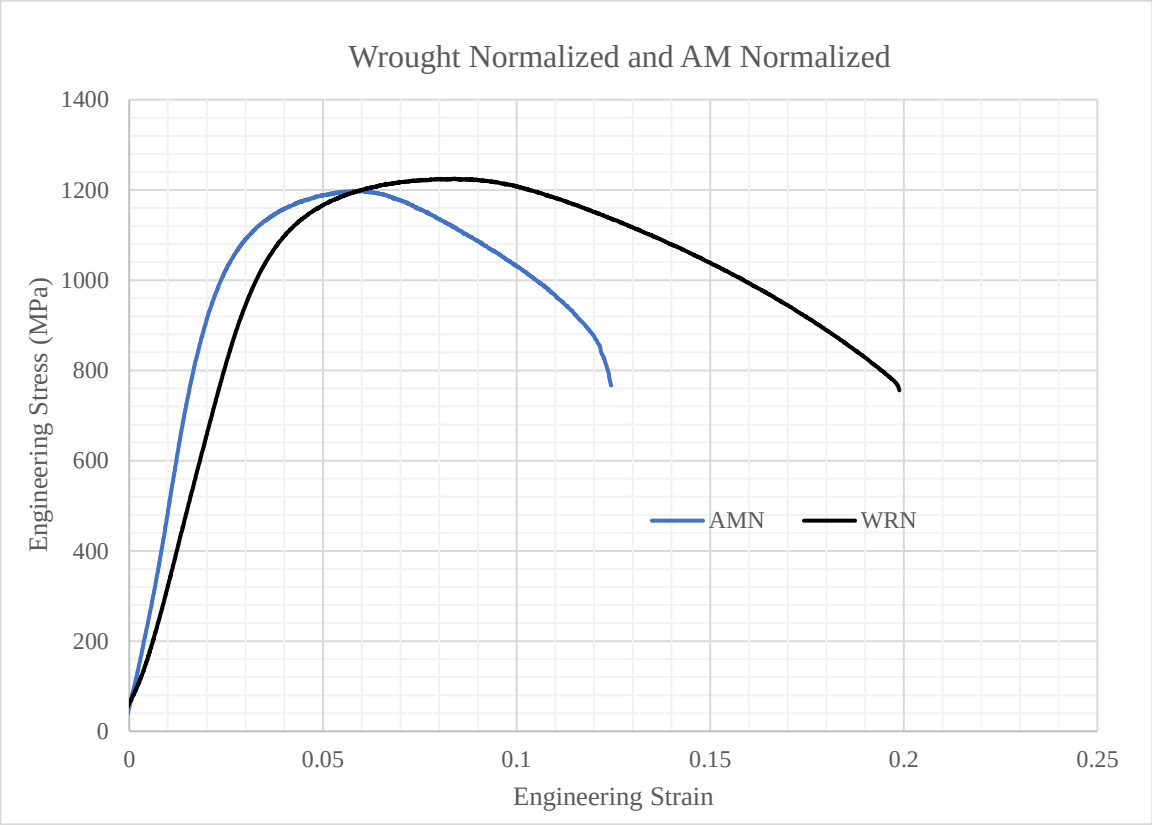

Figure 6.1. Stress-strain curves for normalized wrought and AM specimens.

process provides uniformity to grain size and composition, while the quenching process produces the martensite transformation and associated solution strengthening, resulting in a harder and stronger steel. Both of the normalized DMLS specimens exhibited this low elongation behavior, and as such, are not likely to be well suited to applications for which ductility or significant strain hardening is required. Additionally, as was discussed in Chapter 2, radiation damage in such steels would tend to increase the hardness and decrease ductility further still. However, it is worth noting that the AMN material did respond to normalization as expected, with a marked increase in hardness.

The next specimens of DMLS material and wrought material were both normalized tempered, and tested to failure (Figure 6.2). Following these heat treatments, it is clear that both specimens responded as expected to the post normalization tempering process. Both the AM and wrought material experienced a significant decrease in hardness and increase in ductility. This removal of hardness, however, was more pronounced in the wrought material than in the AM material, the latter of which had around 20% higher YS. This could be due to a number of factors, including the incomplete dissolution of precipitates, the effects of heterogeneity, and/or prior austenite grain size in the pre-heat treated material.

The YS of the AMNT and WRNT were 738 MPa and 610 MPa, respectively. According to the SEM characterization analysis in Chapter 5, the AMNT average grain size was smaller than the base case (WRNT), and thus according to the Hall-Petch relation, this should result in greater yield strength. Additional work beyond this dissertation should include a suite of varying tempering times and temperatures to remove additional hardness from AMNT material, making it more like the ASME code material.

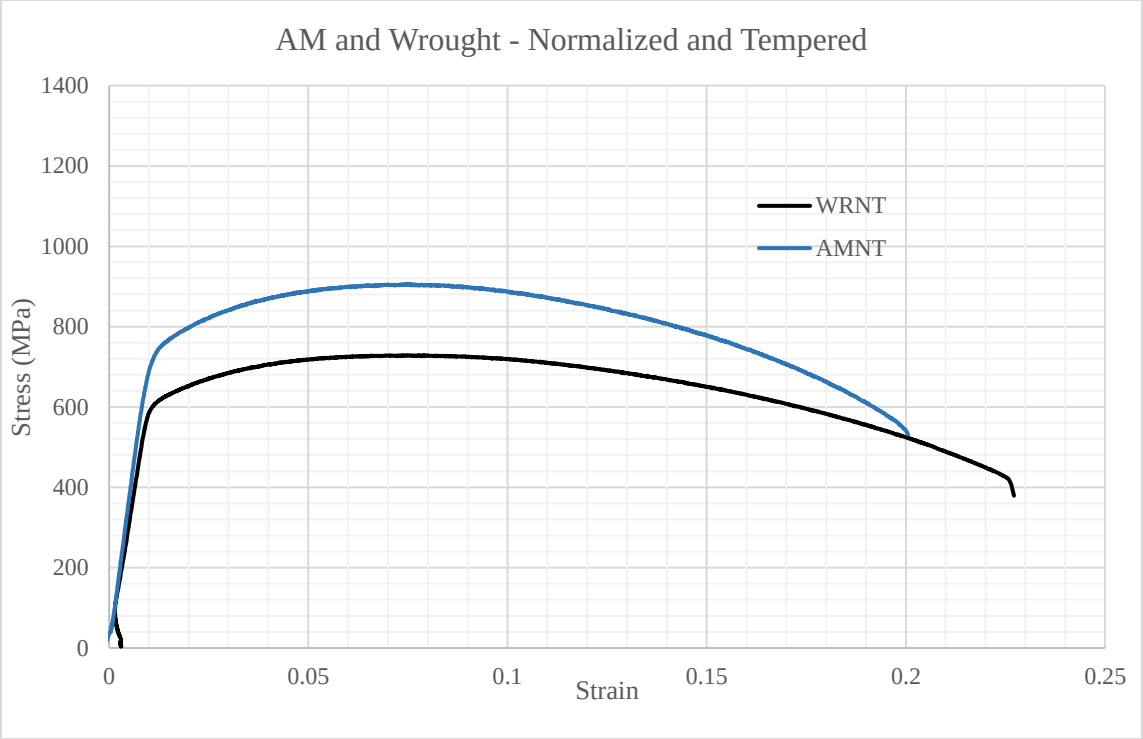

Figure 6.2. Normalized and Tempered material (Wrought and AM)

It is also unknown to what extent the AMAD material would be homogenous throughout the build. The AMAD tensile samples were produced from bottom of the build (adjacent to the build plate). It is possible that local heating and cooling effects during fabrication could cause a variation in the microstructure, such as localized increases in the density of carbides ($M_{23}C_6$) and other precipitates (MX).

This result, combined with the microstructural analysis revealing a uniform microstructure of the DMLS Normalized/Tempered material, indicate that normalizing and tempering heat treatments produced a Grade 91 steel with both a uniform microstructure, with strength and ductility comparable to wrought material. While there is currently no guidance on AM material in the Grade 91 ASME Code Case, this investigation has demonstrated that unirradiated Grade 91 steel fabricated by DMLS reacts similarly to

wrought material, though the post normalization tempering effects are less pronounced in the AM material.

The untreated, As-deposited material (AMAD) was also tested, in order to evaluate its mechanical behavior directly after a build. As indicated in Chapter 5, the AMAD material had very heterogeneous microstructure and relatively high martensite fraction. Conventional thinking would be that the heterogeneous structure and martensite content of the AMAD material would produce a hard, brittle material. However, upon generation of the stress-strain curve, AMAD was shown to be not only strong, but much more ductile than expected (>17% TE), as shown in (Figure 6.3).

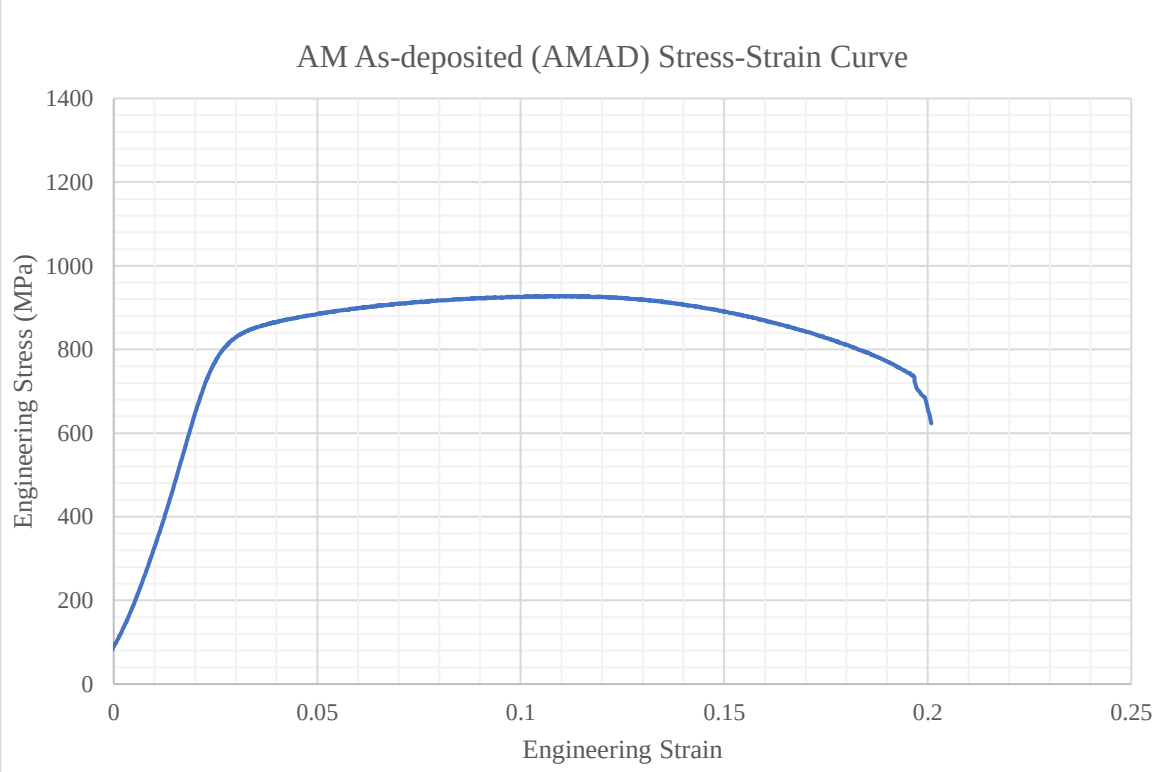

Figure 6.3. AMAD stress strain curve, showing >17% elongation.

For the final room temperature tensile test, direct-tempered material was tested. The expectation was that tempering would soften the As-deposited material and that it would become more ductile. This tempering effect was indeed observed, and the AMT material was above the ASME minimum in both strength and ductility.

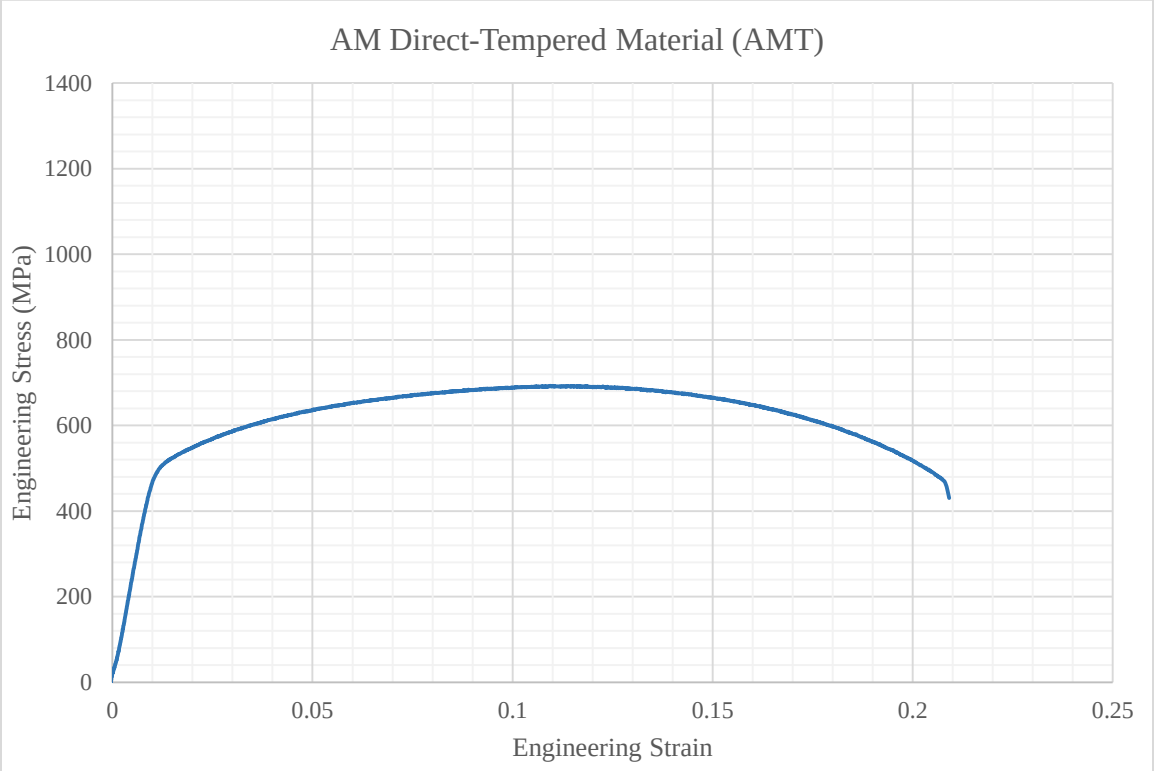

Figure 6.4. Direct tempered (AMT) stress-strain curve.

When plotting all DMLS specimens together, the effects of normalization and tempering are evident in the mechanical performance of each specimen. While it is expected that the As-deposited specimen would exhibit elevated strength and hardness in its normalized condition, as well as more ductility in its normalized/tempered and direct tempered state, this experiment observed that it also exhibited an unexpected degree of ductility in its As-deposited condition. This was true for both of the tested tensile specimens (AMAD1 and AMAD2).

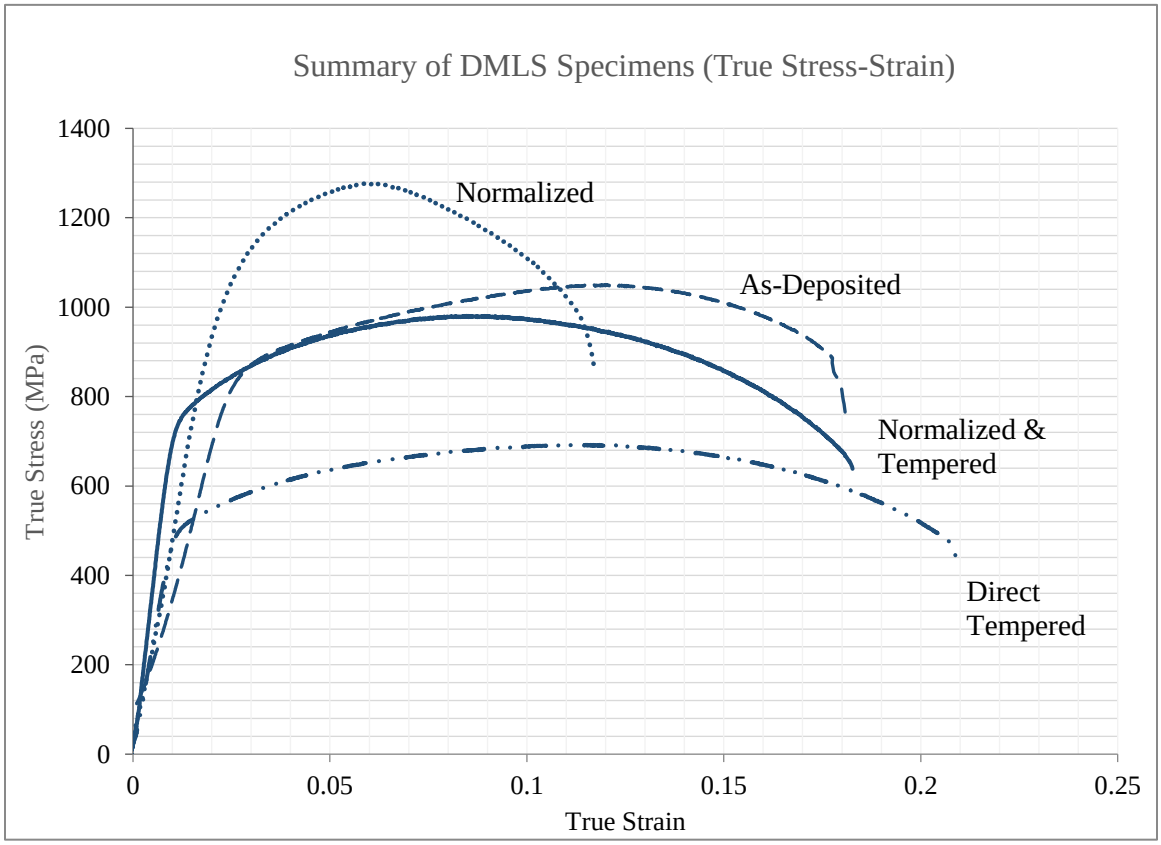

Figure 6.5. Stress-strain curves of all AM specimens, plotted for comparison.

6.1.2. Summary of Room-Temperature Strength and Performance

In general, all normalized specimens showed increased hardness and strength, with a noticeably reduced elongation. DMLS material became weaker and more ductile after being directly tempered, and specimens that were both normalized and tempered showed the combined high strength and ductile behavior desired in Grade 91 steel. The As-deposited material, which was known to have a high degree of disorder, showed high strength, but also higher elongation than expected. Further quantitative analysis of the strain hardening regions of each tensile sample are discussed in Chapter 6.4.

Table 6.2. Strength and elongation summary of room temperature specimens.

Specimen	HT	YS (MPa)	UTS (MPa)	UE (%)	TE (%)
WRN	N	984	1225	5.7	17.2
WRNT	N&T	610	729	6.6	22.1
AMN	N	936	1198	4.3	10.7
AMNT	N&T	738	905	6.7	19.2
AMT	T	501	631	8.7	22.1
AMAD	none	800	928	8.7	17.7

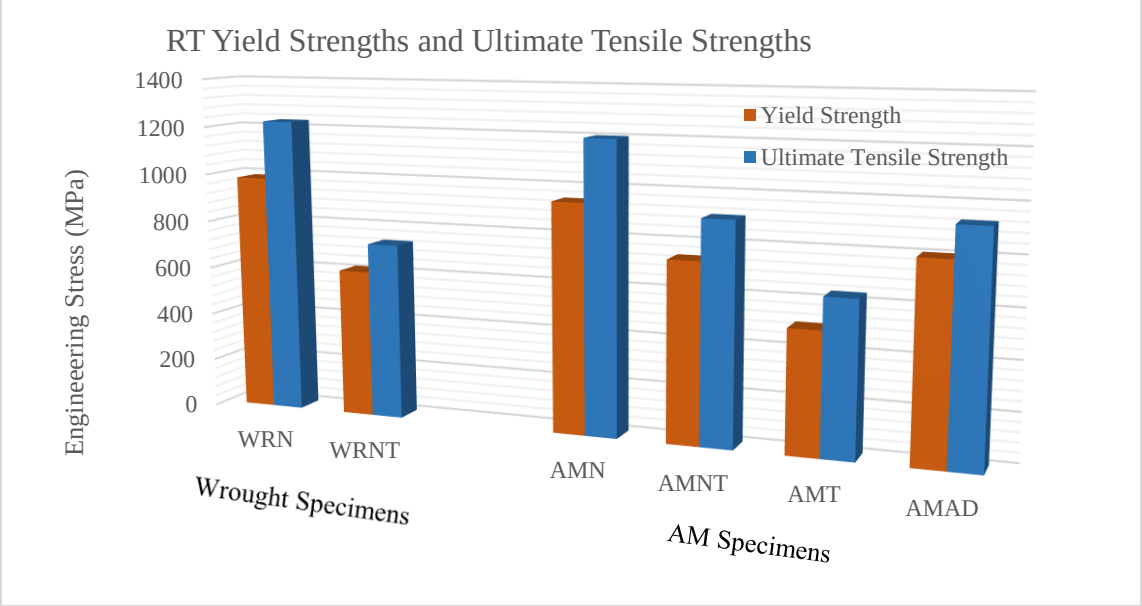

Figure 6.6. Summary of RT Yield Strength and Ultimate Tensile Strengths.

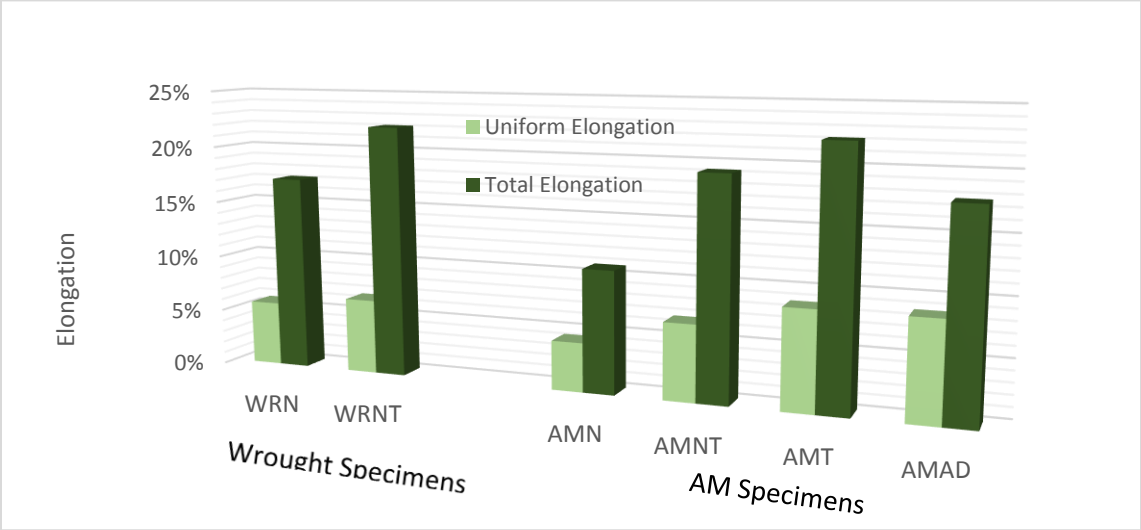

Figure 6.7. Uniform and total elongation for all room temperature specimens.

6.2. Elevated Temperature Stress-Strain Analyses for Grade 91 Steels

Fast spectrum systems generally operate at coolant temperatures between 300 ºC and 600 ºC. For this reason, evaluating the mechanical properties of AM Grade 91 steels in this range will reveal how unirradiated DMLS material will perform under service conditions in the lower to upper coolant temperature regions of most advanced fast reactor designs. Based on the results from room temperature testing, the normalized and tempered specimens of both DMLS and wrought material showed the most desirable combination of strength and ductility. For this reason, they were chosen for further analysis at 300 ºC and 600 ºC. Additionally, As-Deposited material was tested at both elevated temperatures for comparison, and to quantify the effects of heat treatments in these conditions.

6.2.1. 300 ºC Strength Analyses of Grade 91 Steel

In designing fast spectrum systems, 300 ºC is a common benchmark representing the low end of the temperature profile. After The AMNT and WRNT specimens were tested to failure, and their performance directly compared to one another (Figure 6.8). The observed slopes of the linear elastic regions, and strain hardening regions were observed to be nearly identical in both shape and magnitude. Though the AMNT material was observed to be harder and less ductile at room temperature, upon heating to 300 ºC, their strength became nearly indistinguishable. Both specimens exhibited a YS around 520 MPa, which corresponds to about 15% and 20% strength reductions for WRNT and AMNT, respectively.

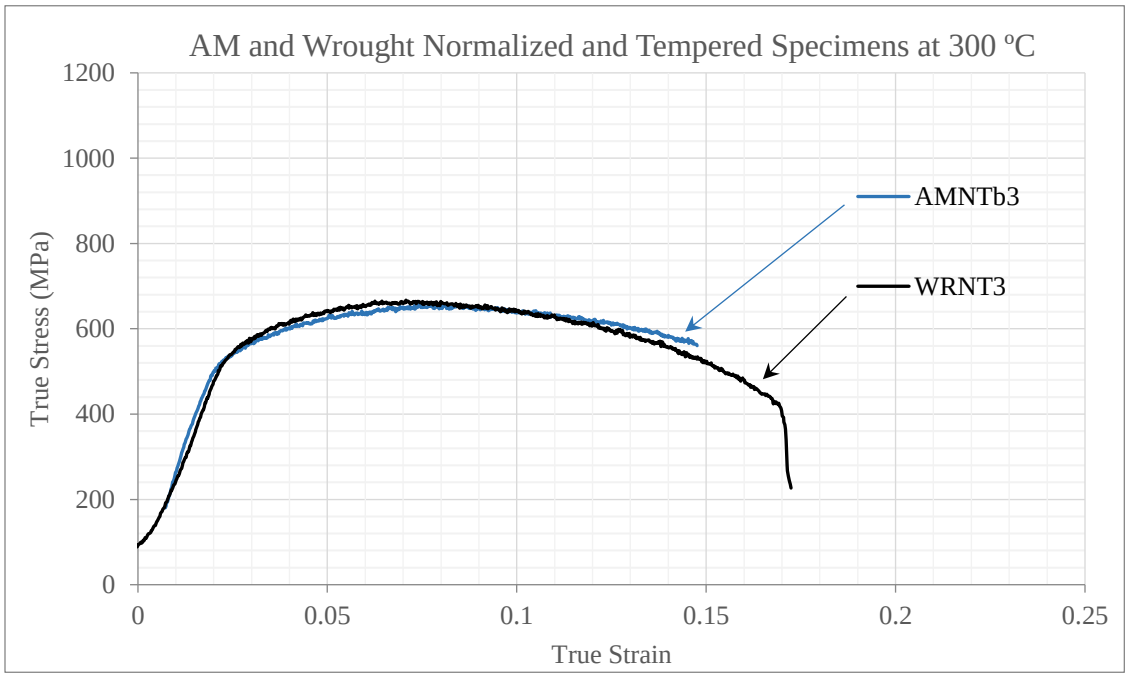

Figure 6.8. WRNT and AMNT, showing similar strength and elongation.

Following the testing of NT material, an As-deposited specimen (AMAD3) was loaded and tested to failure at 300 ºC for comparison. When compared to the previous (normalized/tempered) specimens, it exhibited an extreme high-strength behavior, as well as elongation comparable to both of the normalized and tempered specimens (Figure 6.9). Remarkably, the AMAD specimen exhibited no decrease in strength between room temperature and 300 ºC.

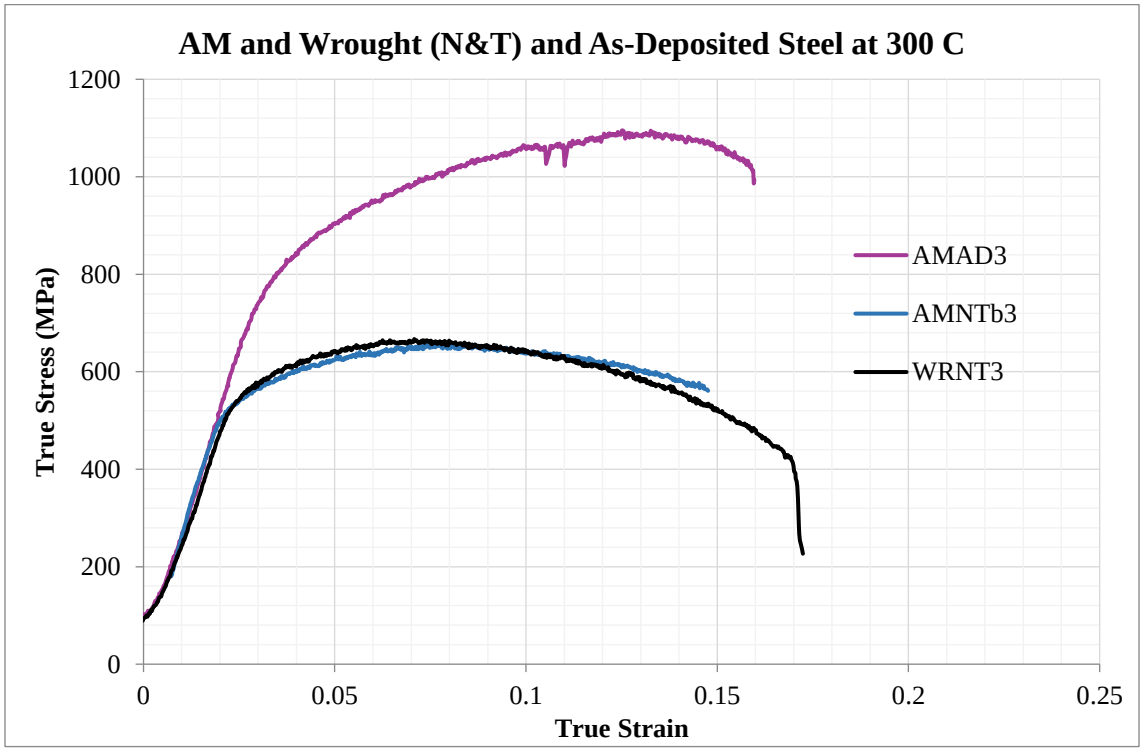

Figure 6.9. All three tensile specimens at 300 °C

Because specimen AMAD3 exhibited such highly unanticipated strength, an additional 300 ºC test (specimen AMAD4), was carried out several months later, and the same extreme strength was observed (Figure 6.9). The observation of this strengthening, suggests that the DMLS fabrication method itself has resulted in a highly heterogeneous and complex microstructure that does not present itself in traditional (wrought) fabrication. As was shown in Chapter 5, the AMAD microscopy reveals a high disordered

microstructure that contains featureless regions, as well as both coarse grain and fine grain constituents. Additionally, normalizing and tempering wrought material typically process produces ~1.5 wt% precipitate [23], of which 85% - 90% is coarse carbide precipitates ($M_{23}C_6$), and the remainder is MX precipitates. The concentration of precipitates in As-deposited material is not known; nor is the temperature-dependent precipitation concentration as the sample is heated.

As previously discussed, precipitation hardening is an important factor in Grade 91 steel, and temperature cycling during fabrication could cause precipitates (metal carbides and nitrides) to come in and out of solution as elements of the DMLS build are re-heated and cooled through the intercritical temperature band with subsequent laser passes. It is also possible that the As-deposited specimen's microstructure is such that heating to elevated temperatures during testing causes additional precipitation. It is possible that heat cycling during or post fabrication is resulting in an increased accumulation of precipitates is unclear, and additional investigation and characterization of this unforeseen extreme strengthening while maintaining good ductility is warranted.

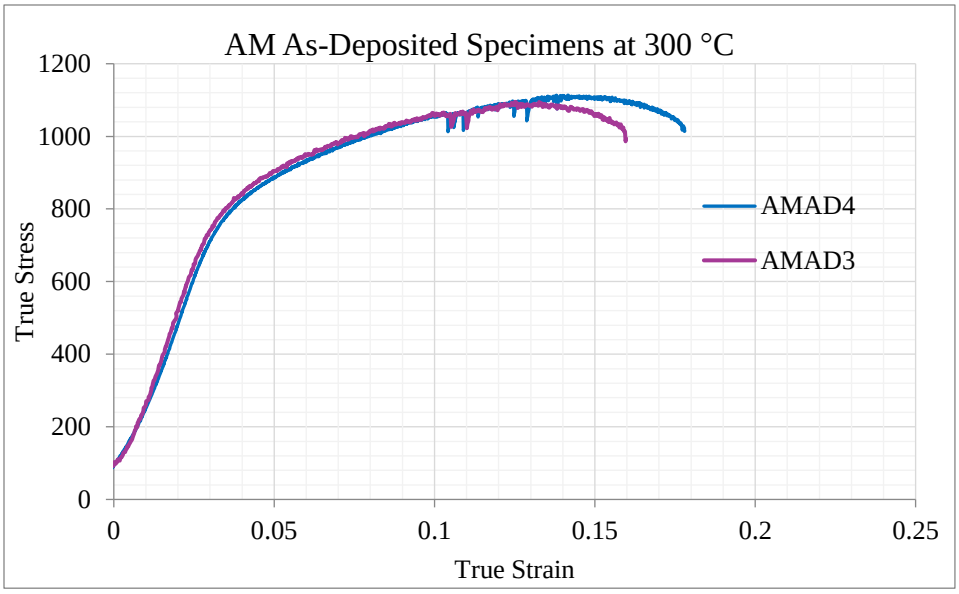

Figure 6.10. Tensile results of two AMAD Specimens, showing good reproducibility of results.

Specimen	HT	YS (MPa)	UTS	UE (%)	TE (%)
WRNT	NT	524	620	4.4	16.4%
AMNT	NT	520	614	4.7	15.7%
AMAD	none	708	943	10.8	14.5%

Table 6.3. 300 °C Tensile strength and ductility summary.

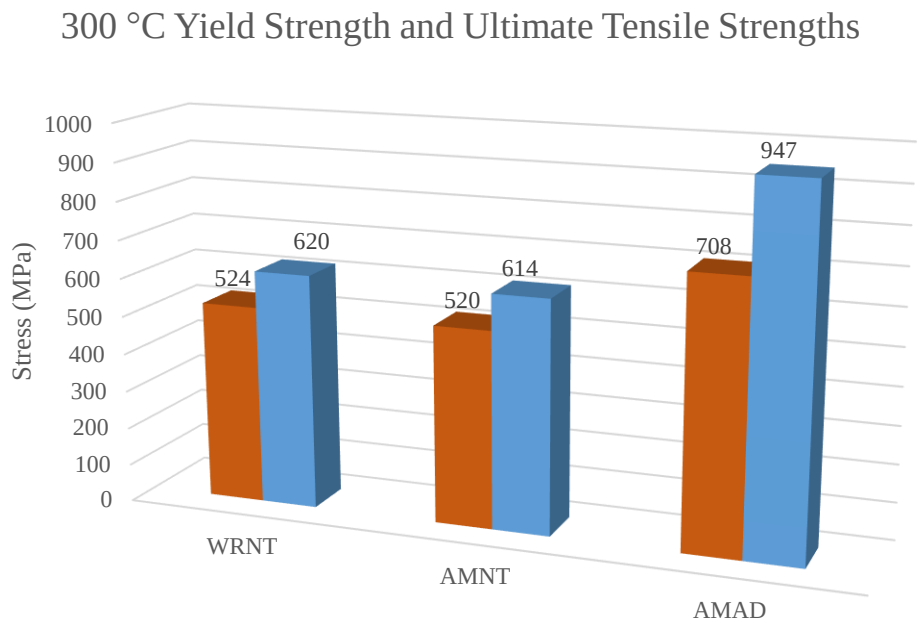

Figure 6.11. YS and UTS for 300 °C specimens.

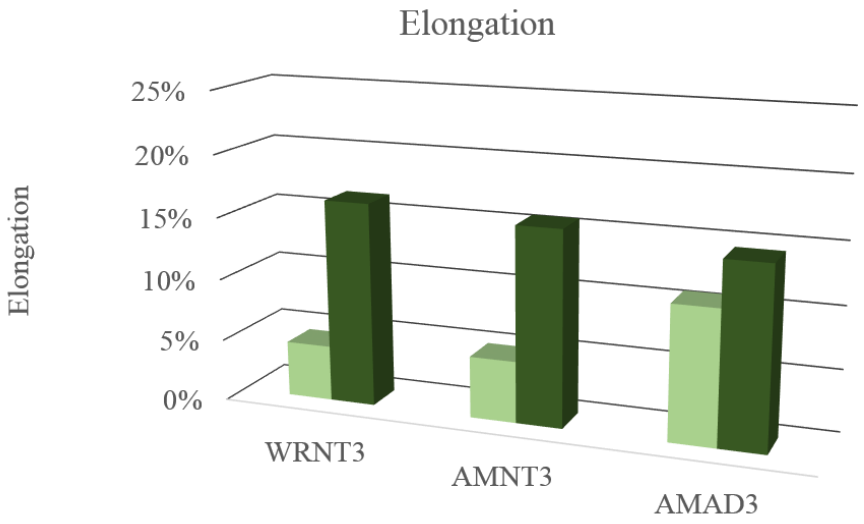

Figure 6.12. Uniform and total elongation for 300 °C specimens.

6.2.2. 600 ºC Strength Analyses of Grade 91 Steel

To protect the specimens against oxidation, all 600 ºC tensile tests were performed in the sealed vacuum furnace as described in Chapter 4. As with the 300 ºC tests, the primary objective of the 600 ºC tensile testing was to assess whether DMLS material can be heat treated to perform similarly to wrought material. The stress-strain curve results of both heat treated specimens were plotted in Figure 6.13.

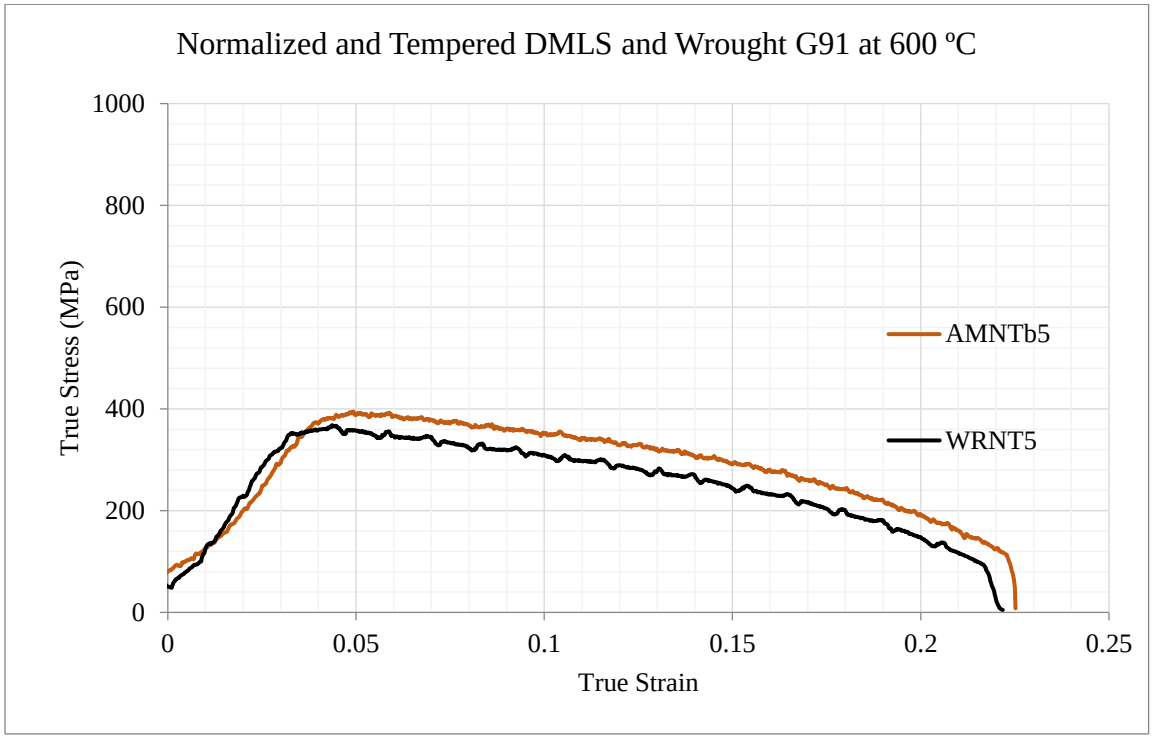

Figure 6.13. AMNT and WRNT specimens testes at 600 °C.

Much like the 300 ºC results, at 600 ºC, the linear elastic region is evident, and the DMLS and wrought material show almost identical shape and amplitude. With increasing temperature, the strain hardening region is significantly diminished, and the YS and UTS

tend to occur close to one another. This result successfully demonstrated that at 600 ºC, the mechanical response of DMLS and wrought material are very similar in terms of strength and ductility.

Because of the compelling extreme strength findings at 300 ºC, additional testing of As-deposited material was carried out at 600 ºC. Again, unexpectedly, the As-deposited material demonstrated extreme strength at 600 ºC (Figure 6.14). In addition, a pronounced strain hardening region (around 5% plastic strain) is visible. Its proportionality constant and strain hardening exponent are calculated in the following subchapter.

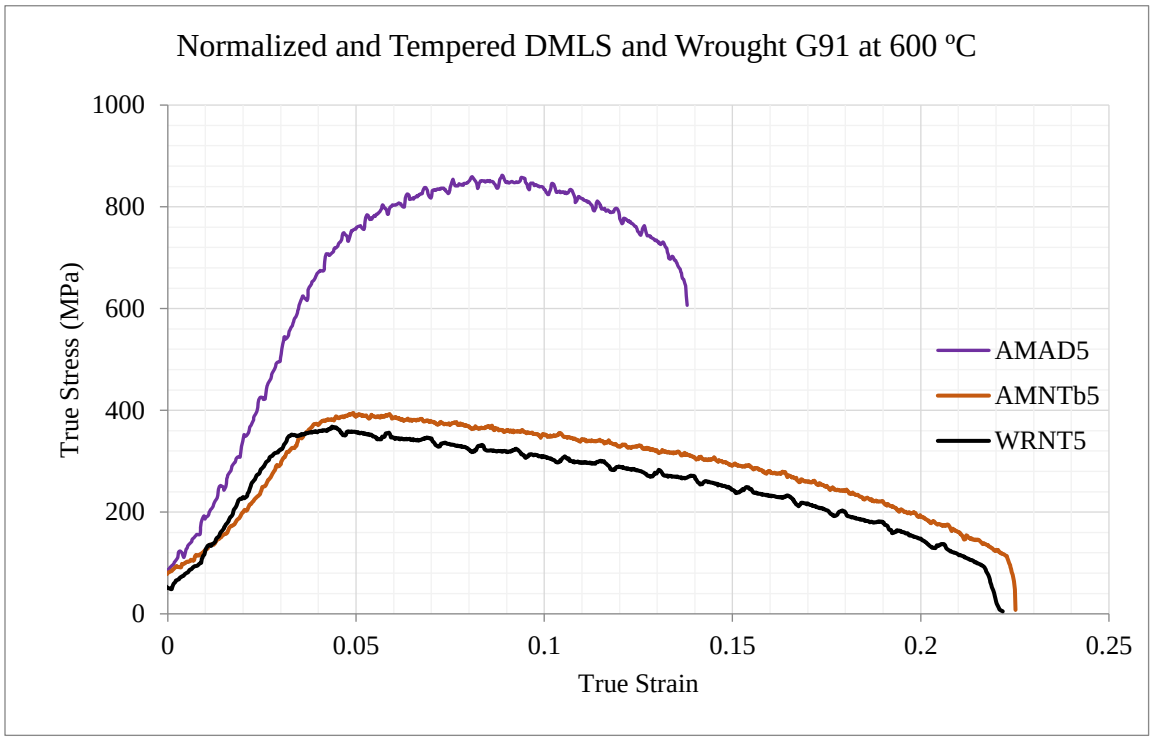

Figure 6.14. All three specimens tested at 600 ºC.

Having observed this extreme strengthening at 600 ºC and in both As-Deposited specimens tested 300 ºC, a fourth elevated temperature tensile test was carried out on one of the final remaining unused wedge type (large) tensile specimens (AMAD6), with

approximately four times the cross section area and 2.5 times gauge length. Aside from showing a slightly different compliance region slope (which is expected), the AMAD6 and AMAD5 samples are nearly exactly the same in magnitude and curve shape, indicating that in the course of this investigation, an ultra-strength, hardened allotrope of Grade 91 steel has been discovered.

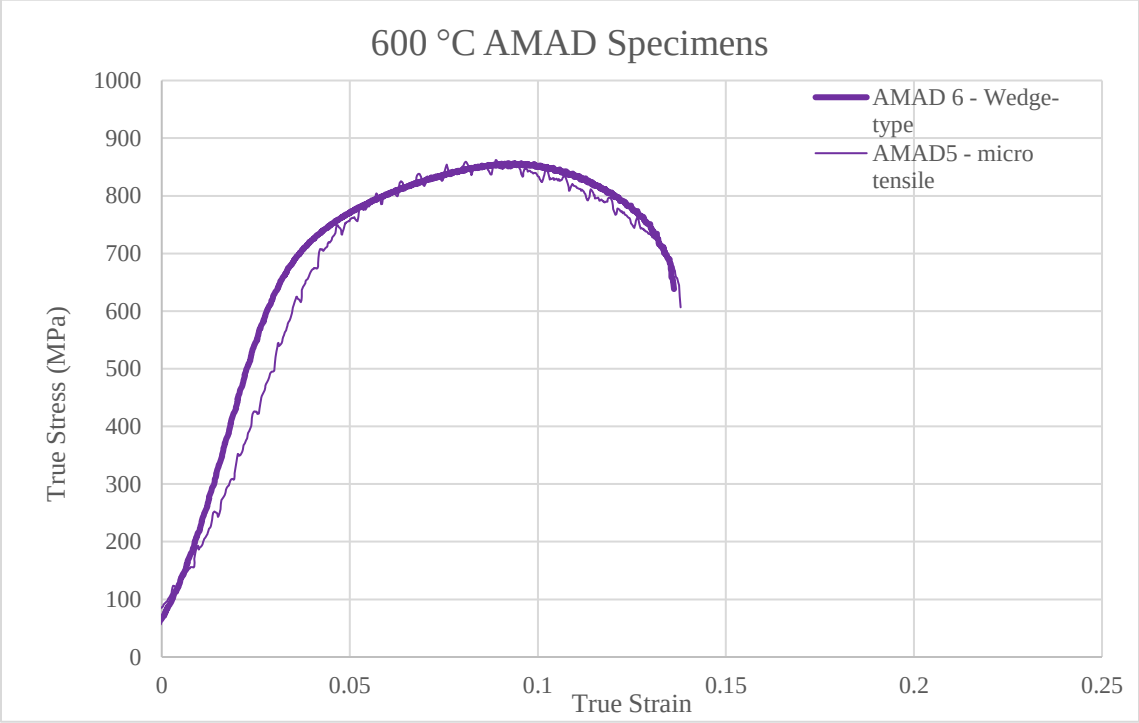

Figure 6.15. Stress-strain curves of both wedge type and microtensile specimens of AMAD material at 600 °C.

A summary of the 600 °C tensile results are given below (Table 6.4), and plotted on Figures 6.16 and 6.17.

Specimen	HT	YS (MPa)	UTS (MPa)	UE (%)	TE (%)
WRNT5	NT	352	361	1.5	21.8
AMNT5	NT	351	363	1.3	21.9
AMAD6	none	616	775	4.9	11.9

Table 6.4. Summary of 600 °C tensile behavior

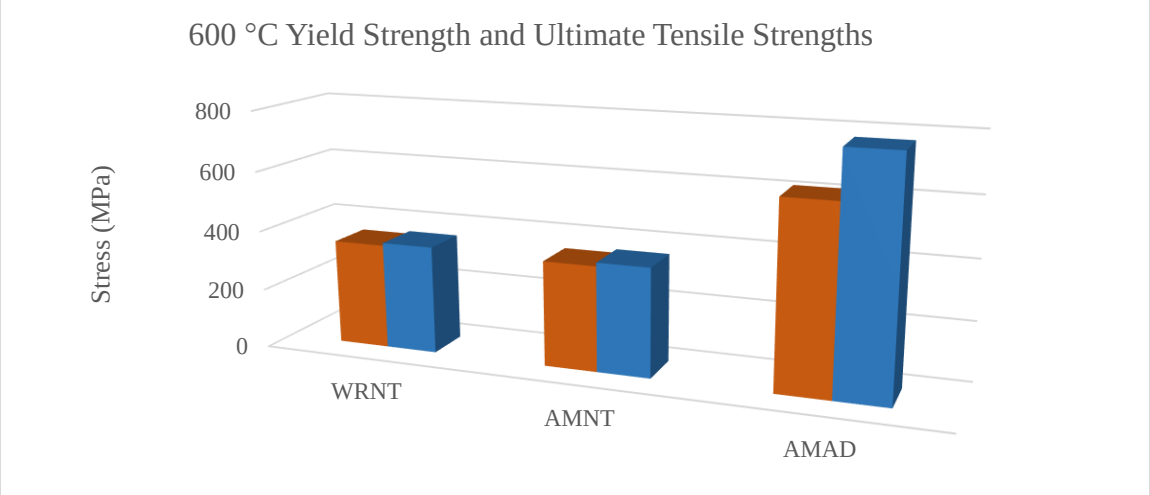

Figure 6.16. YS and UTS for 600 °C specimens.

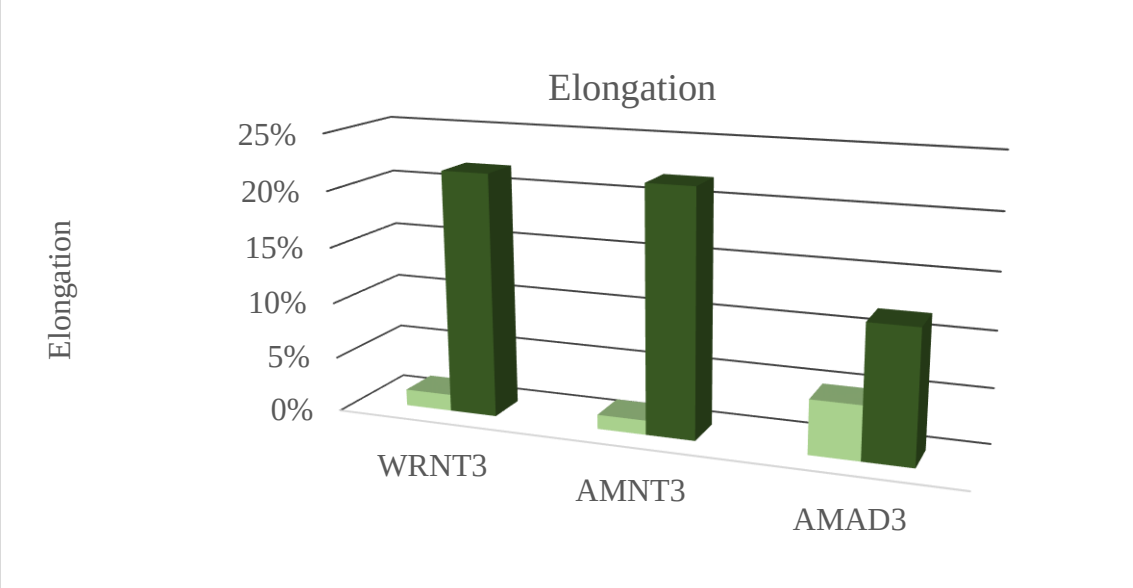

Figure 6.17. Uniform and total elongation for 600 °C specimens.

For comparison to commercial material, the YS of each the Grade 91 steel specimens tested at elevated temperature were compared to the ASME Code Case literature values for minimum YS versus temperature (Figure 6.18).

In comparing tensile specimens, it is apparent that the AMAD specimen had the highest yield strength. At room temperature, the AM normalized and tempered specimen had higher strength, but this variation disappeared at 300 °C and 600 °C, and their strengths and elongation were indistinguishable from on another at those temperatures.

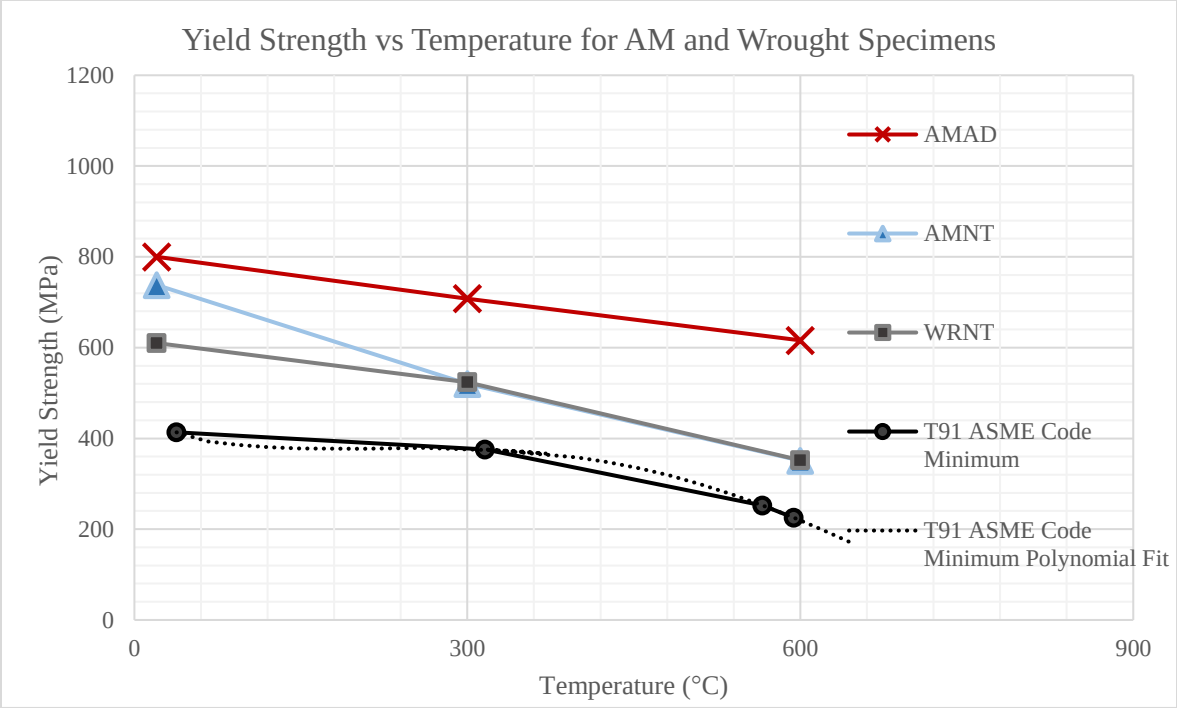

Figure 6.18. Yield Strength vs Temperature for all Elevated Temperature Specimens (this study), Compared to ASME Code Case Minimum Yield Strength Values.

6.3. Strain Hardening and Ductility Analysis of DMLS Grade 91 Steel

To understand and quantify the strain hardening behavior of AM and wrought samples, the Power Law approach was used to generate strain hardening exponents and proportionality constants for all specimens. The strain hardening region (or work hardening region) describes the ability of a material to resist further deformation and become strengthened as it undergoes plastic deformation, and is extremely important to the performance of an engineering material both under normal and abnormal operating conditions. Recalling Equation 4.2, the stress and strain relationship is in exponent form, and in this investigation, the domain of the strain hardening region is taken to be the strain region between the 0.2% offset strain (the yield point), and the maximum stress point (strain at UTS), represented by Region II in Figure 4.16:

$$\sigma = K\varepsilon^{n} \qquad \textbf{Equation 4.2}$$

The strain hardening coefficient (*K*) is proportional to the magnitude of the hardening of a ductile material, while the value of the strain hardening exponent (*n*), can be thought of as a measure of a material's ability to resist necking (non-uniform deformation).

It is evident that from exponential form of Equation 4.2 that on a semi-log strain plot, that the strain hardening region should appear linear. As a check of concept, each of the six room temperature stress-strain curves were plotted to verify the form of the strain hardening behavior.

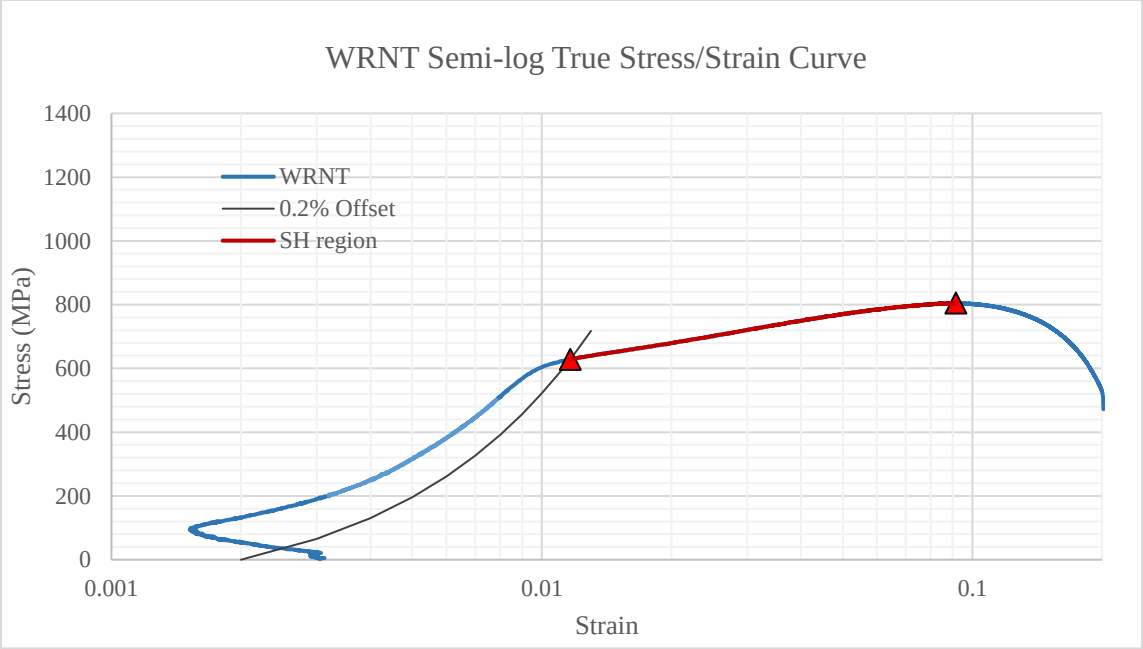

Figure 6.19. Semi-log plot of WRNT.

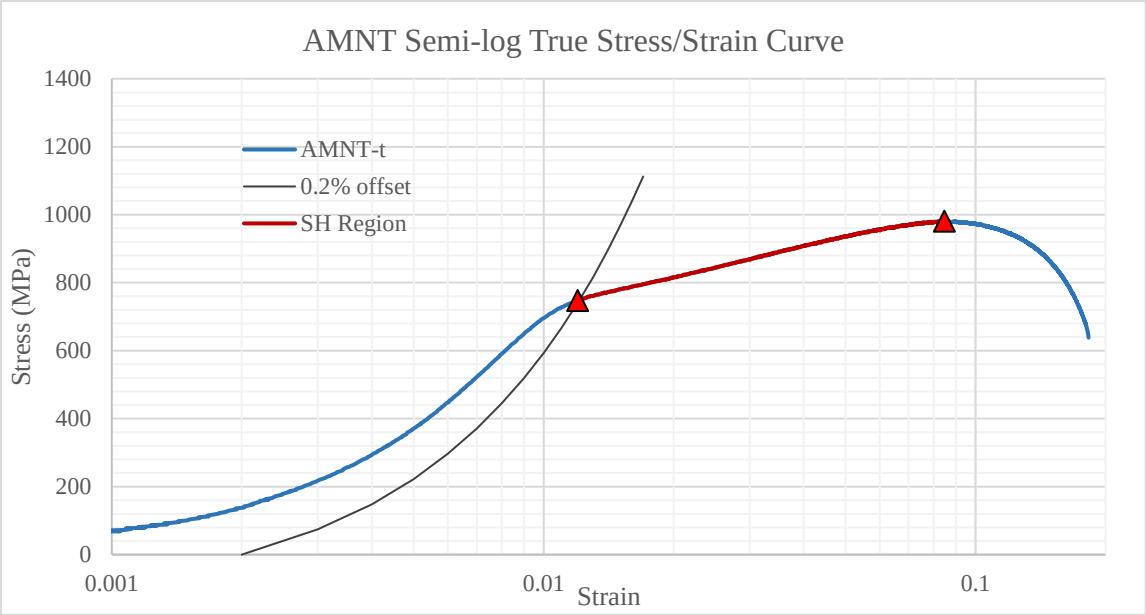

Figure 6.20. Semi-log plot of AMNT.

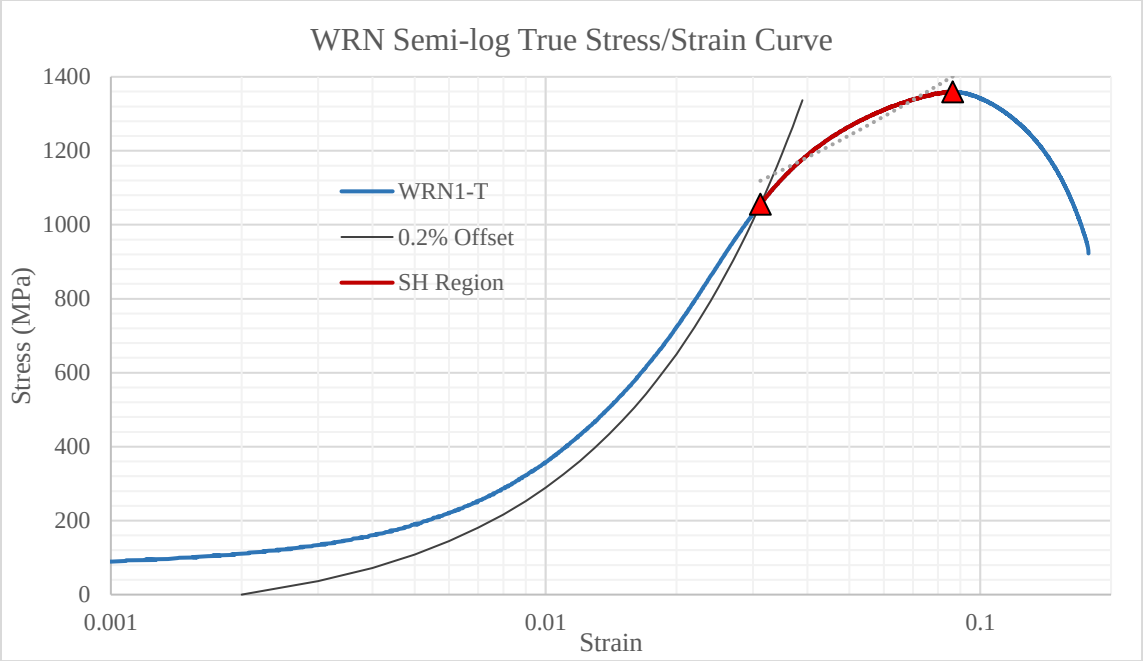

Figure 6.21 Semi-log plot of WRN.

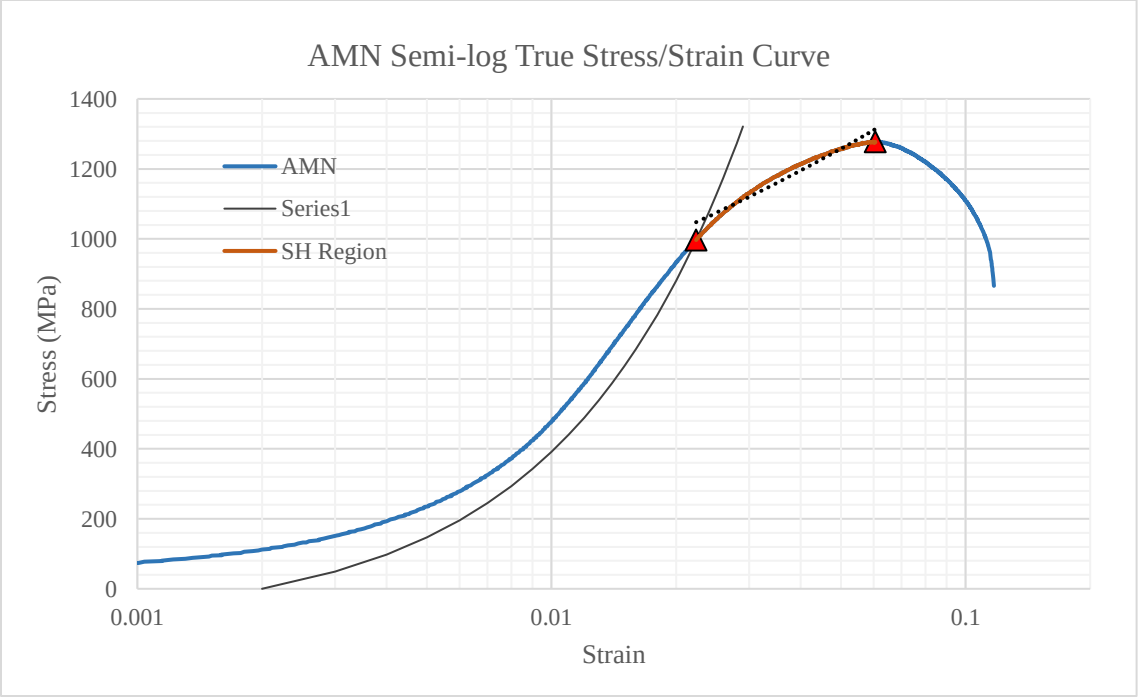

Figure 6.22. Semi-log plot of AMN.

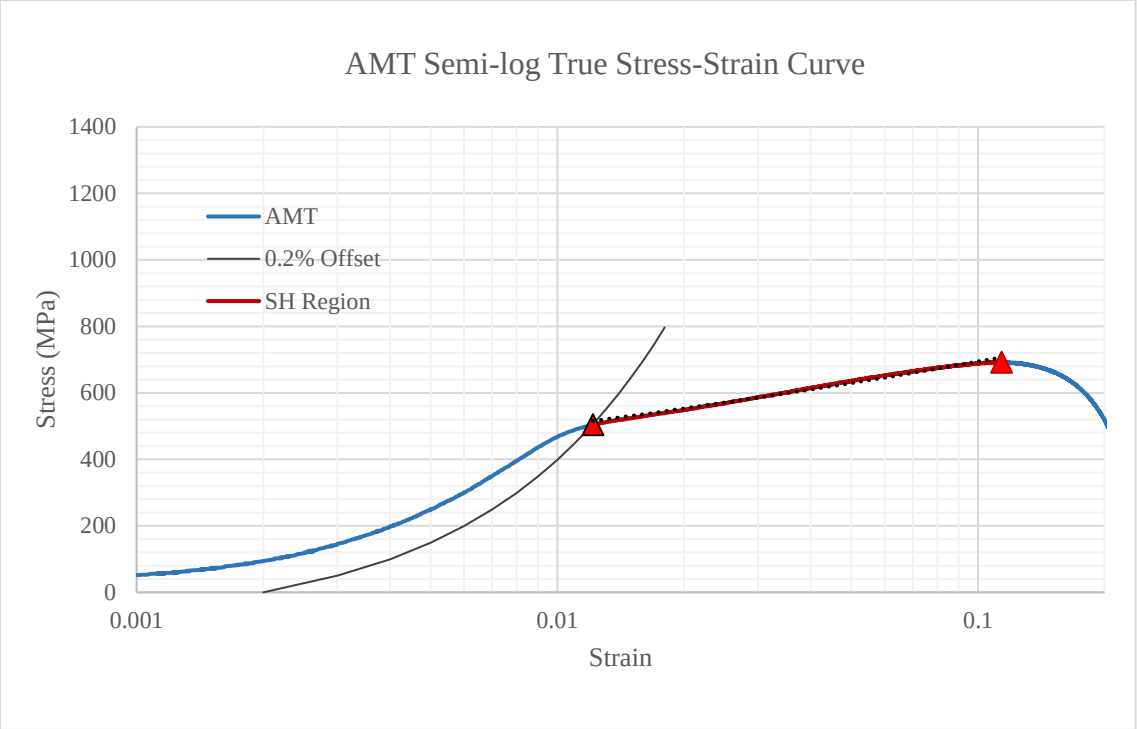

Figure 6.23. Semi-log plot of AMT.

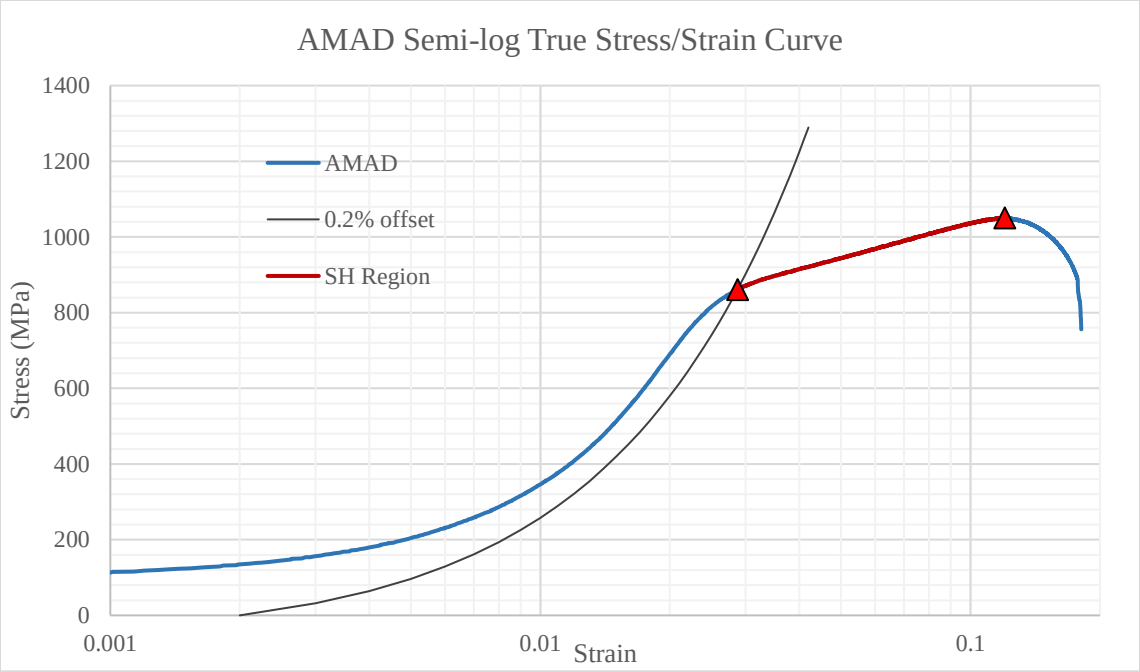

Figure 6.24. Semi-log plot of AMAD.

Reviewing the plots, the normalized and tempered, direct tempered, and as-deposited specimens showed a very closely fit exponential function (linearity in a log plot), with the normalized only heat treated samples adhering less closely to the power law than the other specimen types.

In subchapter 6.1.1, the issue of system compliance and overestimating elastic strain was discussed. In order for Equation 4.2 to be valid, the true strain value at the yield point and ultimate tensile stress must be described with more accuracy than the observed linear elastic slope (which includes compliance). By using the Elastic Modulus (*E*) from literature for the three test temperatures, a more accurate true strain at the yield point can be calculated. Values of E at room at room temperature, 300 ºC, and 600 ºC are taken to be 214 GPa, 195 GPa, and 168 GPa, respectively.

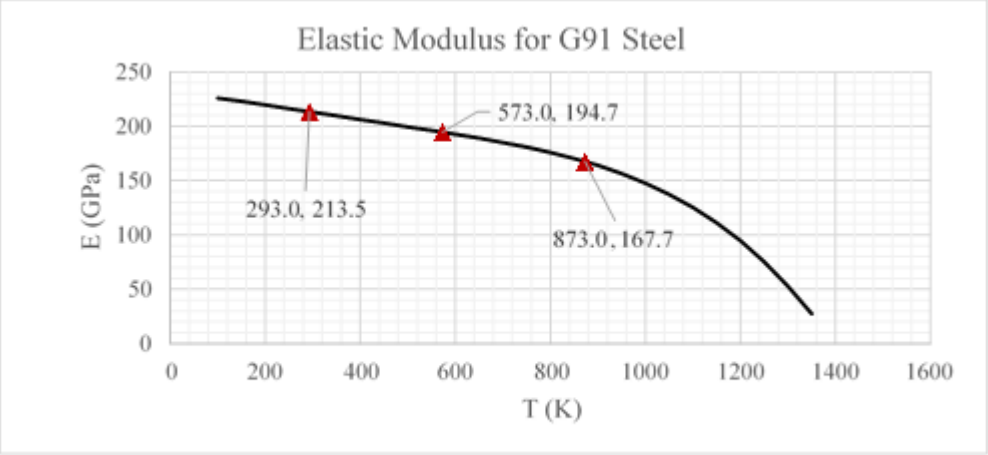

Figure 6.25. Elastic Modulus vs Temperature for Grade 91 Steel [37].

In this manner, a new elastic region is represented with a slope of *E*, such that:

$$\sigma_E = E\varepsilon_E$$

$$\varepsilon_E = \frac{\sigma_e}{E}$$

The Modulus-calculated elastic strain value (ε_E) represents the strain up to the theoretical yield point. To convert to the offset yield point, 0.002 (0.2%) is added to ε_E. To shift the true strain data set such that the strain hardening region (ε_{YS}) begins at the Modulus-adjusted offset point, it was reduced by the difference in strain ($\varepsilon_{YS} - \varepsilon_E$), and then the 0.002 offset shift was added. This is shown graphically in Figure 6.26.

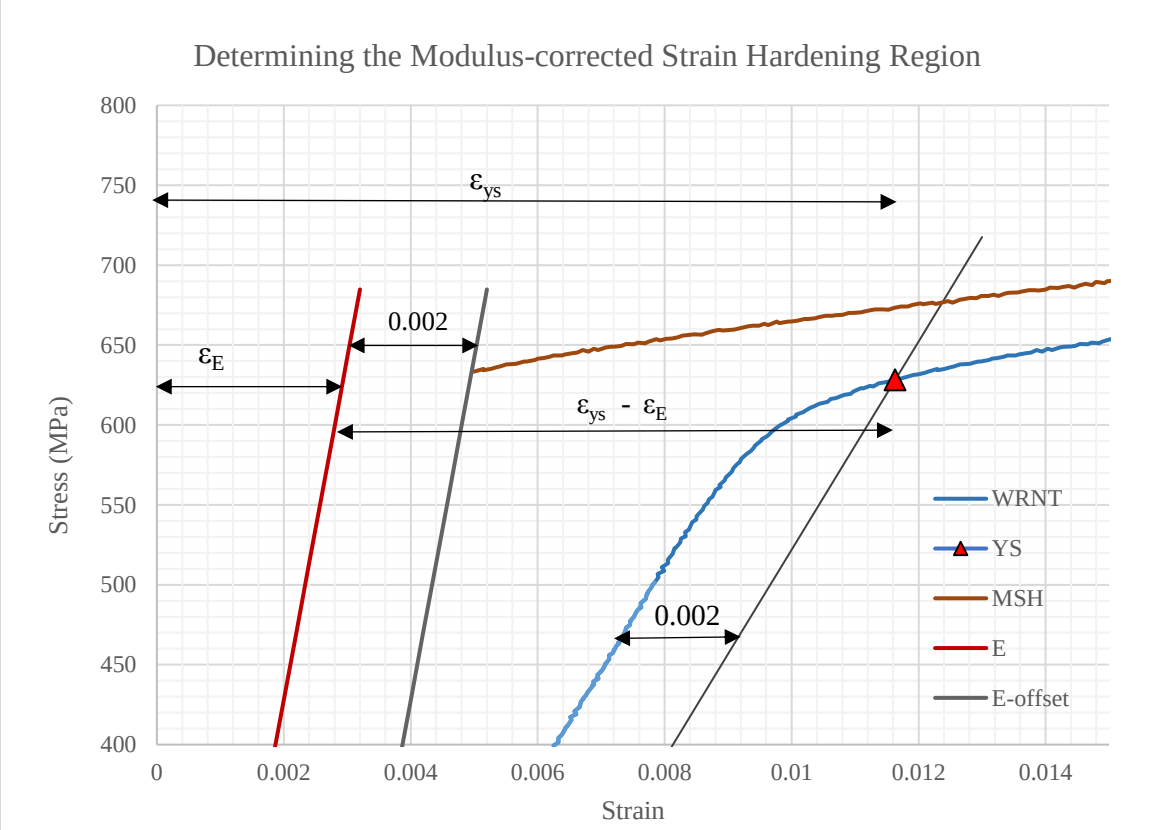

Figure 6.26. Modulus-corrected strain hardening (UE) calculation.

In carrying out this procedure, a new modulus corrected strain hardening region (MSH) plot was generated for each specimen. This "modulus corrected" curve contains the both measured data (the shape and magnitude of the strain hardening region) and simulated

data (the elastic strain limit), and offers a more accurate picture of the stress-strain behavior for calculating strain hardening functions. The modulus-corrected strain hardening functions are plotted below, along with their original true stress-strain curves.

6.3.1. Room Temperature Strain Hardening Functions

The modulus-corrected strain hardening regions are plotted below, along with their original true stress-strain curves. By applying empirical fits to the power law equations, functions of the form given by Equation 4.2 were generated (Figures 6.27-32). The strain hardening functions are isolated and plotted together for comparison in Figure 6.33.

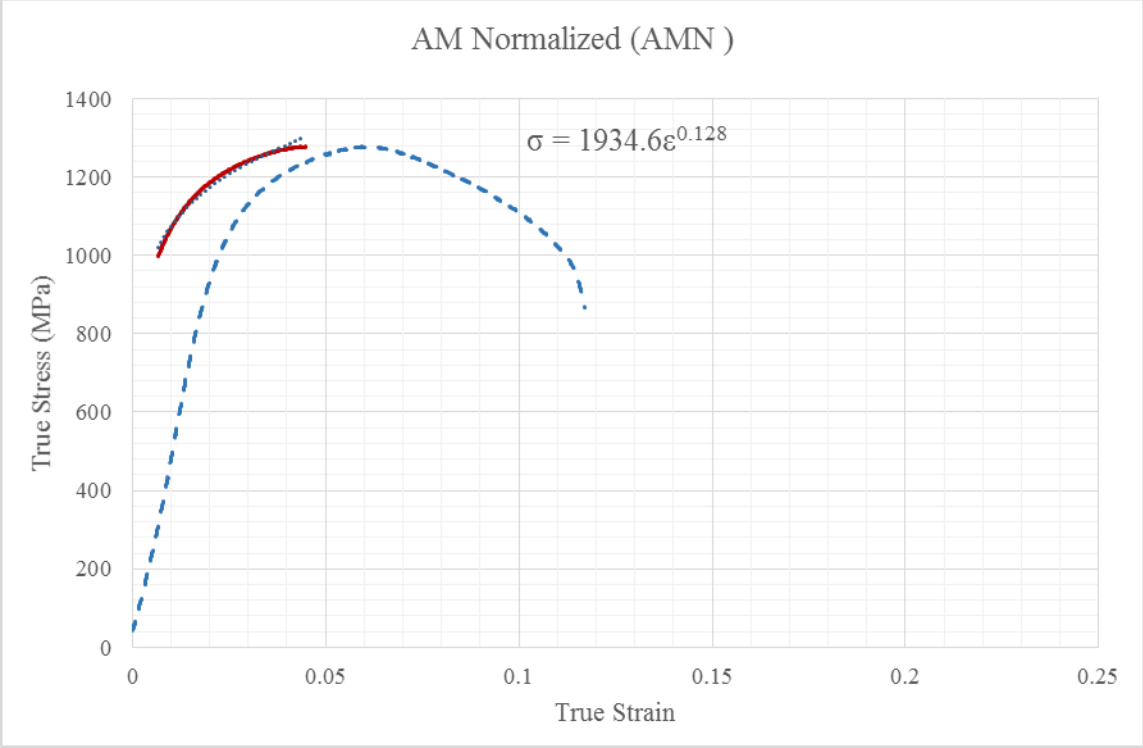

Figure 6.27. RT Strain hardening region of AMN.

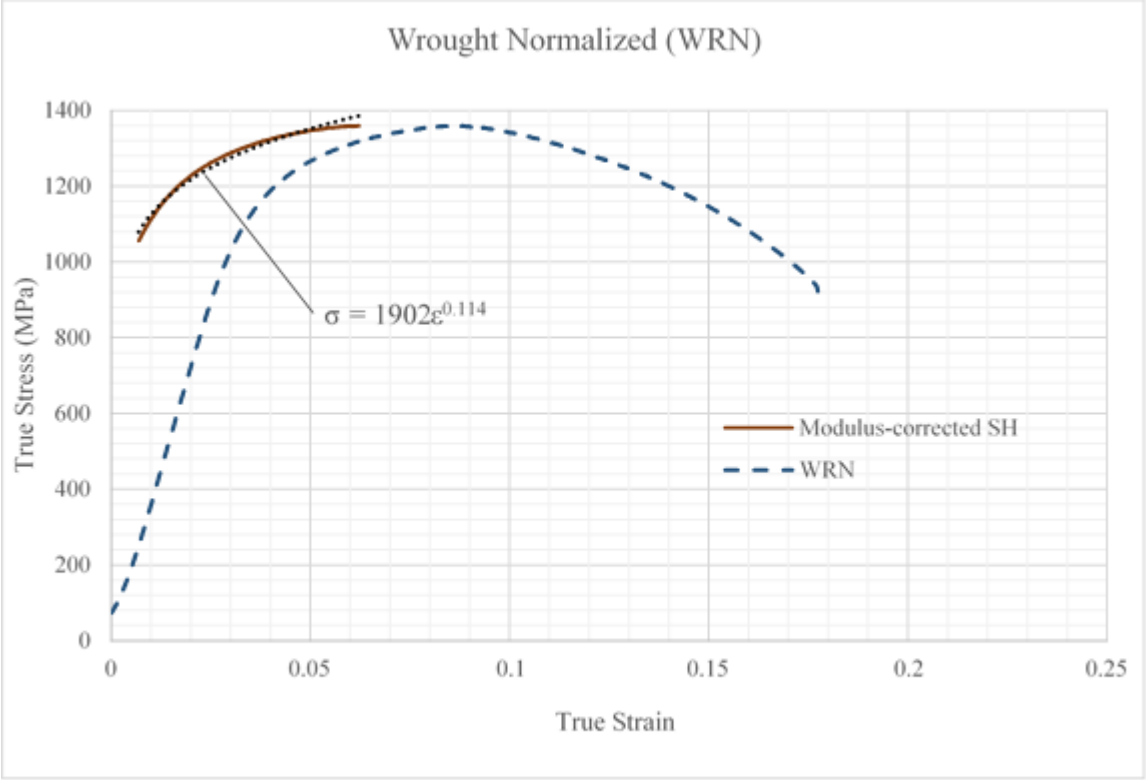

Figure 6.28 . RT Strain hardening region of WRN.

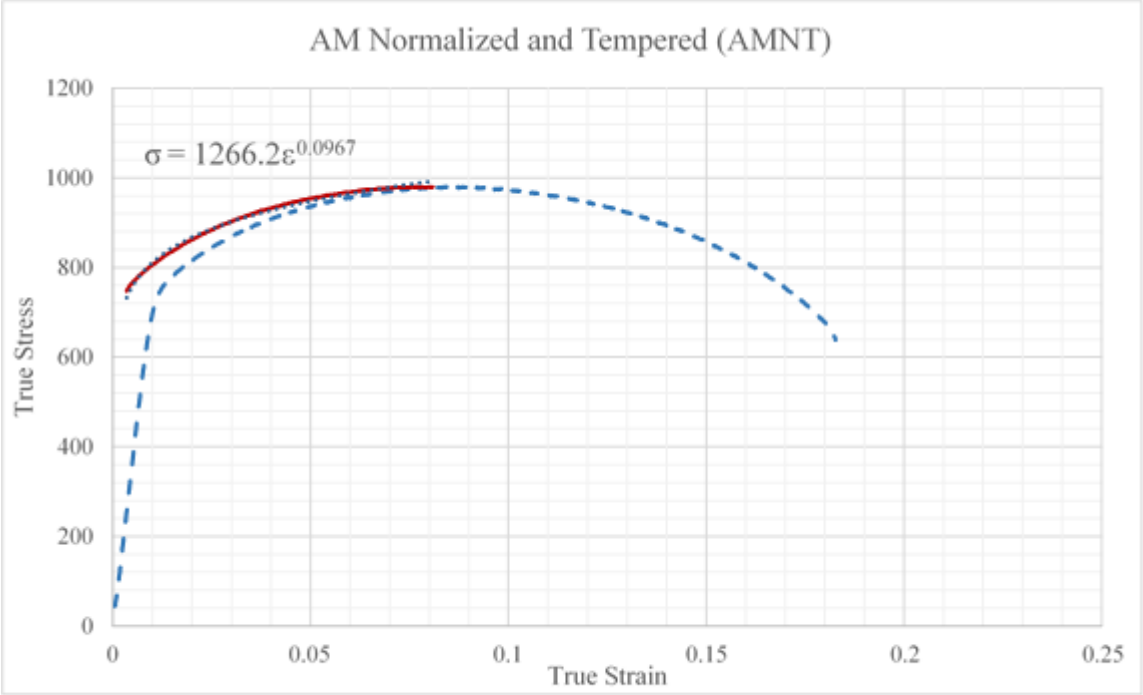

Figure 6.29. RT Strain hardening region of AMNT

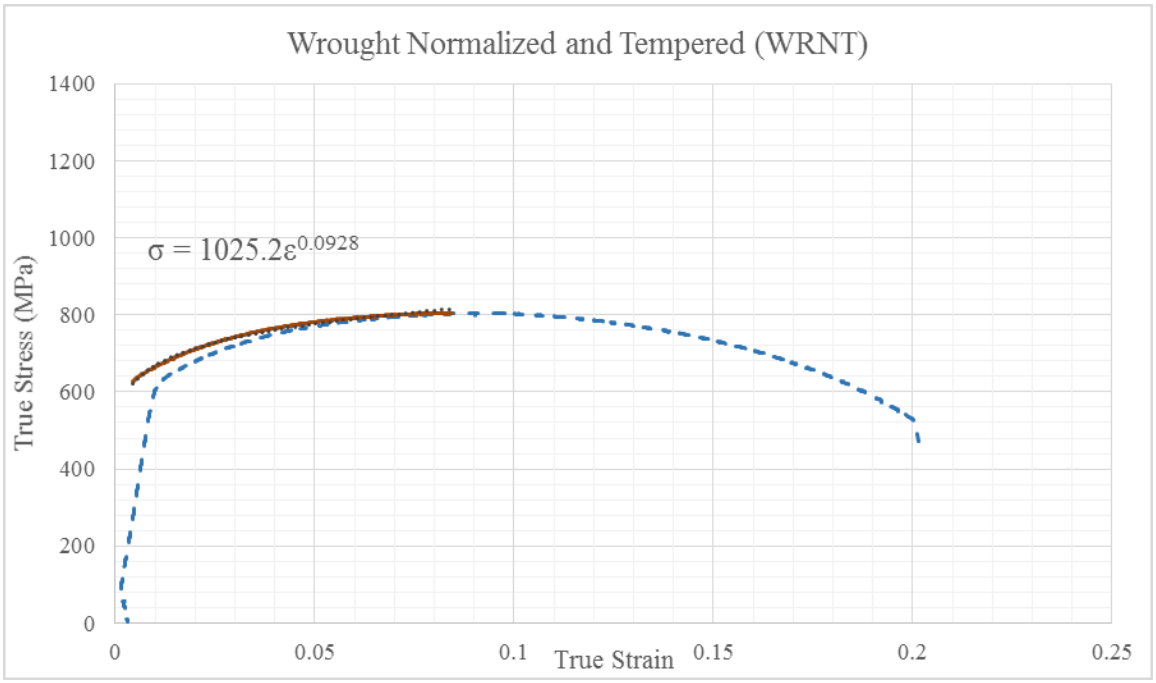

Figure 6.30. RT Strain hardening region of WRNT

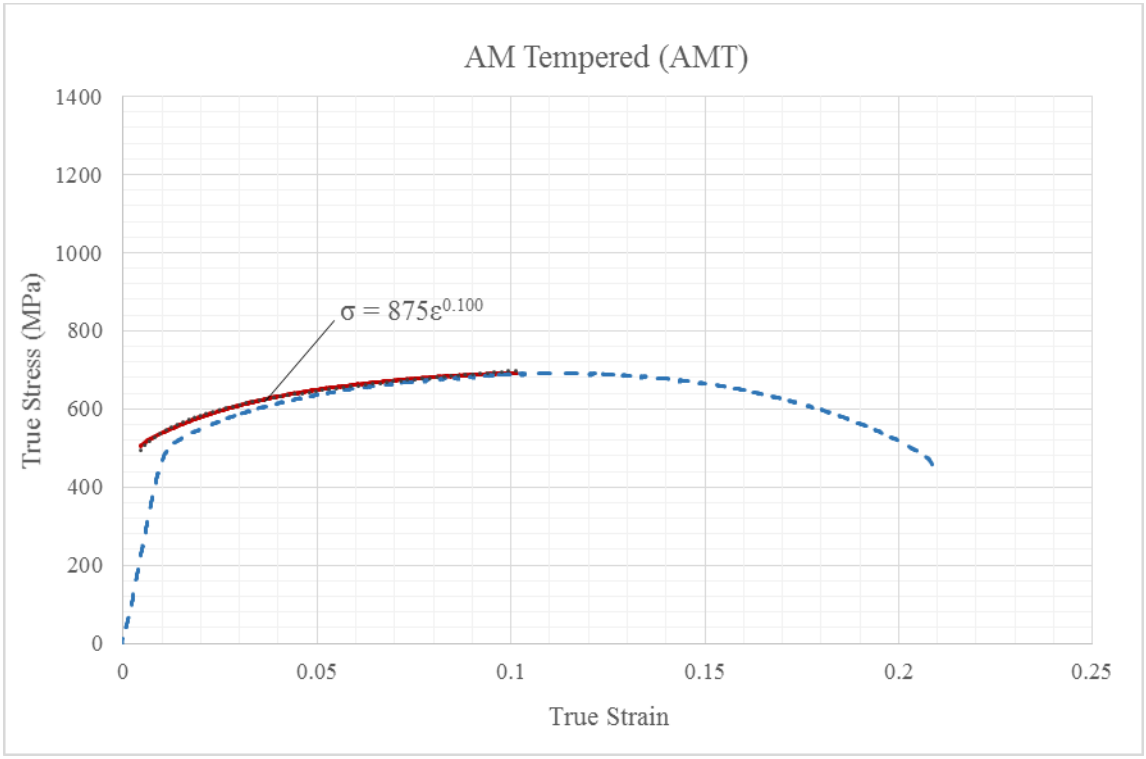

Figure 6.31. RT Strain hardening region of AMT

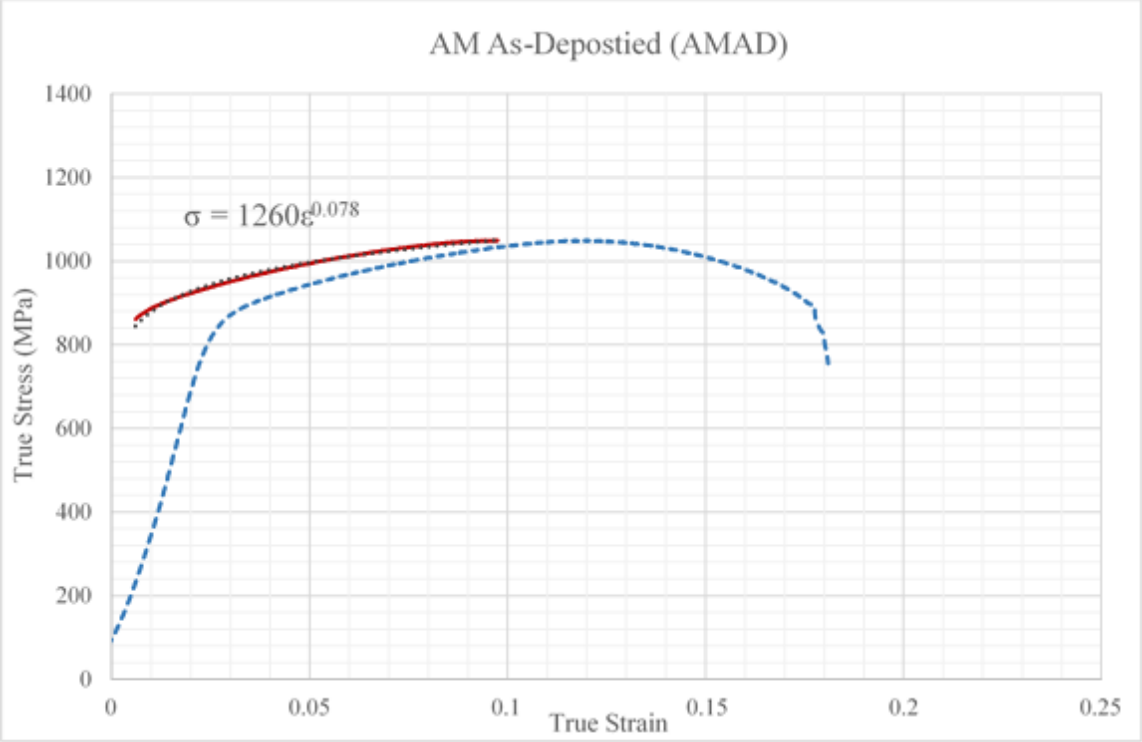

Figure 6.32. RT Strain hardening region of AMAD.

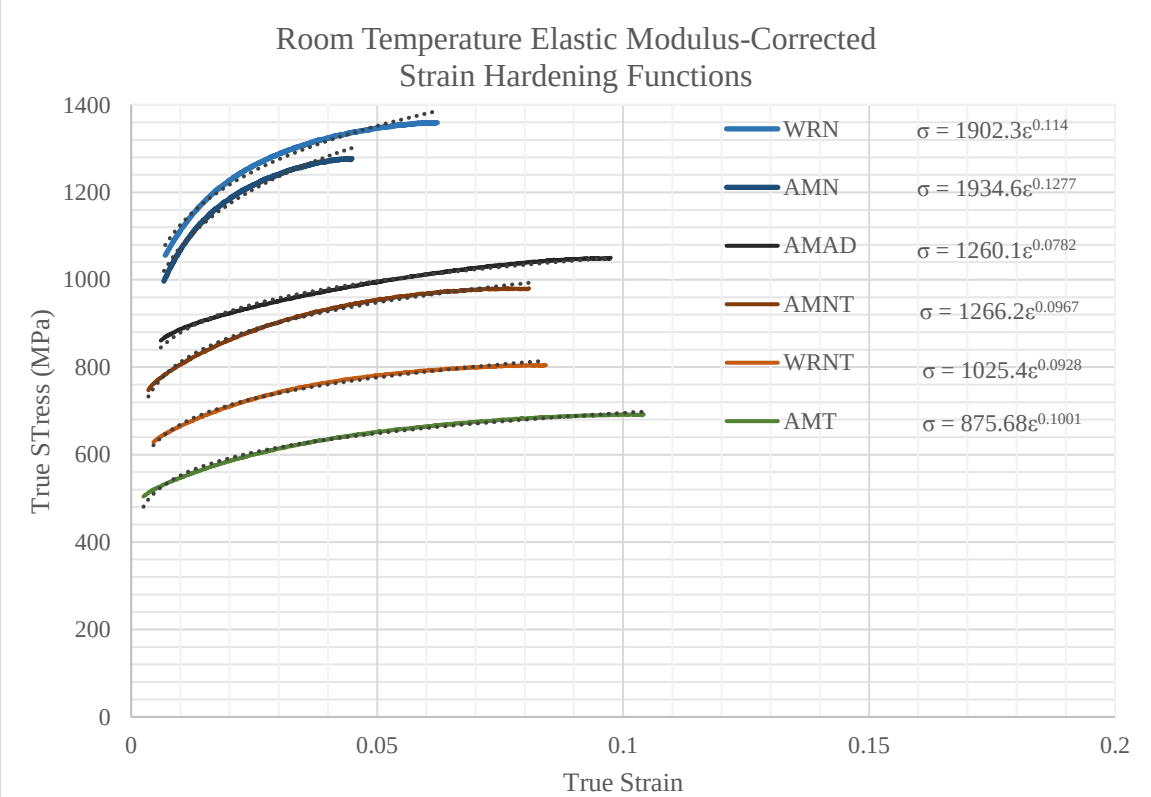

6.33. Modulus-corrected strain hardening functions at RT.

Using the computed values for K (proportionality coefficient), n (strain hardening exponent), and the true strain values, (U_{SH}) was computed for each specimen type, recalling Equation 4.5:

$$U_{SH} = K\left(\frac{{\varepsilon_{UTS}}^{n+1} - {\varepsilon_{YS}}^{n+1}}{n+1}\right)$$

The results from this computation are summarized in Table 6.5, ranked according to Strain Hardening Toughness (U_{SH}):

Specimen	K (MPa)	n	U_{SH} (MJ/m^3) or MPa
AMAD	1260	0.078	90.3
WRN	1902	0.114	70.9
AMNT	1266	0.097	70.8
WRNT	1025	0.093	66.2
AMT	876	0.100	65.0
AMN	1935	0.128	45.8

Table 6.5. RT Strain hardening toughness calculations.

The As-Deposited material (AMAD) once again exhibited unexpectedly favorable strength and ductility, despite having the smallest strain hardening exponent. The next two highest ranked specimens were the two wrought specimens, WRN and WRNT (base case), respectively. The former had the highest strength and the highest strain hardening coefficient (0.128), while the latter had both good strength and ductility. The direct-tempered material (AMT) had a low proportionality coefficient (K), but a wide strain hardening domain (about 10% elongation). The AMNT specimen, similar to the base case, had a combination of both strength and ductility.

6.3.2. Elevated Temperature Strain Hardening Functions

Modulus-corrected stress strain curves were generated for 300 °C tensile specimens, from which strain hardening functions and strain hardening toughness were generated in the same way as for the room temperature specimens (Figure 6.34). Table 6.6 summarizes the proportionality coefficients, and strain hardening exponents, and strain hardening toughness. The same was done for 600 °C specimens.

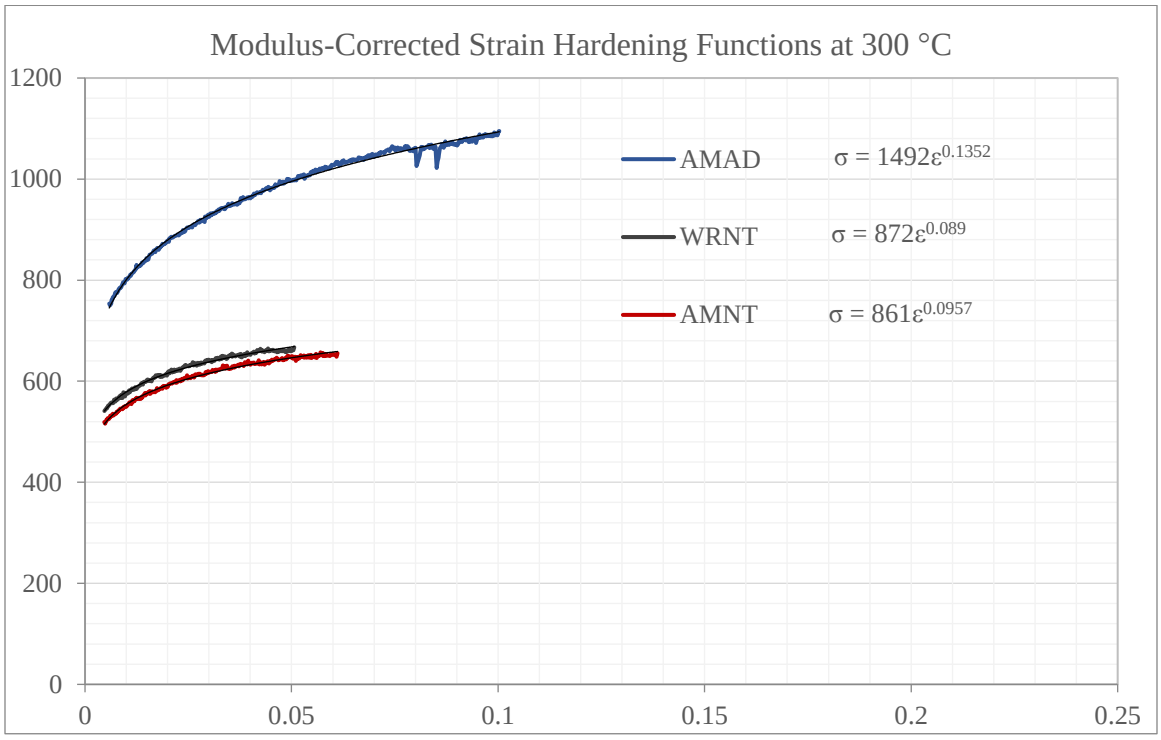

Figure 6.34. Strain hardening functions at 300 °C.

Table 6.6.Strain hardening toughness calculations at 300 °C.

Specimen	K (MPa)	n	U_{SH} (MJ/m^3) or MPa
AMAD	1492	0.14	92.8
AMNT	861	0.10	34.6
WRNT	872	0.09	28.8

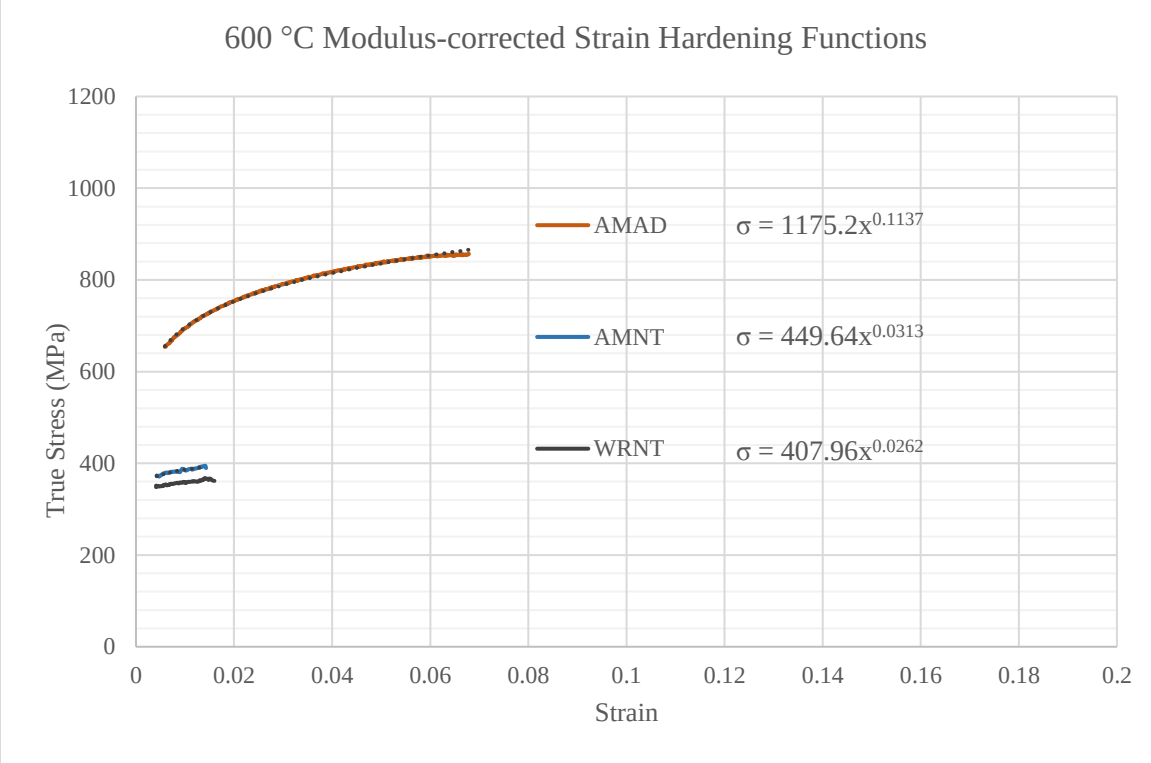

Figure 6.35. Modulus-corrected strain hardening functions

Specimen	K (MPa)	n	U_{SH} (MJ/m^3) or MPa
AMAD	1175	0.11	49.3
AMNT	450	0.03	3.9
WRNT	408	0.03	4.3

Table 6.7.Strain hardening toughness calculations at 600 °C.

6.4. Creep Analysis for Determination of Long-Term Performance

The Strain Rate Jump Test (SRJT) at constant temperature (600 °C) was carried out successfully (after a number of failed attempts), and this investigation was able to generate a dataset of steady state creep rates measuring the (constant) stress on a yielded specimen, varying the strain rate by a factor of 10, observing the stress plateau at a new level, varying the strain rate by a factor of 100, and repeating. Using this method, steady state creep rates were generated for WRNT and AMNT material. These strain rate data were then plotted against the ASME code case data for creep rates for comparison.

Table 6.8. Calculated steady-state creep rate for WRNT

Specimen	Stress (MPa)	$\dot{\varepsilon}_s$ (% hr^{-1})
WRNT-S	250	3.6
	210	36
	350	360

Table 6.9. Calculated steady-state creep rate for AMNT

Specimen	Stress (MPa)	$\dot{\varepsilon}_s$ (% hr^{-1})
AMNT-S	288	3.6
	334	36
	369	360

From the plot (Figure 6.36), the creep rate of ASME code material and AMNT and WRNT from this study both appear to have creep stresses above those of the ASME case, which is a positive result. However, because a true creep test was not performed for very low strain rates, extrapolating over many orders of magnitude has a lot of associated uncertainty. Nonetheless, the demonstration that these steels have a lower creep rate in general warrants further research.

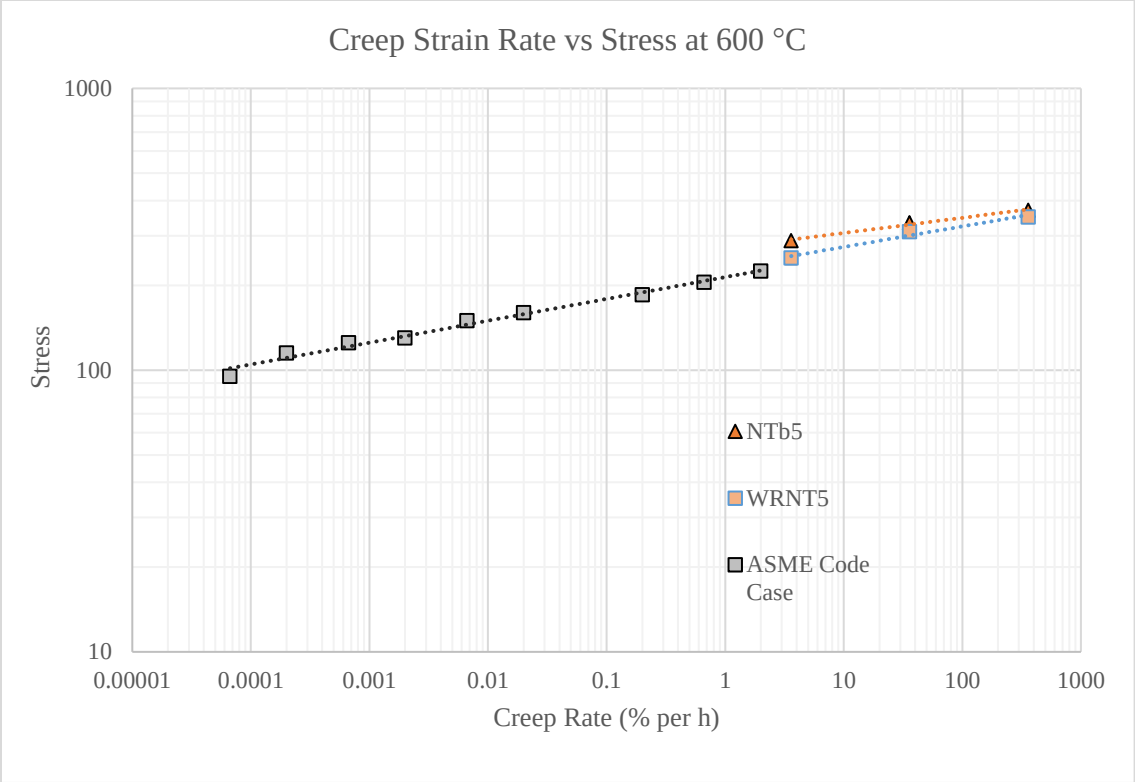

Figure 6.36. Computed steady state creep rate for AMNT and WRNT between 10^{-5} and 10^{-3} s^{-1}.

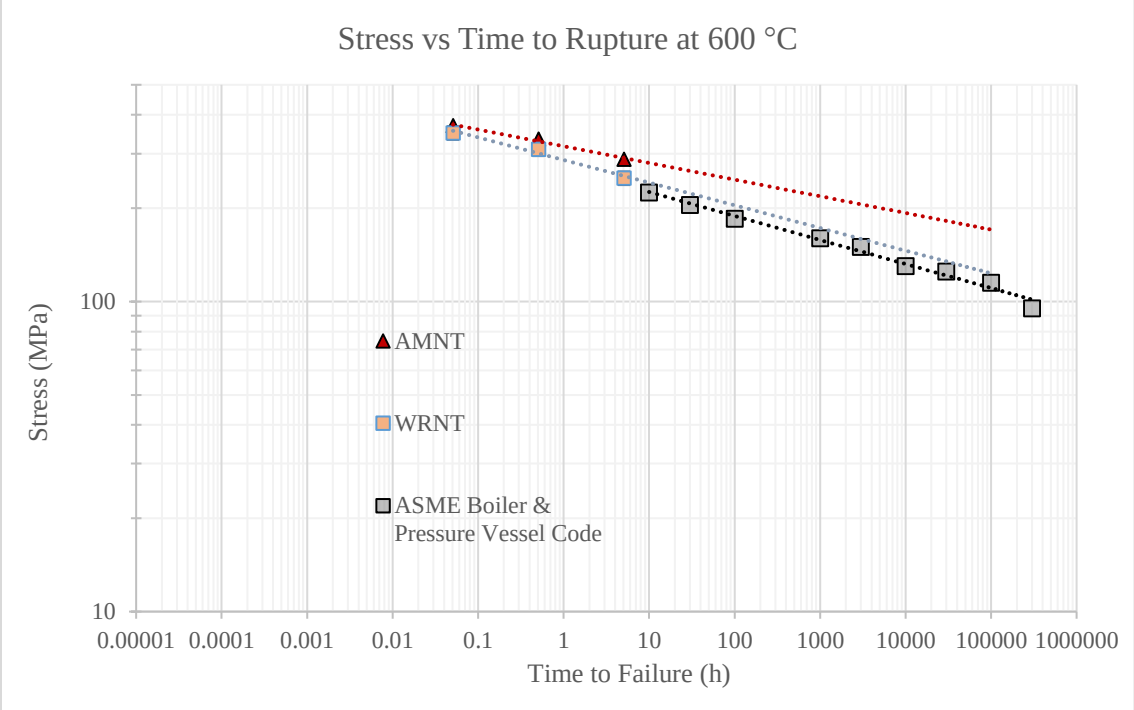

Figure 6.37. Computed stress vs time to rupture for AMNT and WRNT between 10^{-5} and 10^{-3} s^{-1}.

6.5. Thermal Conductivity Analysis Using Laser Flash Analysis

The wrought and AM materials, having essentially the same chemical composition, did not show any observable difference in specific heat. Additionally, the density is mainly governed by the sintering temperature. Thus, to isolate the effects of crystallography on thermal conductivity, each specimen's thermal diffusivity was measured. Using Laser Flash Analysis (LFA), the thermal diffusivity of AM As-deposited (AMAD), AM normalized and tempered (AMNT), and wrought normalized and tempered (WRNT) were measured using a the Netzsch 457 Microflash apparatus. In LFA, thermal conductivity (k) can be calculated from measured values of specific heat (C_p), density (ρ), and thermal diffusivity (α):

$$\alpha = \frac{k}{\rho Cp}, \quad k = \frac{\alpha}{\rho Cp}$$

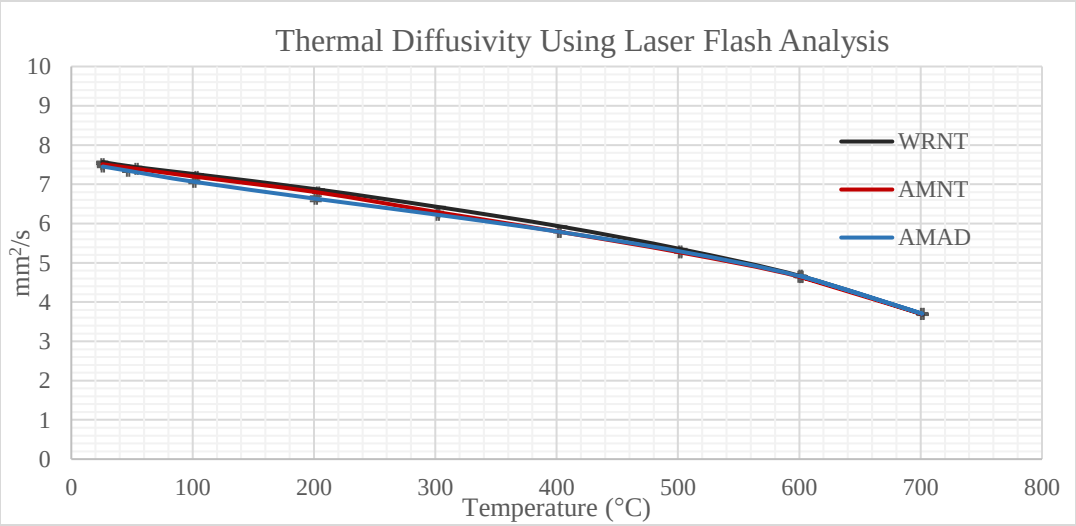

Figure 6.38. Measured Thermal Diffusivity of Various Grade 91 Specimens

As is evident from Figure 6.38, there is no significant difference in thermal diffusivity, and by extension, thermal conductivity. Thus, it is reasonable to conclude that for engineering calculations, the thermal properties of AM and wrought Grade 91 material can be assumed to be equivalent.

6.6. Summary of Mechanical Testing Findings

In summary, the mechanical tests carried out generated the first data set on the strength of AM Grade 91 steel, and showed that in most cases, heat treated AM Grade 91 performed very much like wrought material. ASME code qualification requires that fell sets of data be obtained on a vast number of specimens, multiple heats of material produced independently (to demonstrate reproducibility), and with assessment of additional product form variables (e.g., plates vs tubes). Additionally, this large number of specimens must be tested for YS, UTS, UE, TE, reduction in area, thermal creep properties, creep-fatigue interactions, and other effects [13]. These types of tests generally require years long testing campaigns to complete. However, this investigation was successful in generating the first such data of this type, and thus provides the first insight into potential qualification of AM Grade 91 steel.

Specifically, it was found that:

i) At room temperature, normalized specimens of AM and wrought material both had high UTS, (around 1200 MPa) but low ductility. The AM material had far lower total elongation (around 10%).

ii) AM and wrought material that were normalized and tempered had similar strength, but the AM material was both a slightly harder and slightly less ductile. It is likely that with optimization of heat treatments, they could become more similar.

iii) At 300 °C, WRNT and AMNT exhibited almost identical strength and ductility. Both had UTS of around 650, and total elongation around 16%

iv) At 300 °C, As-deposited material showed very high strength, with a UTS 50% higher than the normalized and tempered material, while experiencing significant strain hardening maintaining nearly the same total elongation at failure as normalized and tempered material.

v) At 600 °C, As-deposited material still showed extreme strengthening behavior, with a pronounced strain hardening region. It had twice the UTS of WRNT and AMNT material, but only around 11% elongation at failure. While AMNT and WRNT material became more ductile between 300 and 600, AMAD did the opposite.

vi) No difference in thermal diffusivity/conductivity was observed among AM and wrought material, nor was it observed for differing heat treatments.

vii) Strain rates, and steady state creep rates were generated for AMNT and WRNT material between 10^{-5} and 10^{-3} s^{-1}. It was found that this corresponds to a creep rate that is less than the ASME code case. While it it is noted that extrapolation of creep rates has high uncertainty, it is a

strong indicator that both steels would perform at least as well as the minimum requirements put forth by the code case.

7. Ion Beam Irradiation Results Nanohardness Analysis

7.1. Calculation of Ion Beam Damage

The ion beam irradiation experiment was carried out successfully on the two prepared foils of AMNT and WRNT material. Upon applying the accelerator current, the adhesive scintillation target was used to align the beam such that the square, monoenergetic ion beam was focused directly on the specimens. With the beam calibrated and focused, the electrical current of 5 MeV Fe^{2+} ions in the final Faraday cup was measured to be 210 nA. Using the elemental atomic charge (e^+) of 1.602 x 10^{-19} C, the ion flux was calculated as follows:

$$210\ nA = \frac{210\ nC}{s} \times \frac{e^+}{1.602\ \times 10^{-10} nC} \times \frac{Fe^{2+}}{2e^+} =$$

$$\frac{6.55 \times 10^{11}\ \ Fe^{2+}}{s}$$

Reviewing the SRIM calculations, this corresponds to a damage rate of :

$$\frac{6.55 \times 10^{11}\ ions}{s} \times \frac{1\ dpa}{10^{15}\ \ Fe^{2+}} =$$

$$\frac{6.55\ \times 10^{-4}\ dpa}{s}$$

Which made for an irradiation time of around 4 hours for 30 dpa, and 9.3 hours for the additional 70 dpa irradiation. By using the Fe K-edge detection method, the 30 dpa irradiation was stopped upon reaching the specific number of x-ray counts, and the system was shut down, and the specimens removed for nanoindentation testing.

7.2. Nanoindentation Analysis of Irradiated specimens

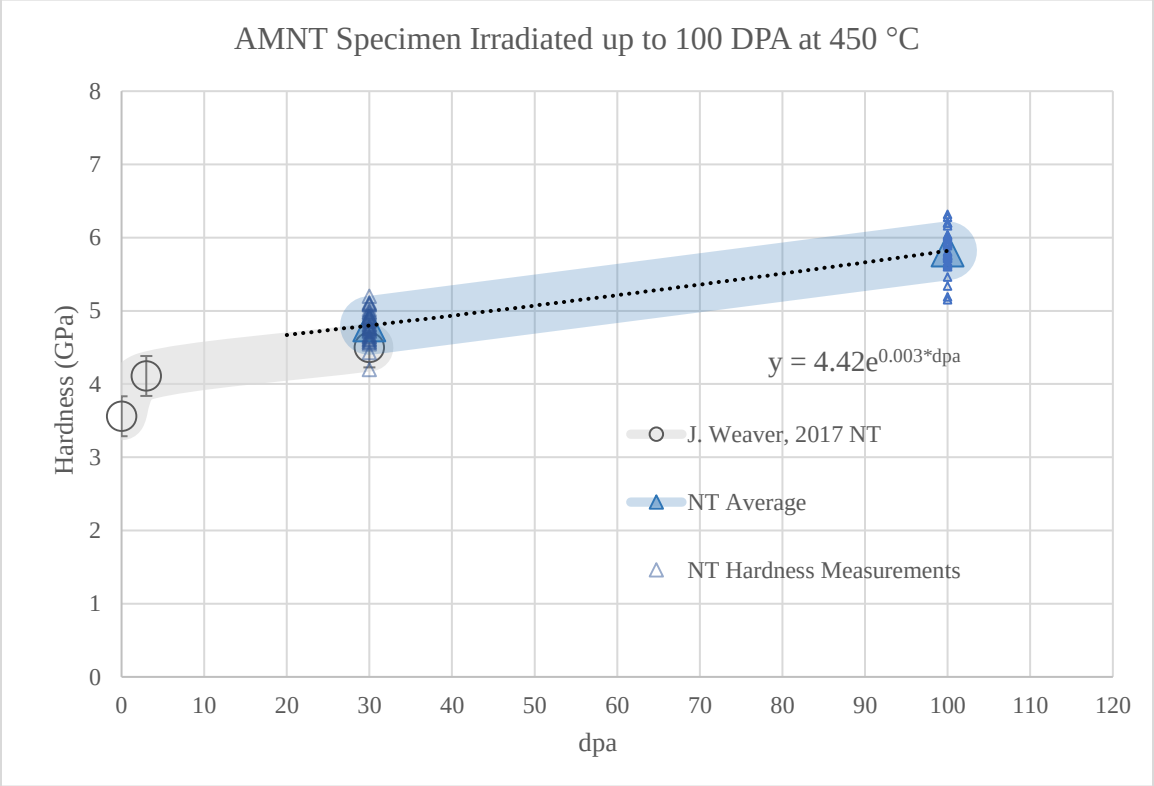

Figure 7.1. AMNT Nanohardness Measurements (36) for 450 °C Irradiations from 0-100 dpa.

There are several sources of error in this calculation. Firstly, the SRIM simulation itself makes a number of assumptions that tend to trade accuracy for computational speed (see subchapter 1.4); this has a stronger effect on damage calculations than penetration range calculations. Secondly, in order to ensure overlap of the nanoindenter interaction volume of the peak dpa region in the specimen (according to the SRIM calculation), a large number of average hardness values are taken over the range of 100 – 300 nm. Though this only represents 0.2 µm, it corresponds to 14.2% of the penetration distance of 5MeV Fe ions, and a number of hardness measurements are averaged together in that region.

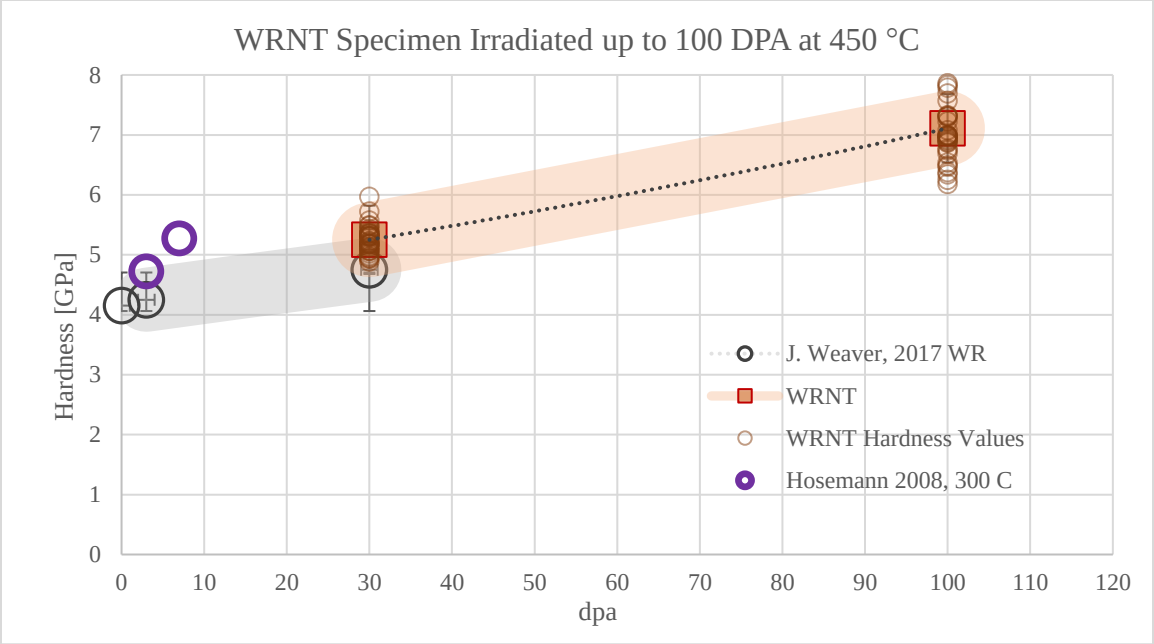

Figure 7.2. WRNT Nanohardness Measurements (36) for 450 °C Irradiations from 0-100 dpa

By using this approach, the AMNT and WRNT (base case) were directly compared (Figure 7.3), giving a clear indication that the base case material experiences more irradiation-induced hardening than the AMNT specimen between 30 and 100 dpa. This high-damage region is crucial to the longevity of advanced reactor components, and according to this study, the AMNT material performs better from an irradiation hardening standpoint in this region. This could result in a greater loss of ductility in the wought material for high dose irradiation exposures.

This difference in radiation damage response from the two steel specimens can be explained by the finer grain size of the AMNT sample. As discussed in Chapter 5, the AMNT material had a finer grain structure than the WRNT. From a performance perspective, Klueh et al. [23] have shown that temperatures above 400 °C tend to mitigate formation and clustering of defects, as they increase the diffusion rate of defects from the

internal lattice to sink locations at grain boundaries. The combination of fine low irradiation swelling, and high temperature operation (500° C-700° C) can be expected to make for a high radiation tolerance of FM steels in general, up to 100 dpa. Furthermore, AM Grade 91 steel, exhibiting a finer grain structure, suggests its radiation damage resistance is even better still.

Future work in AM Grade 91 irradiation analysis should include refining the nanoindentation method to calculate the elastic modulus, and temperature dependent effects on irradiation effects.

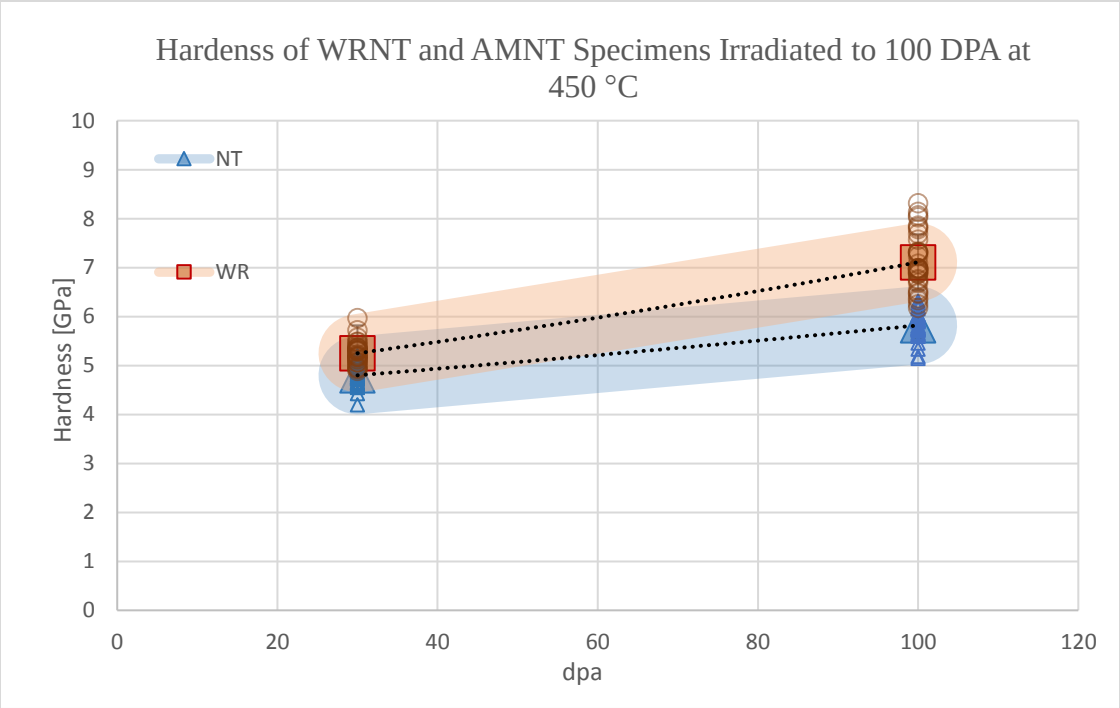

Figure 7.3 AMNT and WRNT Nanohardness Measurements for 450 °C Irradiations from 30 - 100 dpa.

8. Conclusions and Future Work

Though this dissertation represents a preliminary assessment of the suitability of AM Grade 91 material in advanced nuclear applications, it has covered a wide variety of disciplines related to reactor material performance, and the results are highly encouraging. Not only was the first build of Grade 91 successful in building a collection of fully dense specimens free of gross defects, but the specimens were found to have similar martensite fractions to wrought material, and to be highly and favorably responsive to heat treatments. Based upon these findings, additional research into improving AM of ferritic/martensitic steels is warranted.

Though efforts like the

8.1. Contributions to Science

As additive manufacturing promises creative and efficient manufacturing capabilities, it has also opened a new subject in materials science that is interesting from both a practical and an academic perspective. By carrying out the first characterization, mechanical tests, and irradiations of AM Grade 91 steel, this dissertation can conclude that i) not only is AM of FM steels feasible, but that in some cases it has superior qualities to wrought material, ii) Based on these initial findings, the path to qualifying AM Grade 91 has begun; mechanical tests show at least initially, that AM Grade 91 likely has the resistance to swelling, high temperature strength, and ductility that is required tomeet ASME standards. Additionally, this early success suggests that more complicated alloys (like Grade 92 steel) may be amenable to AM methods. Finally, in the course of this investigation, a new, extremely strong Grade 91 allotrope was found. While its exact nature

could not be determined from XRD alone, it exhibited a factor of 2-3 times the strength of code case Grade 91 material at 300 °C and 600 °C, while maintaining good ductility. The fact that this extreme strength was higher than that of both ODS steels and Inconel 617 (a superalloy) was compelling enough to warrant a patent application, which has been submitted by the research group.

8.2. Future Work

In the immediate future, it would be useful to carry out fracture surface testing on the elevated temperature tested specimens. While the AMNT and WRNT specimens increased in ductility between 300 °C and 600 °C, the high strength AMAD material did the opposite. Also, strain rate jump tests can be performed at differing strain rates to improve the uncertainty of this initial set of creep rate calculations. Additionally, attempts to measure the heating cycles of laser AM with embedded instrumentation could build a more accurate understanding of the heat cycling incident upon the build as a function of position. Related to this studies in the near future should be carried out to determine to what extent the orientation of the build has on mechanical strength of AM specimens.

The unexpectedly high strength and ductility of As-deposited material was a compelling result, and additional research is already underway on determining the exact mechanism(s) for this result (i.e., whether this strength is due to purely to phase precipitation, whether a new precipitate phase is forming, or both). Additional builds of AMAD material should be carried out to assess the reproducibility of this material, and further testing on it should include EDS mapping to analyze segregation of constituents, and a rigorous array of tensile tests, including test on direct-tempered material. Buy executing tensile tests above 600 °C, it will be possible to determine at which temperature

the strength disappears, and use that data to determine the nature of the precipitation strengthening it has undergone. Furthermore, the slight difference in room temperature performance of AMNT and WRNT material suggests their heat treatments could be optimized by varying time and temperature to achieve more consistent results. And concurrent to each of these analyses, it is never too early to begin liquid sodium testing on AM components as part of qualification. There are a number of high temperature and high-pressure sodium loops available for such testing.

Appendix I: Fast Reactor Designs and Materials[11]

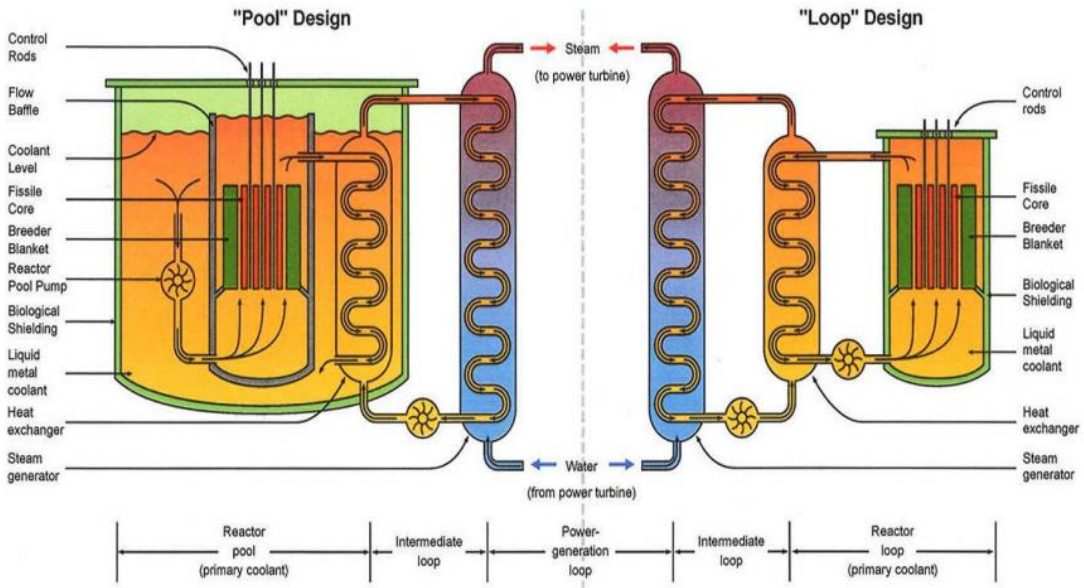

Figure I.1. A. E. Walter and A.B. Reynolds, 1981

Country	Reactor	MWth	Reactor Type	Operating Life (years)	Inlet to IHX Temp. (°C)	Inlet to SG Temp.(°C)
USA	EBR-II	62.5	Pool	30.9	473	467
	FFTF	400	Loop	12.1	565	*
UK	DFR(NaK)	60	Loop	14.4	350	330
	PFR	650	Loop	20.1	550	540
Russia	BOR-60	55	Loop	39.9	545	480
	BN-350	750	Loop	26.4	430	415
	BN-600	1470	Pool	29.7	550	520
France	Phenix	563	Pool	36.2	560	550
	SuperPhenix	2990	Pool	12.4	542	525
Japan	Joyo	140	Loop	32.5	500	470
	Monju	714	Loop	15.6	529	*

*No steam generator and only sodium-to-air heat exchanger.

Structure & Component	Material	Environment	Degradation Process or Mechanism	Factors Controlling Occurrence	Fabrication Capability	Knowledge/ Database
Fuel Cladding	Type 316 SS, 15Cr-15Ni-Ti, Si-modified 15Cr-15Ti-Ti, HT-9, Grade 91 and 92 steels, ODS ferritics	Primary Na Argon gas Fission products, Fuel constituents	Hardening, Swelling, Irradiation creep, Ductility loss, Helium embrittlement Weld integrity	Neutron fluence Service temperature Service life Na compatibility Fuel-side compatibility	Good for austenitics Fair to insufficient for ferritics	Adequate for low burn up
Ducts, Wire Wrapper	Type 316 SS	Primary Na & argon gas	Hardening, Swelling, Irradiation creep, Ductility loss Helium embrittlement Weld integrity	Neutron fluence Service temperature Service life Na compatibility	Good	Adequate for low burn up

Table I.1. Materials Candidated for In-core Components11

Fast Reactor and Micro-Reactor Concepts:						
Reactor Name	**Type [1]**	**Power MWe**	**Fuel**	**Coolant**	**Developer**	**Development Status**
Advanced Reactor Concept (ARC-100)	**SFR**	**100**	**Metal**	**Sodium**	**ARC**	**Under license application**
Power Reactor for Innovative Small Module (PRISM)	**SFR**	**370,**	**Metal**	**Sodium**	**GE**	**Reviewed preliminary license application**
Demonstration Lead-cooled Fast Reactor (DLFR)	**LFR**	**210**	**Oxide (Nitride)**	**Lead**	**Westinghouse**	**Under design**
Amphora-Shaped Lead-cooled Fast Reactor (LFR-AS-200)	**LFR**	**200**	**Oxide**	**Lead**	**Hydromine**	**Under design**
Columbia Basin Consulting Group (CBCG)	**LFR**	**~100**	**Oxide (initially)**	**(LBE)**	**CBCG**	**Under design**
Advanced Fast Reactor (AFR-100)	**SFR**	**100**	**Metal**	**Sodium**	**ANL**	**Under design**
Gen4 Module	**LFR**	**25**	**Nitride**	**LBE**	**Gen4 Energy**	**Under design**
Oklo	**SFR**	**2**	**Metal**	**Sodium**	**Oklo**	**Under design**
Westinghouse LFR	**LFR**			**Liquid Metal**	**Westinghouse**	**Under design**
Toshiba 4S (Super-Safe, Small, and Simple	**LFR**			**Liquid Metal**	**Toshiba**	**Under design**
ENVINCI ™ Micro Reactor				**Heat Pipe**	**Westinghouse**	**Under design**
LANL Heat Pipe				**Potassium Heat Pipes**	**LANL**	**Under design**

Table I.2. List of selected candidate fast reactors and micro-reactor under development.

List of References

1) Brinton, Sam. “The Advanced Nuclear Industry.” – *Third Way*, www.thirdway.org/report/the-advanced-nuclear-industry.

2) “Gateway for Accelerated Innovation in Nuclear // .” *Gateway for Accelerated Innovation in Nuclear*, gain.inl.gov/SitePages/Home.aspx.

3) Maziasz, P.J. JOM (2018) 70: 66. “Development of Creep-Resistant and Oxidation-Resistant Austenitic Stainless Steels for High Temperature Applications”.

4) Kluek, R.L., “Elevated temperature Ferritic and martensitic steels and their application to future nuclear reactors”, International Materials reviews, Vol. 50, No.5, 2005, pp287- 310.

5) Fujimitsu Masuyama, John P. Shingledecker, “Recent Status of ASME Code on Creep Strength Enhanced Ferritic Steels”, Procedia Engineering,Volume 55, 2013, Pages 314-325, ISSN 1877-7058,

6) Y. Yamamoto, “Improving the Performance of Creep Strength Enhanced Ferritic/Martensitic Steels”. *NETL Crosscutting Research Review Meeting, Pittsburgh, PA. May 19 – 23, 2014*

7) Y.Z. Shen, S.H. Kim, H.D. Cho, C.H. Han, W.S. Ryu, J. Nucl. Mater. 400 (2010) 64–68.

8) R.L. Klueh, Int. Mater. Rev. 50 (2005) 287–310.

9) “U.S. Energy Information Administration - EIA - Independent Statistics and Analysis.” *Electricity - U.S. Energy Information Administration (EIA)*, 2014, www.eia.gov/electricity/.

10) Task Force on Energy Systems for Forward/Remote Operating Bases, Final Report. Department of Defense, Defense Science Board, August 1, 2016

11) K.Natesan, M. Li, “Materials Performance in Sodium-Cooled Fast Reactors: Past, Present and Future”. International Conference on Fast Reactors and Related Fuel Cycles: Safe Technologies and Sustainable Scenarios, Paris, France, March 4-7, 2013.

12) BPVC Section III-Rules for Construction of Nuclear Facility Components-Division 1-Subsection NB-Class 1 Components

13) S.J. Zinkle, "Qualification of Structural Materials for Fission and Fusion Reactor Systems", Joint ICFRM-14 and IAEA Satellite meeting on Cross-cutting issues of Structural Materials for Fusion and Fission Applications, Sapporo, Japan, September 10-11, 2009

14) Was, G. S., J. P. Wharry, B. Frisbie, B. D. Wirth, D. Morgan, J. D. Tucker, and T. R. Allen, "Assessment of radiation- induced segregation mechanisms in austenitic and ferritic –martensitic alloys," Journal of Nuclear Materials 411, no. 1 (2011): 41-50.

15) D.V. Rao, unpublished research

16) M. Nastasi, J. W. Mayer, Ion Implantation and Synthesis of Materials, Springer, Berlin, 2006.

17) Klueh, R.L. and D.R. Harries, "High-Chromium Ferritic and Martensitic Steels for Nuclear Applicaitons", ASTM, West Conshohocken, PA

18) Los Alamos National Laboratory, et al. "Ion Beam Materials Lab." *LANL Newsroom*, 12 Apr. 2012, www.lanl.gov/science-innovation/science-facilities/ion-beam-materials-lab/index.php.

19) Was, Gary S. *Fundamentals of Radiation Materials Science: Metals and Alloys*. Springer New York, 2017.

20) Kinchin G.H., Pease R.S., (1955) Rep Prog Phys 18:1

21) M.J. Norgett, M.T. Robinson, I.M. Torrens, "A proposed method of calculating displacement dose rates" Original Research Article, Nuclear Engineering and Design, Volume 33, Issue 1, August 1975 , Pages 50-54

22) Banisalman, Mosab. "Evaluation of the Threshold Displacement Energy in Tungsten by Molecular Dynamics Calculations." *Journal of Nuclear Materials*, North-Holland, 15 Aug. 2017,

23) Klueh RL, Harries DR, ASTM International. *High-Chromium Ferritic and Martensitic Steels for Nuclear Applications*. W. Conshohocken, PA: ASTM; 2001. doi:10.1520/MONO3-EB

24) D. R. Harries, Rad. Effects 101 (1987) 3.

25) D. R. Harries and E. Zolti, Nucl. Eng. and Design/Fusion 3 (1986) 331.

26) "Cross Sections of Ni." *Table of Nuclides*, atom.kaeri.re.kr/nuchart/.

27) Callister, William D., and David G. Rethwisch. *Fundamentals of Materials Science and Engineering: an Integrated Approach*. John Wiley & Sons, 2008.

28) D. Gallina, Finite element prediction of crack formation induced by quenching in a forged valve, Engineering Failure Analysis, Volume 18, Issue 8, 2011, Pages 2250-2259, ISSN 1350-6307

29) DiStefano, J.R. *et al*., *Summary of Modified 9Cr-1Mo Steel Development Program: 1975–1985*, ORNL-6303, October 1986.

30) T. Flament, P. Tortorelli, V. Coen, H.U. Borgstedt, Compatibility of materials in fusion first wall and blanket structures cooled by liquid metals, Journal of Nuclear Materials, Volumes 191–194, Part A,1992,Pages 132-138

31) Lev D Ryabev,Journal of Nuclear Materials,Volumes 233–237, Part 1, 1996,Pages vii-viii, ISSN 0022-3115

32) P. J. Maziasz and R. L. Klueh, in: Effects of Radiation on Mate- rials: 15th International Symposium, ASTM STP 1125, Eds. R. E. Stoller, A. S. Kumar, and D. S. Gelles (ASTM, Philadelphia, 1992) 1135.

33) C.A. Hippsley & N. P. Haworth, Hydrogen and temper embrittlement in 9Cr–1Mo steel. Pages 791-802 | Published online: 18 Jul 2013

34) ASTM International; erstwhile American Society for Testing of Materials

35) Kimura K, Kushima H, Abe F, Yagi K, Irie H. et al, , *"Advances in Turbine Materials, Design and Manufacturing". London Institute of Materials", (1997) 257–69.*

36) Poitevin, Y. and R. Lenain, "Evaluation of the Mechanical Behavior of a 9Cr-1Mo Martensitic Steel Beam Window," presented at AccApp 98, Gatlinburg, TN, Sept. 20–23, 1998.

37) ASME Boiler & Pressure Vessel Code, Section II, Part D, 1998.

38) Stainless 316, 316L, 317, 317L." *United Performance Metals*, www.upmet.com/sites/default/files/datasheets/316-316l.pdf.

39) Laffont, G.,Commissariat à l'Energie Atomique (France), personal communication, January 2002.

40) T, W. Watson and II, E. Robinson, “Thermal Conductivity of a Sample of Type 316 Stainless Steel”, National Bureau of Standards, NBS Project 1006-30-10642, 1963.

41) Hansen, M.,Constitution of Binary Alloys, McGraw-Hill Book Company, 1958.

42) R. G. Faulkner, E. A. Little, and T. S. Morgan, J. Nucl. Mater. 1914194 (1992)

43) R. G. Faulkner, N. C. Waite, E. A. Little, and T. S. Morgan, Mater. Sci. Eng. 171 (1993) 241.

44) R. G. Fanlkner, S. Song, and P. E. J. Flewitt, J. Nucl. Mater. 212- 215 (1994) 608.

45) A. Alamo, Proceedings of IEA Workshop/Working Group Meet- ing on Ferritic/Martensitic Steels, Ed. R. L. Klueh, Oak Ridge National Laboratory, ORNL/M-6627, 1998.

46) A. Hishinuma, Proceedings of IEA Workshop/Working Group Meeting on Ferritic/Martensitic Steels, Ed. R. L. Klueh, Oak Ridge National Laboratory, ORNL/M-6627, 1998.

47) S. Ukai, M. Harada, H. Okada, M. Inoue, S. Nomura, S. Shikakura, K. Asabe, T. Nishida, and M. Fujiwara, J. Nucl. Mater. 204 (1993) 65.

48) S. Ukai, M. Harada, H. Okada, M. Inoue, S. Nomura, S. Shikakura, T. Nishida, M. Fujiwara, and K. Asabe, J. Nucl. Mater. 204 (1993) 74.

49) E. Artz, in: New Materials and Mechanical Alloying Tech- niques, Eds. E. Artz and L. Schultz (Deutsche Gesellschaft fur Materialkunde eV, 1989) 185.

50) K. Onel and J. Nutting, Met. Sci. 13 (1979) 573.

51) P. J. Grobner and W. C. Hagel, Metall. Trans. 11A (1980) 633.

52) M. Pelletier, R. M. Vilar, and G. Cizeron, J. Nucl. Mater. 105 (1982) 237.

53) M. Suzuki, A. Hishinuma, P. J. Maziasz, and T. Sawai, J. Nucl. Mater. 170 (1990) 270.

54) J. M. Vitek and R. L. Klueh, Metall. Trans., 14A (1983) 1047.

55) M. Tamura, H. Hayakawa, A. Yoshitake, A. Hishinuma, and T. Kondo, J. Nucl. Mater. 155-157 (1988) 620.

56) K. Tokuno, K. Hamada, and T. Takeda, J. Metals 44(4) (1992) 25.

57) Kini, Anoop. "Design and Synthesis of an ODS Steel by LAM." *Design and Synthesis of an ODS Steel by LAM | Max-Planck-Institut Für Eisenforschung GmbH*. N.p., 2018.

58) ASME 2017 Pressure Vessels and Piping Conference, Volume 6A: Materials and Fabrication Waikoloa, Hawaii, USA, July 16–20, 2017 Conference Sponsors: Pressure Vessels and Piping Division, ISBN: 978-0-7918-5799-1

59) *ASME Boiler & Pressure Vessel Code*, Section III, Subsection NH (revised 2002)

60) V.S. Srinivasan, B.K. Choudhary, M.D. Mathew, T. Jayakumar, Mater. High Temp. 29 (2012) 41–48.

61) H. Fricker and B. Walser, in: Ferritic Steels for Fast Reactor Steam Generators, Eds. S. F. Pugh and E. A. Little (British Nuclear Energy Society, London, 1978) 35.

62) A. Fleming, R. V. Maskell, L. W. Buchanan, and T. Wilson, in: Materials for High Temperature Power Generation and Process Plant Applications, Ed. A. Strang (The Institute of Materials, London, Book 728, 2000) 33.

63) G. J. Bignold, in: Ferritic Steels for Fast Reactor Steam Generators, Eds. S. F. Pugh and E. A. Little (British Nuclear Energy Society, London, 1978) 342.

64) J. P. Broomfield, J. E. Forrest, D. R. Holmes, and M. I. Manning, in: Topical Conference on Ferritic Alloys for Use in Nuclear Energy Technologies, Eds. J. W. Davis and D. J. Michel (Met. Soc. AIME, New York, 1984) 77.

65) Fleming, R. V. Maskell, L. W. Buchanan, and T. Wilson, in: Materials for High Temperature Power Generation and Process Plant Applications, Ed. A. Strang (The Institute of Materials, London, Book 728, 2000) 33.

66) J. P. Broomfield, J. E. Forrest, D. R. Holmes, and M. I. Manning, in: Topical Conference on Ferritic Alloys for Use in Nuclear Energy Technologies, Eds. J. W. Davis and D. J. Michel (Met. Soc. AIME, New York, 1984) 77.

67) M. Aubert, B. Mathieu, and P. Petrequin, in: Topical Conference on Ferritic Alloys for Use in Nuclear Energy Technologies, Eds. J. W. Davis and D. J. Michel (Met. Soc. AIME, New York, 1984) 245.

68) L. Colombier, Molybdenum in Stainless Steels and Alloys (Climax Molybdenum Co., Ann Arbor, MI, 1968).

69) A. P. Bond, J. D. Marshall, and H. J. Dundas, in: Stress Corrosion Testing, ASTM STP 425 (American Society for Testing and Materials, Philadelphia, 1967) 116.

70) P. J. Ennis and W. J. Quadakkers, in: PARSONS 2000, Advanced Materials for 21 st Century Turbines and Power Plant, Eds.

71) A. Strang, W. M. Banks, R. D. Conroy, G. M. McColvin, J. C. Neal and S. Simpson, (The Institute of Materials, London, Book 736, 2000) 265.

72) R. P. Anantatamula, W. F. BrehmSodium compatability of HT-9 and Fe-9 1-Mo Steels. Westinghouse Hanford.

73) Yvon, Pascal & Carré, Frank. (2009). Structural Materials Challenges for Advanced Reactor Systems. Journal of Nuclear Materials. 385. 217-222. 10.1016/j.jnucmat.2008.11.026.

74) Y. Chen, "Irradiation Effects of HT-9 Martensitic Steel", Nuclear Engineering and Technology, vol.45, No.3 June 2013.

75) R. L. Klueh and J.M. Vitek, *Journal of Nuclear Materials* 132 (1985) 27-31.

76) Toloczko, M.B., F.A. Garner, and C.R. Eiholzer, "Irradiation Creep and Swelling of the US Fusion Heats of HT9 and 9Cr-1Mo to 208 dpa at ~400°C," Journal of Nuclear Materials 212–215, 1994, 604-607.

77) Hydrogen embrittlement susceptibility of tempered 9%Cr-1% Mo steel L. Marchetti a , E. Herms a , P. Laghoutaris a , J. Cheˆne b, * aCEA, DEN, DPC, SCCME, Laboratoire d'Etude de la Corrosion Aqueuse, F-91191 Gif-sur-Yvette, France

78) E. Amar, A. Pineau, Interpretation of ductile fracture toughness temperature dependence of a low strength steel in terms of a local approach, Eng. Frac. 478 A. Pineau et al. / Acta Materialia 107 (2016) 424e483 Mech. 22 (1985) 1061e1071.

79) J. Harding, "Effect of temperature and strain rate on strength and ductility of four alloy steels", Met. Technol. 4 (1977) 6e16.

80) V.K. Sikka, Elevated Temperature Ductility of Types 304 and 316 Stainless Steel, Tech. rep., Oak Ridge National Laboratory, Tennessee, 1978.

81) A. Lambert-Perlade, Rupture par clivage de microstructures d'aciers bainitiques obtenues en conditions de soudage, Ph.D. thesis, Ecole de Mines de Paris, France, 2001.

82) D. J. Abson and J. S. Rothwell* Review of type IV cracking of weldments in 9–12%Cr creep strength enhanced ferritic steels. TWI Ltd International Materials Reviews, November 2013, 58(8), 437-473.

83) "WELDLIFE - Avoidance of P91 Type IV Failure in P91 and P92 Steels." *ETD Consulting*. N.p., n.d.

84) M. Yaguchik, A. Nakamura, S. Nakahashi, "Re-evaluation of Long-term Creep Strength of Welded Joint of ASME Grade 91 Type Steel"

85) Ohadi, Michael. "AM Processes: Powder Based AM." *Schedule of Classes*. Sept. 2017. Web.

86) Newman, John. "EADS, EOS Pair for AM Sustainability Study." *Rapid Ready Technology*. N.p., 05 Feb. 2014. Web. 18 Apr. 2018.

87) Leinenbach, S., Los Alamos National Security, LLC, and U.S. Department of Energy. "Advanced Qualification of Additive Manufacturing Materials (AM) Workshop." July 2015.

88) M. Agarwala et al., "Direct selective laser sintering of metals". Rapid Prototyping Journal Vol. 1 · Number 1 · 1995 · pp. 26–36 © MCB University Press · ISSN 1355-2456.

89) "Systems and Solutions for Metal Additive Manufacturing." *EOS Additive Manufacturing of High-quality Metal Parts*.

90) T. Lienart, unpublished research.

91) C. Salzbrennera, High-throughput stochastic tensile performance of additively manufactured stainless steel, Journal of Materials Processing Technology, Journal of Materials Processing Technology 241 (2017) 1–12,

92) S. Maloy, CAD Drawings provided by LANL staff

93) LFA 457 MicroFlash®." *NETZSCH Analyzing & Testing*. Web.

94) S. Caminada, Introduction to P91/T91 Material, International Workshop on Fabrication and Processing of Grade 91 Material, 25 February 2011

95) "X-ray Powder Diffraction Beamline (XPD)." *BNL | National Synchrotron Light Source II (NSLS-II).*

96) De Graef, M., & McHenry, M. (2012). X-ray diffraction: Geometry. In *Structure of Materials: An Introduction to Crystallography, Diffraction and Symmetry* (pp.

259-290). Cambridge: Cambridge University Press.

97) "LOI Bragg." *Wikimedia Commons*. https://commons.wikimedia.org/w/index.php?curid=14524146

98) E. Stergar, M. Salston, K. Fields, Y. Wu, G.R. Odette, "On the High Temperature Creep Behavior of Nanostructured Ferritic Alloys", UC-Santa Barbara, Santa Barbara, USA, 2017

99) J. P. Biersack and L. Haggmark, Nucl. Instr. and Meth., vol. 174, 257, 1980) and the work by J. F. Ziegler on stopping theory (see "The Stopping and Range of Ions in Matter", *volumes 2 - 6*, Pergamon Press, 1977-1985

100) DIFFRAC.SUITE TOPAS - XRD Software, X-ray Diffraction." *Bruker.com*. N.p.,.

101) Standard Test Methods for Tension Testing of Metallic Materials. ASTM, West Conshohoken, PA., 2015, E8, pp.60–81.

102) D.J Sprouster, M. Elbakhshwan, L.E Ecker, Brookhaven National Laboratory, unpublished communication

103) Ishiwari, R. Shiomi-Tsuda, N. Sakamoto, N. 'Stopping Powers of Be, Al, Ti, V, Fe, Co, Ni, Cu, Zn, Mo, Rh, Ag, Sn, TA, Pt and Au for 6.5 MeV Protons' 1988 1988-Ishi2 Nucl. Inst. Methods, B31, 503 (1988)

104) W.C. Oliver and G.M. Pharr Measurement of hardness and elastic modulus by instrumented indentation: Advances in understanding and refinements to methodology. Journal of Materials Research. V. 19 (Issue 1) January 2004 01 March 2011

105) B. Eftink, E. Aydogan, D. Vega, et al. Unpublished research

106) "Metal Additive Manufacturing." Accelerated Certification of Additively Manufactured Metals (ACAMM). https://acamm.llnl.gov/ N.p., n.d. Web.